

**NUMERICAL METHODS FOR COMPUTING THE MODAL DECOMPOSITION
OF THE MAGNETIC POLARIZABILITY OF CONDUCTING OBJECTS**

A Dissertation
Presented to
The Academic Faculty

By

Jonathan E. Gabbay

In Partial Fulfillment
of the Requirements for the Degree
Doctor of Philosophy in
Electrical and Computer Engineering



School of Electrical and Computer Engineering
Georgia Institute of Technology
August 2019

Copyright © Jonathan E. Gabbay 2019

**NUMERICAL METHODS FOR COMPUTING THE MODAL DECOMPOSITION
OF THE MAGNETIC POLARIZABILITY OF CONDUCTING OBJECTS**

Approved by:

Waymond R. Scott, Jr, Advisor
School of Electrical and Computer
Engineering
Georgia Institute of Technology

Dr. Gregory Durgin
School of Electrical and Computer
Engineering
Georgia Institute of Technology

Dr. Andrew Peterson
School of Electrical and Computer
Engineering
Georgia Institute of Technology

Dr. Morris Cohen
School of Electrical and Computer
Engineering
Georgia Institute of Technology

Dr. Michael Lacey
School of Mathematics
Georgia Institute of Technology

Date Approved: May 1, 2019

And as imagination bodies forth
The forms of things unknown, the poet's pen
Turns them to shapes and gives to airy nothing
A local habitation and a name

-William Shakespeare

To my parents, Joan and David.

ACKNOWLEDGEMENTS

First and foremost, I would like to thank my advisor, Dr. Waymond R. Scott, Jr., for his support and guidance over the years, both professionally and personally. I have learned so much from him that it is truly hard to overstate the influence he has had on the person I have become. I am very grateful for this.

I would like to thank the members of my reading committee, Dr. Durgin and Dr. Peterson, who also served as members of my proposal committee, for their technical feedback and for helping to refine my thesis work. The classes they taught helped to develop my technical skills early in my graduate studies. Dr. Peterson, thanks again for meeting with me numerous times to advise me about various numerical methods. I would also like to thank Dr. Cohen and Dr. Lacey for serving on my committee.

I would like to thank my labmates in the Electromagnetics group, past and present: Sam Carey, Dylan Crocker, Ethan Hayes, Rohit Joshi, Andrew Kerr, Kyle Krueger, Mike McFadden, Mark Reed, James Sustman. Mike McFadden in particular taught me so much when I was starting out, and for that I am extremely grateful. Thanks to the staff members at Georgia Tech: Debbie, Janine and Daniela.

I would like to thank my family, and especially my parents, Joan and David, and my two sisters, Yael and Talia. You mean the world to me. Thanks for being there for me over the years. I would finally like to thank my girlfriend Michelle Plavnik and all of my dear friends. Thank you for supporting me over the years and encouraging me along the way. I am very fortunate.

TABLE OF CONTENTS

| | |
|--|-----------|
| Acknowledgments | v |
| List of Tables | x |
| List of Figures | xi |
| Summary | xv |
| Chapter 1: Introduction | 1 |
| 1.1 Fundamentals of Electromagnetic Induction Sensing | 2 |
| 1.2 The Magnetic Polarizability Tensor | 3 |
| 1.3 Pole-Expansion Form | 4 |
| 1.3.1 Simplifications for Targets with Symmetry | 6 |
| 1.3.2 Graphing the Magnetic Polarizability | 7 |
| 1.3.3 Scaling the Pole-Expansion Coefficients | 8 |
| 1.3.4 Inverting Pole-Expansion Coefficients from Experimental Data | 8 |
| 1.3.5 Numerically Computing Pole-Expansion Coefficients | 11 |
| 1.4 Outline | 11 |
| I Integral Methods | 13 |
| Chapter 2: Conducting Sheets and Shells | 14 |

| | | |
|---|--|-----------|
| 2.1 | Introduction | 14 |
| 2.2 | Electromagnetic Model | 15 |
| 2.3 | Numerical Strategy | 17 |
| 2.3.1 | Discretization and Choice of Basis Functions | 17 |
| 2.3.2 | Discrete Gradient Operator | 18 |
| 2.3.3 | Pole Expansion Derivation | 20 |
| 2.4 | Implementation Details | 22 |
| 2.5 | Computational and Experimental Results | 23 |
| 2.5.1 | Hollow Spherical Conductor | 23 |
| 2.5.2 | Cylindrical Tubing | 23 |
| 2.5.3 | Thin Conducting Disk | 25 |
| 2.5.4 | Shells of the Platonic Solids | 25 |
| 2.6 | Conclusion | 27 |
| Chapter 3: Conducting Solids | | 33 |
| 3.1 | Introduction | 33 |
| 3.2 | Electromagnetic Model | 34 |
| 3.3 | Numerical Strategy | 36 |
| 3.3.1 | Discretization and Choice of Basis Functions | 36 |
| 3.3.2 | Discrete Curl Matrix | 37 |
| 3.3.3 | Tree-Cotree Decomposition and Projection | 38 |
| 3.3.4 | Pole Expansion Derivation | 42 |
| 3.4 | Numerical Implementation | 44 |

| | | |
|--|---|-----------|
| 3.5 | Results | 44 |
| 3.5.1 | Spherical Conductor | 44 |
| 3.5.2 | Cubical Conductor | 48 |
| 3.5.3 | Regular Tetrahedron | 51 |
| 3.6 | Conclusion | 53 |
| Chapter 4: Bodies of Revolution | | 54 |
| 4.1 | Introduction | 54 |
| 4.2 | Numerical Strategy | 54 |
| 4.2.1 | Circuit Impedance Model | 54 |
| 4.2.2 | Generalized Eigenvalue Problem | 56 |
| 4.2.3 | Pole Expansion Derivation | 57 |
| 4.3 | Results | 58 |
| 4.3.1 | Spherical Conductor | 58 |
| 4.3.2 | Thick Wire Loops | 59 |
| 4.4 | Conclusion | 65 |
| II Differential Methods | | 66 |
| Chapter 5: Conducting Solids | | 67 |
| 5.1 | Introduction | 67 |
| 5.2 | The Finite Integration Technique | 67 |
| 5.3 | A Curl-Curl Equation | 70 |
| 5.4 | The Sparse Generalized Eigenvalue Problem | 72 |
| 5.4.1 | The Lanczos Algorithm | 73 |

| | | |
|---|---|------------|
| 5.4.2 | The FEAST Algorithm | 74 |
| 5.4.3 | The Jacobi-Davidson Iteration | 75 |
| 5.5 | Null Space Avoidance Techniques | 81 |
| 5.5.1 | Ritz Value Filtering | 81 |
| 5.5.2 | Tree-Cotree Filtering | 82 |
| 5.5.3 | Simplified Augmented System | 84 |
| 5.5.4 | Null-Space-Free Jacobi-Davidson | 85 |
| 5.6 | Pole Expansion Derivation | 89 |
| 5.7 | Numerical Implementation | 93 |
| 5.8 | Results | 94 |
| 5.8.1 | Spherical Conductor | 94 |
| 5.8.2 | Cubical Conductor | 97 |
| 5.9 | Conclusion | 100 |
| Chapter 6: Conclusions and Discussion | | 101 |
| Appendix A: Derivation of the Reciprocity Relation | | 105 |
| Appendix B: Pole Expansion of a Spherical Shell | | 107 |
| References | | 115 |

LIST OF TABLES

| | | |
|-----|--|----|
| 2.1 | Comparison between the thin-disk limit fitted using the finite element method (FEM)[5] and the surface integral method (SIM) © 2019 IEEE | 25 |
| 2.2 | Normalized magnetic polarizability expansion coefficients for the shells of the five Platonic solids and a hollow sphere | 26 |

LIST OF FIGURES

| | | |
|-----|---|----|
| 1.1 | Operating principle of an EMI sensor. By illuminating a conductor with a time-varying magnetic field, \vec{H}^{inc} , eddy currents, \vec{J} , are excited in the conducting media. According to Lenz's law, these eddy currents induce a scattered magnetic field, \vec{H}^{sca} , that opposes the magnetic excitation; the currents decay exponentially in time. | 2 |
| 1.2 | EMI response of a non-permeable copper sphere of radius 1 cm. In Fig. 1.2a, an Argand diagram of the zz -component of the magnetic polarizability tensor is plotted. In Fig. 1.2b, a characteristic stem plot of the pole-expansion coefficients is shown, where the stem positions are the relaxation frequencies, ζ_k , and the zz -components of the magnetic polarizability tensor are the amplitudes. | 7 |
| 1.3 | Cart-mounted wideband EMI sensor, that operates over a frequency range from 1 kHz to 90 kHz at 17 logarithmically-spaced frequencies. This sensor has one large transmit coil and four smaller receive coils. | 9 |
| 1.4 | Measurement system used in this thesis. The system measures the frequency-dependent MPT of a target by rotating it in a circular path that passes between two coaxial and parallel coils, a transmitter and a receiver, which lie above and below the circular path. | 10 |
| 2.1 | Loop basis function associated with the central node © 2019 IEEE | 18 |
| 2.2 | Convergence plot for the pole-expansion coefficients of a hollow spherical conductor. The relative error in the coefficients is plotted against the inverse of the average mesh edge dimension. © 2019 IEEE. | 28 |
| 2.3 | Stream function, ψ , for the single z -oriented eddy-current mode of a hollow spherical shell. The analytically-derived and numerically-computed stream functions are plotted against the polar angle, θ , measured from the z -axis. Because of the rotational symmetry, the stream function does not vary in the azimuthal direction, ϕ . Therefore, the eddy current, $\vec{J} = \hat{n} \times \nabla\psi$, must flow exclusively in the azimuthal direction. | 29 |

| | | |
|-----|--|----|
| 2.4 | Longitudinal and transverse pole-expansion coefficients for thin conducting tubes plotted as a function of their aspect ratio, h/d . The coefficients were normalized by scaling the tubing dimensions so that they were inscribed by the unit sphere. © 2019 IEEE. | 30 |
| 2.5 | Current flow patterns for the first three longitudinal and transverse eddy-current modes of a conducting tube. Only one side of the tube is shown with the currents on the other side of the tube completing the contours. Two orthogonal modes can represent the transverse modes, y-directed modes (shown) and the x-directed modes which are identical after a 90° rotation. © 2019 IEEE. | 31 |
| 2.6 | Contours of the stream function of the first modes of the hollow platonic solids and the only mode of the hollow sphere (with a non-zero dipole moment). Equal currents flow through each of the contours, and all currents flow in the same direction around the shell. | 32 |
| 3.1 | Example graph with $\mathcal{N} = 4$, $\mathcal{E} = 5$, $\mathcal{F} = 2$. All nodes are positively oriented by convention, and the reference node is n_4 . The orientation of each of the edges and faces is denoted by an arrowhead. For this graph, the node-edge incidence matrix, \mathbf{G} , and the edge-face incidence matrix, \mathbf{C} , are given. It can be trivially seen that $\mathbf{CG} = \mathbf{0}$ | 38 |
| 3.2 | One of many tree-cotree decompositions relative to the boundary of a simple graph. The boundary is the set of edges on the exterior. One of the many possible trees is shown in bold, while the cotree edges are grayed out. Note that the tree does not close a cycle with itself or with the boundary. | 39 |
| 3.3 | Normalized pole-expansion coefficients of a spherical conductor. Since a sphere is an isotropic target, its polarizability tensors are diagonal, with equal entries along the diagonal. | 45 |
| 3.4 | Cutout of the mesh of a sphere that was used to derive the pole-expansion coefficients and draw the mode graphs. This mesh has 45,319 tetrahedra, which corresponds to 42,543 cotree unknowns. | 45 |
| 3.5 | Slices of the first three modes of a spherical conductor, computed using a volume integral method. The quiver plots illustrate the direction of current flow in the x - y plane. The color plots graph the amplitude of the current density flowing through the y - z plane. | 46 |
| 3.6 | Normalized pole-expansion coefficients of a cubical conductor. Since a cube is an isotropic target, its polarizability tensors are diagonal, with all of its non-zero entries being equal. | 47 |

| | | |
|------|--|----|
| 3.7 | Cutout of the cubical mesh used to draw the mode graphs. This mesh has 49,728 tetrahedra, which corresponds to 46,259 cotree unknowns. | 48 |
| 3.8 | Slices of the first three modes of a cubical conductor, computed using a volume integral method. The quiver plots illustrate the direction of current flow in the x - y plane. The color plots graph the amplitude of the current density flowing through the y - z plane. | 49 |
| 3.9 | Normalized pole-expansion coefficients of a tetrahedral conductor. Since a tetrahedron is an isotropic target, its polarizability tensors are diagonal, with all of its non-zero entries being equal. | 50 |
| 3.10 | Cutouts of the tetrahedral mesh used to draw the mode graphs. This mesh has 47,001 tetrahedra, which corresponds to 29,796 cotree unknowns. | 51 |
| 3.11 | Slices of the first three modes of a conducting regular tetrahedron, computed using a volume integral method. The quiver plots illustrate the direction of current flow in the x - y plane. The color plots graph the amplitude of the current density flowing through the x - z and y - z planes. | 52 |
| 4.1 | Cutout of a torus discretized into rotationally-symmetric elements with triangular cross section. | 55 |
| 4.2 | Slices of the eddy-current modes in the y - z plane of a non-permeable conducting sphere. The cross section of the current-density flow is plotted, with blue and red marking currents that flow into the page and out of the page respectively. | 60 |
| 4.3 | Convergence plot for the pole-expansion coefficients of the MPT of a spherical conductor. The relative error in the pole-expansion coefficients is plotted against the mesh's average relative edge length. | 61 |
| 4.4 | Slices of the eddy-current modes of a thick wire loop with $a/b = 0.5$. The cross section of the current-density flow in the y - z plane is plotted, with blue and red marking currents that flow into the page and out of the page respectively. | 62 |
| 4.5 | Pole-expansion coefficients of a thick wire loop that are divided by their analytical values for a thin wire loop, and then graphed against their aspect ratio a/b . Experimental data validates the thin-wire approximation but also demonstrates the significance of higher-order modes. | 63 |

| | | |
|-----|---|----|
| 4.6 | Normalized pole-expansion coefficients of a thick wire loop are graphed against their aspect ratio a/b . The radii of the wire loops have been normalized to 1 so that the coefficients can be easily scaled. | 64 |
| 5.1 | Illustration of a Yee grid for the magneto-quasistatic grid equations | 68 |
| 5.2 | Alain Bossavit’s “Maxwell’s House”, which illustrates the relations between electromagnetic unknowns, scalar and vector potentials, and the constitutive relations. Left facade: Faraday complex. Right facade: Ampere complex. Front facade: Electric fields and charges. Back facade: Magnetic fields and impressed currents. Note the time derivatives that acts between front and back facades. | 68 |
| 5.3 | Illustration of a discretized highly-conductive sphere embedded in a low conductivity region. Only the primary cells in the conducting region are shown, illustrating FIT’s characteristic cubical grid. | 71 |
| 5.4 | Normalized pole-expansion coefficients of a spherical conductor. Since a sphere is an isotropic target, its polarizability tensors are diagonal, with equal entries along the diagonal. | 95 |
| 5.5 | Slices of the first five modes of a spherical conductor in the $y-z$ plane, with a dipole moment pointing in the \hat{z} -direction. A color plot of the amplitude of the current density is graphed with blue and red currents flowing in and out of the page respectively. | 96 |
| 5.6 | Normalized pole-expansion coefficients of a cubical conductor. Since a cube is an isotropic target, its polarizability tensors are diagonal, with equal entries along the diagonal. | 98 |
| 5.7 | Slices of the first five modes of a cubical conductor in the $y-z$ plane, with a dipole moment pointing in the \hat{z} -direction. A color plot of the amplitude of the current density is graphed with blue and red currents flowing in and out of the page respectively. | 99 |

SUMMARY

This thesis presents numerical methods for characterizing the wideband responses of conducting objects to excitation by electromagnetic induction (EMI) sensors. These sensors operate by exciting eddy currents in conducting media and detecting the scattered fields that the eddy currents induce. EMI sensors can be used to measure the magnetic polarizability tensor (MPT) of conducting targets, which encapsulates the entire scattering interaction between target and sensor.

Wideband characterization of the magnetic polarizability tensor can be achieved by expanding the frequency response in pole-expansion form. The pole-expansion coefficients may be used as a signature, which can be used for subsurface detection. These coefficients are valuable for target detection because they do not depend on the positioning of the target relative to the sensor or on the specific measurement frequencies and can be trivially scaled to represent larger families of targets.

Developing numerical methods for deriving the pole-expansion coefficients is important, because closed-form expressions for the coefficients are rarely available, and inversions of experimental data are often unreliable. Analytical expressions are only derivable for geometries such as a sphere or a thin wire loop, that exhibit high degrees of symmetry. Inversions of experimental data are often unreliable, because the inverse problem is ill-conditioned; even noiseless data cannot be inverted reliably because of the finite arithmetic precision.

In this work, both integral and differential methods are developed for modeling different types of targets, including rotationally-symmetric targets and thin sheets. The interaction between sensor and target is modeled as a linear system, which can then be set up as a generalized eigenvalue problem. The eigenvalues of the system correspond to the pole locations of the pole expansion. The remaining coefficients can be derived from the eigenvectors of the system, which correspond to the natural modes of the eddy-current problem.

CHAPTER 1

INTRODUCTION

Despite limited use in recent years, landmines remain a major cause of death and maiming in many countries across the world. According to the International Campaign to Ban Landmines, every day in 2016, an average of 23 people around the world lost their life or limb to a landmine or another explosive remnant of war [1]. Because of this large humanitarian cost, there has been a dedicated effort to detect and remove landmines in a safe and reliable manner.

Detecting landmines reliably is a difficult task. Landmines are generally concealed in unknown locations underground, which means that sensors must be able to detect them through layers of soil. The task is further complicated by abundant metallic clutter, such as ammunition shells, that are ubiquitously found in the surrounding scene. For this task, landmine detectors generally utilize a combination of electromagnetic induction (EMI) and ground-penetrating radar (GPR) sensors. These sensors are also used in a variety of other applications where it is important to be able to discriminate between targets and clutter. These applications include treasure hunting, archaeology, utility location, and geophysical prospecting.

These two types of sensors provide complementary information about buried targets. GPR sensors are capable of detecting both conducting and non-conducting targets but have limited ability to discriminate between target types, and more importantly, to discriminate between targets and clutter. EMI sensors, in contrast, cannot detect non-conducting targets directly but can gather additional information about conducting targets that can be used to infer their shape, size, spatial orientation, and material composition. The focus of this work is to characterize the wideband EMI responses of different types of conducting targets, including conducting sheets and shells and conducting bodies of revolution.

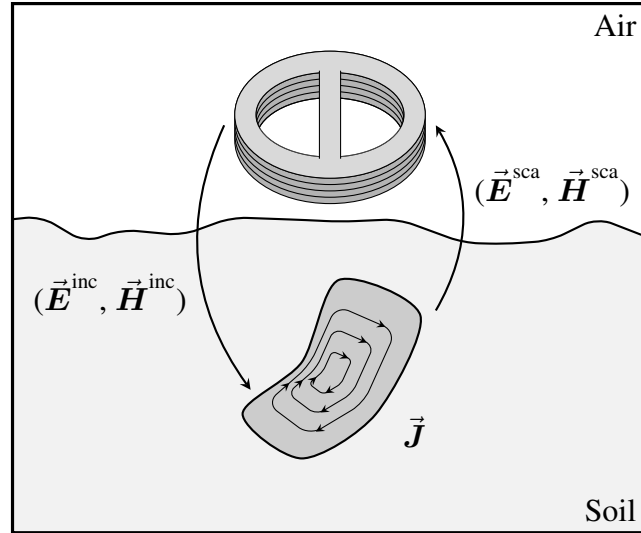


Figure 1.1: Operating principle of an EMI sensor. By illuminating a conductor with a time-varying magnetic field, \vec{H}^{inc} , eddy currents, \vec{J} , are excited in the conducting media. According to Lenz’s law, these eddy currents induce a scattered magnetic field, \vec{H}^{sca} , that opposes the magnetic excitation; the currents decay exponentially in time.

1.1 Fundamentals of Electromagnetic Induction Sensing

EMI sensors are commonly chosen for applications that require detecting electrically-conductive targets that are buried at shallow depths in non-conductive soil. Although EMI sensors cannot detect non-conducting targets, many targets of interest have significant metallic content, including landmines and unexploded ordnance (UXO). Detection using EMI sensors is based upon the physical phenomenon whereby an excitation in the form of a time-varying magnetic field causes eddy currents to flow in conducting media. These eddy currents, according to Lenz’s law [2], are known to induce a scattered magnetic field that opposes the magnetic excitation. EMI sensors transmit a magnetic field that penetrates the soil; by sensing the scattered fields, they are able to detect the presence of buried metal. The basic operating principle of an EMI sensor system is illustrated in Fig. 1.1.

At its most basic level, an EMI sensor system is comprised of two sets of coils, transmitting and receiving, which are not necessarily disjoint. The transmitting coils are driven by a time-varying current source such that they produce the desired magnetic excitation. The

receiving coils measure the scattered magnetic response. Isolation between the transmitting and receiving coils is often achieved either by time gating or by choosing coils with orthogonal fields (e.g. dipole coils for transmitting and quadrupole coils for receiving). Systems with multiple receiving coils are common, as they can gather additional information about the location and orientation of targets.

Frequent false alarms are a significant issue for narrowband EMI sensors, since the scattered responses due to metallic clutter cannot be distinguished reliably from the responses from targets of interest. Wideband sensors can provide an answer to this clutter problem by collecting additional frequency data, which captures within it information about the target's shape, size, conductivity, and permeability. EMI sensors can be designed to utilize very high bandwidths, such as the sensor in [3], which operates over the frequency range of 300 Hz to 90 kHz, a bandwidth of 300:1. When broadband data are measured at different positions relative to the target, the measured data can be checked against a dictionary so that only targets of specific types are flagged. The additional data can also be used to estimate the target's position and orientation underground.

Because of the promise of wideband EMI sensing, substantial attention has been given to deriving numerical models for the EMI scattering problem [4, 5, 6, 7, 8]. Eddy current problems, more generally, have been studied extensively in the past, using mostly variational methods [9, 10]. Later, symmetric boundary element methods emerged [11], based on the work of Hiptmair [12], that have since gained in popularity.

1.2 The Magnetic Polarizability Tensor

In EMI detection, it is common to approximate a target by a magnetic dipole, so that the EMI scattering mechanism can be represented by a magnetic polarizability tensor (MPT), M , which is a symmetric, positive-semidefinite, rank 2 tensor (dyadic), with 6 independent coefficients [13]. This approximation is valid whenever the target is electrically small relative to the wavelength of the sensor. When this dipole approximation is valid, the voltage

measured across the receiving coil, V_{ind} , can be approximated using reciprocity by

$$V_{\text{ind}} \approx j\omega\mu_0 \vec{\mathbf{H}}_{\text{RX}}(\vec{\mathbf{r}}) \cdot \left(\mathbf{M} \vec{\mathbf{H}}_{\text{TX}}(\vec{\mathbf{r}}) \right), \quad (1.1)$$

where ω is the angular frequency, $\vec{\mathbf{H}}_{\text{TX}}(\vec{\mathbf{r}})$ is the magnetic field due to the transmitting coil at the location of the target, and $\vec{\mathbf{H}}_{\text{RX}}(\vec{\mathbf{r}})$ is the field of the receiving coil at the target had it been driven by a unit-magnitude time-varying current. In other words, the reciprocity relation states that the EMI response depends *exclusively* upon the magnetic polarizability of the target and the magnetic fields supported by the transmitting and receiving coils at the location of the target. A derivation of this reciprocity relation is given in Appendix A.

Targets can be identified based on the frequency dependence of their tensor coefficients. This is because \mathbf{M} does not vary with a target's positioning or orientation relative to the sensor. Early work by Shubitidze *et al.* [14] computed the MPT of three-dimensional and rotationally-symmetric UXO using the method of auxiliary sources. More recently, Ledger [15] presented a method for computing the MPT of general targets, which include both permeable and non-permeable targets as well as targets with sharp edges.

1.3 Pole-Expansion Form

Still unresolved is the question of how to optimally discriminate between targets and clutter based upon their frequency-dependent MPT. An interesting approach to wideband EMI characterization was introduced by Baum [16], where he proposed applying the singularity expansion method in the EMI context. Under this framework, the frequency response of a target is viewed as a pole expansion with real-valued poles. Much of the early efforts at this characterization were concerned with computing the pole locations of different targets, which may be viewed as the reciprocal of the time constants of the exponential decay of the different natural modes excited in the target. This is because these time constants are independent of the positioning and orientation of the target relative to the sensor. The

pole-expansion coefficients were derived analytically for a thin wire loop and a conducting sphere [6]. Carin *et al.* [4] computed these time constants for rotationally-symmetric conductors, including permeable targets. This work, however, neglected the spatial dependence embedded in the magnetic polarizability tensor, which can be very valuable for target classification.

More recently, a modal approach was proposed by McFadden [17], for computing the pole-expansion coefficients of targets numerically. This methodology was used to compute wideband models for non-permeable, rotationally-symmetric targets. Under this viewpoint, Baum's frequency-dependent MPT is viewed through the lens of natural modes, each decaying exponentially in time at a corresponding real-valued relaxation frequency, the reciprocal of the time constant of its exponential decay. Under this framework, the frequency-dependent MPT, $\mathbf{M}(\omega)$, can be characterized by a discrete set of frequency-independent coefficients,

$$\mathbf{M}(\omega) = \mathbf{M}_0 - \sum_{k=1}^K \frac{j\omega/\zeta_k}{1 + j\omega/\zeta_k} \mathbf{M}_k, \quad (1.2)$$

where ζ_k are the relaxation frequencies, \mathbf{M}_k are frequency-independent MPTs, and \mathbf{M}_0 is the DC term. This approach separates the frequency behavior from a set of frequency-independent MPTs, that represent the scattering behavior of each of the natural modes.

This modal viewpoint of the EMI scattering problem has several notable advantages. It allows the frequency-dependent MPT to be represented by a small number of frequency-independent coefficients. This allows the frequency-dependent MPT to be easily computed for any frequencies of interest. The frequency-independent coefficients can be scaled to describe targets with the same shape but different characteristic dimension or electrical conductivity. In this way, a large family of targets can be described using a single set of parameters. The natural modes, which are computed as a byproduct of the modal approach, provide insight into the current flow patterns. This may often be beneficial but is especially helpful when attempting to design sensor components or shielding that does not interfere with the EMI sensor.

1.3.1 Simplifications for Targets with Symmetry

For any target, because \mathbf{M} is symmetric, it is also diagonalizable, meaning that there must be some orthogonal transformation for which the tensor is diagonal. The number of independent tensor coefficients after the transformation reduces to 3, with 3 degrees of freedom remaining to characterize the orthogonal transformation. All three tensor components must be non-negative because \mathbf{M} is positive semidefinite.

When a target is rotationally symmetric, two of the tensor coefficients along the diagonalized tensor must be identical, reducing the number of unique tensor coefficients to 2. The orthogonal transformation has only 2 degrees of freedom, because of the rotational invariance. If the z -axis is the axis of rotation, then $\mathbf{M}|_{zz}$ is independent, but $\mathbf{M}|_{xx} = \mathbf{M}|_{yy}$ and all the off-diagonal coefficients are zero.

For a small subset of conductor geometries that have high degrees of symmetry, including spheres and Platonic solids, the total number of degrees of freedom is reduced to 1. Their target responses are known to be isotropic, meaning that their MPT is a scalar multiple of the identity tensor, and the tensor is invariant with respect to orthogonal transformations. In these cases, the pole expansion can be simplified,

$$(\mathbf{M}(\omega)|_{zz})\mathbf{I}_3 = \sum_{k=1}^K \frac{j\omega/\zeta_k}{1 + j\omega/\zeta_k} (\mathbf{M}_k|_{zz})\mathbf{I}_3, \quad (1.3)$$

where $\mathbf{M}(\omega)|_{zz}$ is a scalar function of frequency representing the zz -component of $\mathbf{M}(\omega)$, \mathbf{I}_3 is the identity tensor of dimension 3, and $\mathbf{M}_k|_{zz}$ are scalar coefficients representing the zz -components of \mathbf{M}_k . In this expression the entire tensor was represented by its zz -component, however, this choice is arbitrary, since the tensor's diagonal terms are equal, $\mathbf{M}|_{xx} = \mathbf{M}|_{yy} = \mathbf{M}|_{zz}$. All off-diagonal tensor coefficients for an isotropic target must be identically zero. In other words, an isotropic target requires only two sets of scalar values to characterize its pole expansion, the set of relaxation frequencies, ζ_k , and a set of amplitudes, $\mathbf{M}_k|_{zz}$.

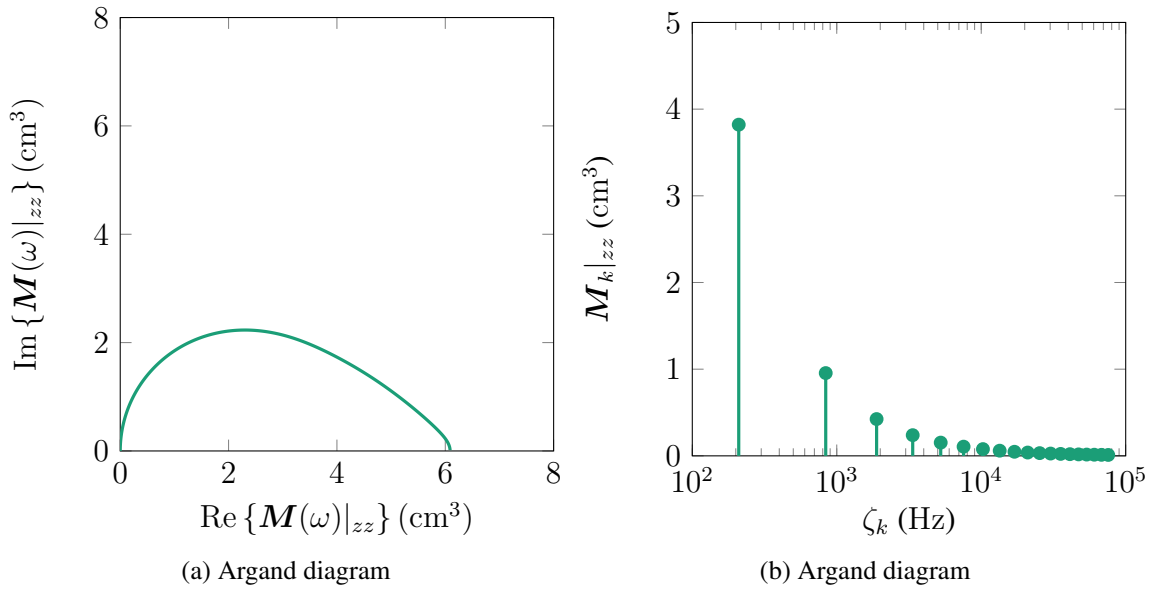


Figure 1.2: EMI response of a non-permeable copper sphere of radius 1 cm. In Fig. 1.2a, an Argand diagram of the zz -component of the magnetic polarizability tensor is plotted. In Fig. 1.2b, a characteristic stem plot of the pole-expansion coefficients is shown, where the stem positions are the relaxation frequencies, ζ_k , and the zz -components of the magnetic polarizability tensor are the amplitudes.

1.3.2 Graphing the Magnetic Polarizability

The MPT can be graphed either in the frequency domain or in the pole-expansion domain. In the frequency domain, the MPT is sometimes plotted on an Argand diagram, where one of the tensor coefficients of $\mathbf{M}(\omega)$ is plotted parametrically in frequency, with the real part on the x -axis and the imaginary part on the y -axis. An Argand diagram for the magnetic polarizability of a non-permeable copper sphere of radius 1 cm is plotted in Fig. 1.2a. General targets require six plots to characterize the MPT, but because the sphere has an isotropic response, a single plot can characterize the entire tensor. The MPT for the same sphere is graphed in the pole-expansion domain in Fig. 1.2b. In this plot, the height of the stems is determined by the amplitude, $M_k|_{zz}$, and the location is determined by the corresponding relaxation frequency, ζ_k . Although the pole-expansion terms associated with the higher relaxation frequencies appear inessential because of their small amplitude, they are significant when trying to reconstruct $\mathbf{M}(\omega)$ from the pole expansion.

1.3.3 Scaling the Pole-Expansion Coefficients

The pole-expansion coefficients can be scaled to describe targets with the same shape but different characteristic dimension or electrical conductivity. For this reason, it is beneficial to normalize the coefficients so that they can be reused. The pole expansion coefficients can be scaled from their normalized values using the relations [5]

$$\mathbf{M}_k = \widetilde{\mathbf{M}}_k R^3 \quad (1.4)$$

$$\zeta_k = \frac{\widetilde{\zeta}_k}{\sigma \mu_0 R^2}, \quad (1.5)$$

where $\widetilde{\mathbf{M}}_k$ and $\widetilde{\zeta}_k$ are normalized coefficients, σ is the electric conductivity of the scatterer, μ_0 is the permeability of free space, and R is the characteristic dimension of the scatterer. For thin scatterers, it is natural to normalize the relaxation frequencies using a sheet conductivity, $\sigma_s = \sigma t$, where t is the sheet thickness. If the sheet conductivity is to remain constant when the characteristic dimension is scaled, then the normalization becomes

$$\zeta_k = \frac{\widetilde{\zeta}_k^s}{\sigma_s \mu_0 R}, \quad (1.6)$$

where $\widetilde{\zeta}_k^s$ denotes a normalized coefficient that follows this shell scaling instead of Eq. (1.5). This parameter scaling derives directly from the electromagnetic equations and can be inferred from the derivation of the pole-expansion coefficients for the spherical shell (See Appendix B).

1.3.4 Inverting Pole-Expansion Coefficients from Experimental Data

The pole-expansion coefficients can be approximated from the measured spatial and frequency responses of a target. In this work, the process by which the coefficients are fitted from data will be referred to as inversion. In the field, measurements are inverted so that the fitted pole-expansion coefficients can be compared to a dictionary of targets of interest [18,



Figure 1.3: Cart-mounted wideband EMI sensor, that operates over a frequency range from 1 kHz to 90 kHz at 17 logarithmically-spaced frequencies. This sensor has one large transmit coil and four smaller receive coils.

19, 20, 21]. Field measurements are generally recorded in noisy environments and consist of relatively few looks at a target. An EMI system that was designed to collect field data is shown in Fig. 1.3.

In this work, the primary aim of fitting experimental data is to validate numerical results. As such, the experimental system used in this thesis was designed to minimize the effects of noise by taking long and controlled measurements. Generally, only a few of the fitted coefficients are accurate, because the inverse problem is highly ill-conditioned [22]. The accurate coefficients are those associated with the most dominant poles in the expansion. The inaccuracies cannot be attributed entirely to the noise, since even noiseless, synthetic data cannot be inverted perfectly, and poles with smaller relative tensor coefficients are often indiscernible [18]. Worse, these poles often combine to cause errors in the dominant terms of the expansion.

Laboratory Measurement System

The laboratory measurements recorded in this thesis were gathered using the experimental setup that was used in [5]. The system measures the frequency-dependent MPT, $M(\omega)$, of

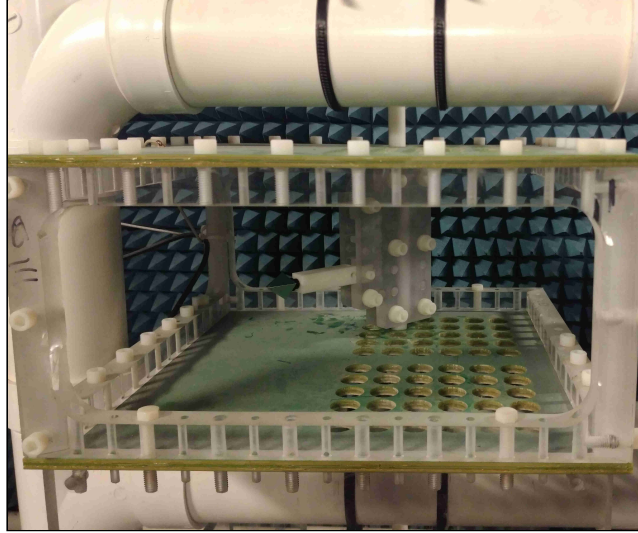


Figure 1.4: Measurement system used in this thesis. The system measures the frequency-dependent MPT of a target by rotating it in a circular path that passes between two coaxial and parallel coils, a transmitter and a receiver, which lie above and below the circular path.

a target by rotating it in a circular path that passes between two coaxial and parallel coils, a transmitter and a receiver, which lie above and below the circular path. The experimental setup is shown in Fig. 1.4. The transmitting coil is driven by a wideband multisine with 21 logarithmically-spaced tones, ranging between 330 Hz and 90.030 kHz. At each time step, the scattered response at the receive coil is recorded at each of the 21 frequencies.

Fitting the Pole-Expansion Coefficients

Using both the target's known position relative to the coils, and the voltages measured across the receive coil, a discrete number of poles and their corresponding positive-semidefinite frequency-independent MPTs can be inverted from the measured data by solving a convex optimization problem. Known target symmetries can be used to further constrain the optimization. For example, when inverting the MPT of a rotationally symmetric target, it is beneficial to assume that the tensor coefficients in each of the transverse directions are identical, to improve the fit. For an isotropic target like a sphere, making an isotropic assumption on the tensor coefficients improves the fit even further, because it drastically reduces the number of degrees of freedom.

1.3.5 Numerically Computing Pole-Expansion Coefficients

For the majority of targets, the pole-expansion coefficients must be computed numerically. Numerical approaches for computing the coefficients are important, because inversions of experimental data are often unreliable. Although it is straightforward to solve a quasi-magnetostatic problem and compute $M(\omega)$ for any given frequency, inverting this tensor does not produce accurate coefficients. Directly solving for the pole-expansion coefficients is much more accurate but also a far more complex task.

For a small subset of conductor shapes, the pole-expansion coefficients can be derived analytically. This subset is comprised of conductor geometries that are characterized by high degrees of symmetry and includes shapes such as spheres, prolate and oblate spheroids, and filament rings. In this work, these canonical targets will often be used for validation.

Numerical computation of coefficients has been performed in the past for targets with rotational symmetry [4, 17], but this analysis has not been extended to general target geometries. The objective of this work is to develop techniques for numerically computing the pole-expansion coefficients of the frequency-dependent magnetic polarizability of conducting targets with more general target geometries.

1.4 Outline

The methods described in this thesis can be used to derive the pole-expansion coefficients of the magnetic polarizability of families of targets, with dedicated methods for targets that are rotationally symmetric or targets that are thin in one dimension. In each of the methods, Maxwell's equations are first represented using a numerical method, either integral or differential, which is then set up as a generalized eigenvalue problem. The eigenvalues of the system correspond to the pole locations of the pole expansion. Because the eigenvectors of the system are the associated mode patterns, deriving the remaining coefficients in the pole

expansion involves very straightforward post-processing.

This document is organized in two parts, the first discussing integral methods and the second discussing differential methods. Part one contains three chapters: a method for modeling conducting sheets and shells, a method for modeling conducting solids, and a very simple method for conducting bodies of revolution. The second part discusses a differential method for modeling conducting solid targets. The document ends with a short conclusion and suggestions for future research.

Part I

Integral Methods

CHAPTER 2

CONDUCTING SHEETS AND SHELLS

2.1 Introduction

In this chapter, a method will be presented for computing the pole-expansion coefficients of the magnetic polarizability of thin conducting sheets and shells¹. In the past, pole-expansion coefficients have generally not been derived for these types of targets, aside from the coefficients for the thin circular disk in [5]. That particular volume approach, however, can only model rationally-symmetric targets and is computationally expensive for thin targets. A generalized approach for modeling surfaces and shells is valuable because many targets of interest can be assumed to be infinitesimally thin, which greatly reduces the complexity of the numerical model. Many obvious targets can be modeled in this way, such as metal containers, ammunition casings, and scrap metal, but also metal that might be deployed along with the EMI sensor, such as ground-penetrating radar antennas [24].

In this chapter, a method will be presented for computing the pole-expansion coefficients of the MPT of thin conducting targets. The method utilizes a stream function to enforce both a quasi-magnetostatic assumption and the appropriate boundary conditions on the eddy currents. The method is verified by comparing the numerically-derived pole-expansion coefficients for a spherical shell to a derived analytical solution (Appendix B). Numerically-computed coefficients are also compared to measured data. This includes the pole-expansion coefficients for cylindrical tubes, of various aspect ratios, which are compared to experimental results, showing good agreement. Pole-expansion coefficients are given for a disk and are compared to the results in [5]. Finally, pole-expansion coefficients and mode graphs are given for the shells of the Platonic solids, which are isotropic targets.

¹The work in this chapter has been published in [23].

Because of their high degrees of symmetry this class of targets only has one dominant pole in their respective pole expansions.

2.2 Electromagnetic Model

The primary aim of deriving a numerical model is to characterize the scattered magnetic field that is induced by the eddy currents that are excited by the EMI sensor in a thin conducting region, Ω_c . Maxwell's equations in their time-harmonic form, and under the eddy-current approximation, which allows displacement currents to be neglected, state that

$$\nabla \times \vec{H}(\vec{r}) = \vec{J}(\vec{r}) \quad (2.1a)$$

$$\nabla \times \vec{E}(\vec{r}) = -j\omega\vec{B}(\vec{r}) \quad (2.1b)$$

$$\nabla \cdot \vec{B}(\vec{r}) = 0 \quad (2.1c)$$

$$\nabla \cdot \vec{J}(\vec{r}) = 0. \quad (2.1d)$$

In addition, the constitutional relationships state that

$$\vec{B}(\vec{r}) = \mu\vec{H}(\vec{r}) \quad (2.2a)$$

$$\vec{J}(\vec{r}) = \sigma\vec{E}(\vec{r}), \quad (2.2b)$$

where μ is the permeability, and the electrical conductivity, σ , satisfies

$$\sigma = \begin{cases} \sigma_c & \text{in } \Omega_c \\ 0 & \text{in } \Omega \setminus \Omega_c. \end{cases} \quad (2.3)$$

If a vector potential, $\vec{B}(\vec{r}) = \nabla \times \vec{A}(\vec{r})$, is introduced, then Ampere's law (2.1a) can be satisfied by

$$\nabla^2 \left(\vec{A}(\vec{r}) - \vec{A}^{\text{inc}}(\vec{r}) \right) = -\mu_0 \vec{J}(\vec{r}), \quad (2.4)$$

provided that the conducting and background media are assumed to be non-permeable. The incident magnetic vector potential, \vec{A}^{inc} , represents the magnetic excitation in the absence of the conductor. Implicit in this separation is the assumption that the excitation is not significantly altered by the addition of the conductor.

The well-known fundamental solution to the three-dimensional Laplacian is

$$\nabla^2 G(\vec{r}) = -\delta(\vec{r}), \quad (2.5)$$

where $G(\vec{r})$ is the free-space Green's function, $G(\vec{r}) = \frac{1}{4\pi r}$. Utilizing the Green's function, the magnetic vector potential due to the eddy currents flowing over a surface, S , can be written as

$$\vec{A}(\vec{r}) - \vec{A}^{\text{inc}}(\vec{r}) = \frac{\mu_0}{4\pi} \int_S \frac{\vec{J}(\vec{r}')}{\|\vec{r} - \vec{r}'\|} dS'. \quad (2.6)$$

When it is assumed that there is no charge built up in the computational domain, the electric field can be directly related to the magnetic vector potential, while also satisfying Faraday's law (2.1b), $\vec{E}(\vec{r}) = -j\omega \vec{A}(\vec{r})$. Substituting for the electric field and then subsequently substituting Ohm's law, $\vec{E}(\vec{r}) = \sigma_s^{-1} \vec{J}(\vec{r})$, into Eq. (2.6), we have

$$\sigma_s^{-1} \vec{J}_s(\vec{r}) + j\omega \frac{\mu_0}{4\pi} \int_S \frac{\vec{J}_s(\vec{r}')}{\|\vec{r} - \vec{r}'\|} dS' = -j\omega \vec{A}^{\text{inc}}(\vec{r}). \quad (2.7)$$

Eq. (2.7) relates the surface eddy currents, $\vec{J}_s(\vec{r})$, that flow in the conductor due to the magnetic excitation, $\vec{A}^{\text{inc}}(\vec{r})$.

2.3 Numerical Strategy

2.3.1 Discretization and Choice of Basis Functions

Following the approach in [17], we aim to utilize an eigenvalue solver to decompose Eq. (2.7) into its natural modes. Consequently, Eq. (2.7) is discretized using a finite-element basis. The conducting region is approximated by a polyhedral surface, comprised of triangular cells, which must be sufficiently small so as to properly represent the current density. Divergence-conforming constant normal/linear tangential (CN/LT) Nedelec basis functions [25, 26] were chosen to represent the divergence-free surface current density,

$$\vec{\mathbf{J}}_s(\vec{\mathbf{r}}) \approx \sum_{i=1}^{\mathcal{N}(\mathcal{E})} \mathbf{j}_i \vec{\mathbf{f}}_i(\vec{\mathbf{r}}), \quad (2.8)$$

where \mathbf{j}_i are the basis function coefficients, $\mathcal{N}(\mathcal{E})$ is the number of edges in the mesh, and

$$\vec{\mathbf{f}}_i(\lambda_j, \lambda_k) = \hat{\mathbf{n}} \times (\lambda_j \nabla \lambda_k - \lambda_k \nabla \lambda_j), \quad (2.9)$$

where $\vec{\mathbf{f}}_i$ is the basis function associated with the i th edge, that is oriented from node j to node k , and λ_j, λ_k are barycentric coordinates (in the triangles adjacent to the edge) for the two nodes that are common to the edge.

The choice of basis function is natural because the surface current density is solenoidal, Eq. (2.1d). While divergence-conforming (CN/LT) basis functions have finite divergence over their domain, the divergence of the constructed surface current density can be constrained to zero using a simple topological matrix. These divergence-conforming elements maintain the normal continuity of the surface current density across the boundary of cells. This prevents the accumulation of electric charge on the cell boundaries. Furthermore, using the same topological matrix, it is simple to satisfy the boundary conditions on the surface current density.

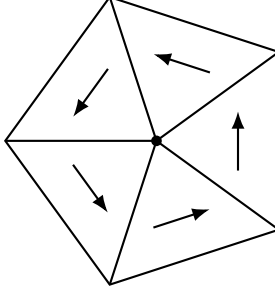


Figure 2.1: Loop basis function associated with the central node © 2019 IEEE

The discrete version of Eq. (2.7) can be written as

$$\mathbf{R}\mathbf{j} + j\omega\mathbf{L}\mathbf{j} = -j\omega\mathbf{a}^{\text{inc}}, \quad (2.10)$$

where the following matrices must be computed for each basis function pair:

$$\mathbf{L}_{ij} = \frac{\mu_0}{4\pi} \iint \frac{\vec{\mathbf{f}}_i(\vec{\mathbf{r}}) \cdot \vec{\mathbf{f}}_j(\vec{\mathbf{r}}')}{\|\vec{\mathbf{r}} - \vec{\mathbf{r}}'\|} dS' dS \quad (2.11)$$

$$\mathbf{R}_{ij} = \int \sigma_s^{-1} \vec{\mathbf{f}}_i(\vec{\mathbf{r}}) \cdot \vec{\mathbf{f}}_j(\vec{\mathbf{r}}) dS \quad (2.12)$$

$$\mathbf{a}_i^{\text{inc}} = \int \vec{\mathbf{f}}_i(\vec{\mathbf{r}}) \cdot \vec{\mathbf{A}}^{\text{inc}} dS. \quad (2.13)$$

Since the (CN/LT) basis functions are divergence conforming, Eq. (2.7) does not, on its own, constrain the solenoidality of the surface current density. The divergence of the surface current density will be constrained to zero by using a stream function to expand the basis-function coefficients.

2.3.2 Discrete Gradient Operator

The approach taken in this chapter is to represent the solenoidal surface current density using a scalar stream function (or equivalently, using loop basis functions [27]). Adopting either viewpoint, the basis-function coefficients are determined by scalar coefficients, interpolated over the nodes of the discrete mesh. A loop basis function is illustrated in Fig. 2.1.

A topological node-edges incidence matrix is used to algebraically constrain the basis-function coefficients to ensure the solenoidality of the surface current density in the conducting region. This can be achieved by using a node-edge incidence matrix, \mathbf{G} , with entries

$$\mathbf{G}_{ij} = \begin{cases} -1, & \text{if the } i\text{th edge is oriented negatively with} \\ & \text{respect to the } j\text{th node,} \\ +1, & \text{if the } i\text{th edge is oriented positively with} \\ & \text{respect to the } j\text{th node} \\ 0, & \text{otherwise.} \end{cases} \quad (2.14)$$

If the coefficients of the surface current density are constrained such that

$$\mathbf{j} = \mathbf{G}\psi, \quad (2.15)$$

where ψ is a scalar potential, then by substituting the potential into Eq. (2.10) and multiplying the equation by \mathbf{G}^T , it becomes

$$\mathbf{G}^T \mathbf{R} \mathbf{G} \psi + j\omega \mathbf{G}^T \mathbf{L} \mathbf{G} \psi = -j\omega \mathbf{G}^T \mathbf{a}_i^{\text{inc}}, \quad (2.16)$$

which is a symmetric matrix equation, with a number of unknowns equal to the number of nodes in the mesh. Finally, a generalized eigenvalue problem can be set up so as to diagonalize both system matrices,

$$\mathbf{G}^T \mathbf{L} \mathbf{G} \mathbf{v} = \lambda \mathbf{G}^T \mathbf{R} \mathbf{G} \mathbf{v}, \quad (2.17)$$

or

$$\mathbf{L}_G \mathbf{V} = \mathbf{R}_G \mathbf{V} \Lambda, \quad (2.18)$$

where each \mathbf{v} is an eigenvector, λ is the corresponding eigenvalue, $\mathbf{V} = [\mathbf{v}_1, \mathbf{v}_2, \dots, \mathbf{v}_K]$ is

the matrix of eigenvectors, $\Lambda = \text{diag}[\lambda_1, \lambda_2, \dots, \lambda_K]$ is the diagonal matrix of eigenvalues, $\mathbf{R}_G = \mathbf{G}^T \mathbf{R} \mathbf{G}$, and $\mathbf{L}_G = \mathbf{G}^T \mathbf{L} \mathbf{G}$. Both \mathbf{R}_G and \mathbf{L}_G are dense, symmetric, and positive definite, and their generalized eigenvalues and eigenvectors can be found trivially.

2.3.3 Pole Expansion Derivation

The generalized eigenvalues and eigenvectors of Eq. (2.17) can be used to expand Eq. (2.16) into pole-expansion form by first recognizing that

$$\mathbf{R}_G = \mathbf{R}_G \mathbf{V} \mathbf{V}^T \mathbf{R}_G \quad (2.19)$$

$$\mathbf{L}_G = \mathbf{R}_G \mathbf{V} \Lambda \mathbf{V}^T \mathbf{R}_G, \quad (2.20)$$

which derives from the \mathbf{R}_G -orthogonality of the eigenvectors, $\mathbf{V}^T \mathbf{R}_G \mathbf{V} = \mathbf{I}$. The pencil can then be written as

$$\mathbf{R}_G + j\omega \mathbf{L}_G = \mathbf{R}_G \mathbf{V} (\mathbf{I} + j\omega \Lambda) \mathbf{V}^T \mathbf{R}_G. \quad (2.21)$$

If Eq. (2.21) is multiplied on the left by \mathbf{V}^T and on the right by \mathbf{V} , then

$$\mathbf{V}^T (\mathbf{R}_G + j\omega \mathbf{L}_G) \mathbf{V} = (\mathbf{I} + j\omega \Lambda). \quad (2.22)$$

Taking the inverse of the pencil, provided that ω does not coincide with a pole, results in

$$\begin{aligned} (\mathbf{V}^T (\mathbf{R}_G + j\omega \mathbf{L}_G) \mathbf{V})^{-1} &= (\mathbf{I} + j\omega \Lambda)^{-1} \\ \mathbf{V}^{-1} (\mathbf{R}_G + j\omega \mathbf{L}_G)^{-1} (\mathbf{V}^T)^{-1} &= (\mathbf{I} + j\omega \Lambda)^{-1} \\ (\mathbf{R}_G + j\omega \mathbf{L}_G)^{-1} &= \mathbf{V} (\mathbf{I} + j\omega \Lambda)^{-1} \mathbf{V}^T, \end{aligned} \quad (2.23)$$

which can be written in summation form as

$$(\mathbf{R}_G + j\omega\mathbf{L}_G)^{-1} = \sum_{k=1}^K (1 + j\omega\lambda_k)^{-1} \mathbf{v}_k \mathbf{v}_k^T. \quad (2.24)$$

Using Eq. (2.24), it is possible to solve for the stream function unknowns in Eq. (2.16),

$$\boldsymbol{\psi} = - \sum_{k=1}^K \frac{j\omega}{1 + j\omega\lambda_k} \mathbf{v}_k \mathbf{v}_k^T \mathbf{G}^T \mathbf{a}_i^{\text{inc}}. \quad (2.25)$$

Multiplying Eq. (2.25) on the left by \mathbf{G} gives

$$\mathbf{j} = \mathbf{G}\boldsymbol{\psi} = - \sum_{k=1}^K \frac{j\omega\lambda_k}{1 + j\omega\lambda_k} \lambda_k^{-1} \mathbf{G}\mathbf{v}_k \mathbf{v}_k^T \mathbf{G}^T \mathbf{a}_i^{\text{inc}}, \quad (2.26)$$

where the eigenvalues can be identified as the reciprocal of the relaxation frequencies associated with the eddy-current modes. The magnetic polarizability of each of the current density modes can be computed from their magnetic dipole moments,

$$\vec{\mathbf{m}} = \frac{1}{2} \int_S \vec{\mathbf{r}} \times \vec{\mathbf{J}}_s(\vec{\mathbf{r}}) dS, \quad (2.27)$$

which can be evaluated using quadrature. The magnetic dipole moments are computed for eddy currents supported by excitations, $\vec{\mathbf{A}}^{\text{inc}}$, that correspond to \hat{x} -, \hat{y} -, and \hat{z} -directed uniform magnetic fields². Then, the components of the magnetic polarizabilities can be inverted from the magnetic moments using the relation

$$\vec{\mathbf{m}} = \mathbf{M} \cdot \vec{\mathbf{H}}^{\text{inc}}. \quad (2.28)$$

The three magnetic excitations provide a full-rank basis, which is sufficient to invert the tensor components.

²These $\vec{\mathbf{A}}^{\text{inc}}$ are not unique, and many compatible fields could have been chosen. In this work, for example, $\vec{\mathbf{A}}^{\text{inc}} = -\frac{1}{2}\mu_0(y\hat{x} - x\hat{y})$ was chosen for the \hat{z} -directed excitation.

2.4 Implementation Details

Triangular meshes for the conducting surfaces were generated with the MATLAB package `DistMesh` [28], when the conductor shapes were simple, and `gmsh` [29], when the conductor shapes were more complex. `DistMesh` produces better quality meshes, however, is restricted to a small set of geometries.

The basis-function interactions required to fill the \mathbf{R} and \mathbf{L} matrices were computed using a quadrature rule for triangles [30]. This rule has barycentric nodes at $(\frac{1}{6}, \frac{1}{6})$, $(\frac{2}{3}, \frac{1}{6})$, $(\frac{1}{6}, \frac{2}{3})$ and weights of $\frac{1}{3}$ for each. The singular kernel in Eq. (2.11) poses a challenge when computing the integrals for basis functions that have overlapping domains. These include the obvious self terms but also basis functions on neighboring triangles that share a vertex or edge with the source triangles. As in [31], the singularity was canceled using the approach outlined in [32]. After the inner integral has been simplified, the outer integral can be evaluated using the same quadrature rule for triangles.

The topological matrix, \mathbf{G} , is used to enforce boundary conditions. For closed surfaces with no boundary, such as a hollow sphere, it is sufficient to eliminate a single degree of freedom from \mathbf{G} to gauge the scalar potential. For a disk, a surface with a single boundary, all the degrees of freedom that correspond to boundary nodes can simply be eliminated from \mathbf{G} to enforce the boundary condition on the current. For a tube, a simple surface with two boundaries, one of the boundaries can be eliminated and the degrees of freedom from the remaining boundary may be combined into a single unknown. Enforcing boundary conditions for target geometries that are more complex requires special care and is beyond the scope of this thesis [31].

The generalized eigenvalues and eigenvectors of the linear system were computed using MATLAB's `eig` routine. The computations were run on a hex-core, 3.4 GHz Intel i7 processor, with 64 GB of memory. On this computer, `eig` will find all of the generalized eigenvalues and eigenvectors for a pair of $7,445 \times 7,445$ matrices in less than 10 min.

This corresponds to the mesh having 22,332 edges, which is equal to the number of basis functions used to expand the current density.

2.5 Computational and Experimental Results

2.5.1 Hollow Spherical Conductor

This target provides a useful benchmark for the numerical method because it is possible to derive an analytical expression for the pole-expansion coefficients (See Appendix B). The hollow sphere is also noteworthy because its high degree of symmetry causes it to have only a single eddy-current mode that has a non-zero dipole moment. This means that three of the generalized eigenvectors of the linear system have a non-zero moment, but they all share the same eigenvalue.

In Fig. 2.2, the relative error in pole-expansion coefficients is plotted versus the inverse of the average mesh edge length. This plot was generated by deriving the coefficients for meshes of varying coarseness and comparing them to their analytical values. The coefficients converge quadratically, with the frequency-dependent MPTs, M_k , achieving higher accuracy relative to the relaxation frequencies, ζ_k^s . It is possible that this occurs because of the additional integration that is performed when deriving those coefficients. In Fig. 2.3, the numerically-computed stream function for the spherical shell is compared to its analytical expression.

2.5.2 Cylindrical Tubing

Thin brass cylindrical tubes were chosen to provide a comparison between experimental and computational results. Brass tubing, which is commercially available in a wide variety of diameters, can be easily cut to specific lengths. Furthermore, the tubes physically resemble ammunition casings that often act as clutter in EMI detection. The aspect ratio of the cut tubing can be represented by the ratio of the height of the cylinder, h , to its diameter, d . The pole-expansion coefficients can then be plotted as a function of aspect ratio.

In Fig. 2.4, normalized pole-expansion coefficients, experimental and simulated, are plotted as a function of the tubing aspect ratio, h/d . The coefficients were first normalized by scaling the tubing dimensions so that they were inscribed by the unit sphere. This allows the coefficients to be easily scaled to any characteristic dimension. Numerical results are represented by the solid graph lines, that were generated by sweeping the cylinder aspect ratios over a large number of simulations. The scattered data points correspond to the inverted coefficients from the experimental measurements. The modes are ordered such that the first mode is the lowest in frequency and are the highest in tensor coefficient amplitude.

From examination of the plots, it is apparent that there is excellent agreement between the pole-expansion coefficients for the first-order modes in both longitudinal and transverse directions. The measured coefficients for the second-order modes are only moderately accurate. This is a consequence of the relative weakness of the second-order modes when compared to the first-order modes. In Fig. 2.5, the current patterns of the first three modes in both longitudinal and transverse directions are plotted.

The graphs in Fig. 2.4 can also be used to compute the pole-expansion coefficients for families of similar targets by using Eq. (1.4) and Eq. (1.6) to scale the normalized coefficients. In the experiment, the tube with $h/d = 3$, for example, was a non-permeable brass tube with a height of 1.5", a diameter of 0.5", a thickness of 0.014", and a conductivity of 1.602×10^7 S/m. Its first longitudinal mode was measured at a frequency of 8.451 kHz with an amplitude of 4.886 cm^3 . This corresponds to a measured normalized frequency of 7.632 and a normalized amplitude of 0.603. The numerical model, in comparison, computed a normalized frequency of 7.049 and a normalized amplitude of 0.618.

The inversion algorithm is inaccurate when inverting relaxations that are more than an order of magnitude weaker than the principle relaxation. In relative terms, the transverse coefficients are expected to be more accurate than the longitudinal coefficients, because the inversion exploits the axial symmetry of the tubing. The accuracy of the second-order modes is degraded, however, by inaccuracy in the third-order modes, which are extremely

Table 2.1: Comparison between the thin-disk limit fitted using the finite element method (FEM)[5] and the surface integral method (SIM) © 2019 IEEE

| n | $\tilde{\zeta}_n^s$ (SIM) | $\tilde{\zeta}_n^s$ (FEM) | $(\tilde{M}_{zz})_n$ SIM | $(\tilde{M}_{zz})_n$ FEM |
|-----|---------------------------|---------------------------|--------------------------|--------------------------|
| 1 | 0.439 | 0.44 | 1.933 | 1.93 |
| 2 | 0.939 | 0.94 | 0.333 | 0.33 |
| 3 | 1.442 | 1.43 | 0.129 | 0.13 |
| 4 | 1.948 | 1.92 | 0.067 | 0.07 |
| 5 | 2.459 | 2.41 | 0.041 | 0.04 |

difficult to invert due to their small amplitude. This inaccuracy in the higher-order modes highlights the importance of computational modeling, since inverted coefficients may have significant errors.

2.5.3 Thin Conducting Disk


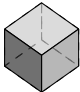




An interesting target for comparison is a thin conducting disk, since pole-expansion coefficients of cylindrical targets of varying aspect ratios have been modeled in [5]. In Table 2.1, the fitted thin-disk limit coefficients are compared to idealized numerical results that were computed with the surface integral method. The table shows excellent agreement between the two methods. To the extent that the coefficients differ, it is unclear which is more accurate.

2.5.4 Shells of the Platonic Solids

Eddy-current modes in the shells of the Platonic solids behave much like currents in a hollow sphere, in particular, all these targets have a MPT that is isotropic [6]. In Table 2.2, the coefficients corresponding to the first-order mode were normalized, so that each of the shells encompassed a volume of $4\pi/3$. Their normalized coefficients were compared to the coefficients of a unit-radius hollow sphere.

Of note, is the similarity in coefficients between the shells of the Platonic solids and the hollow spherical shell. While all the Platonic solid shells have additional poles with small

Table 2.2: Normalized magnetic polarizability expansion coefficients for the shells of the five Platonic solids and a hollow sphere

| | Shape | $\tilde{\zeta}_1^s$ | \tilde{M}_1 |
|---|--------------|---------------------|---------------|
|  | Tetrahedron | 3.0035 | 6.7515 |
|  | Cube | 3.0492 | 6.6502 |
|  | Octahedron | 3.0762 | 6.4630 |
|  | Dodecahedron | 3.0287 | 6.3934 |
|  | Icosahedron | 3.0262 | 6.3287 |
|  | Sphere | 3.0000 | 6.2832 |

non-zero dipole moments, the amplitude of the secondary poles, decreases with increasing solid order (the tetrahedron has the largest secondary poles, and the icosahedron has the smallest). The second mode of the tetrahedron has an amplitude that is 3% of the amplitude of the first mode, while the second mode of the icosahedron has a vanishingly-small amplitude. In Fig. 2.6, the first mode of each of the hollow platonic solids is plotted with a comparison to the single mode of the hollow sphere.

2.6 Conclusion

A surface integral method was presented for numerically deriving the pole-expansion coefficients of the magnetic polarizability of thin conducting shells. The method utilizes a stream function to enforce both a quasi-magnetostatic assumption and the appropriate boundary conditions on the currents. The coefficients are derived from the linear system matrices by performing a simple generalized eigendecomposition.

To demonstrate the validity of the method, a hollow spherical conductor was modeled, and the derived coefficients were compared to their analytical values. For additional verification, the pole-expansion coefficients of a thin conducting disk were compared to the limit computed by a finite element code. The pole-expansion coefficients were computed for the shells of the Platonic solids, which are isotropic. These shells only have one dominant pole because of their high degrees of symmetry.

Experimental verification was achieved by measuring the pole-expansion coefficients of a number of thin brass tubes and comparing them to the numerical predictions. The simulated coefficients corresponding to the first-order longitudinal and transverse modes showed excellent agreement with the experiment. The agreement with the second-order modes was only moderately good, however, these modes are weaker than the measurement system can invert accurately. This demonstrates the value of a numerical approach, because even with a controlled measurement system, the expansion coefficients cannot be inverted with precision.

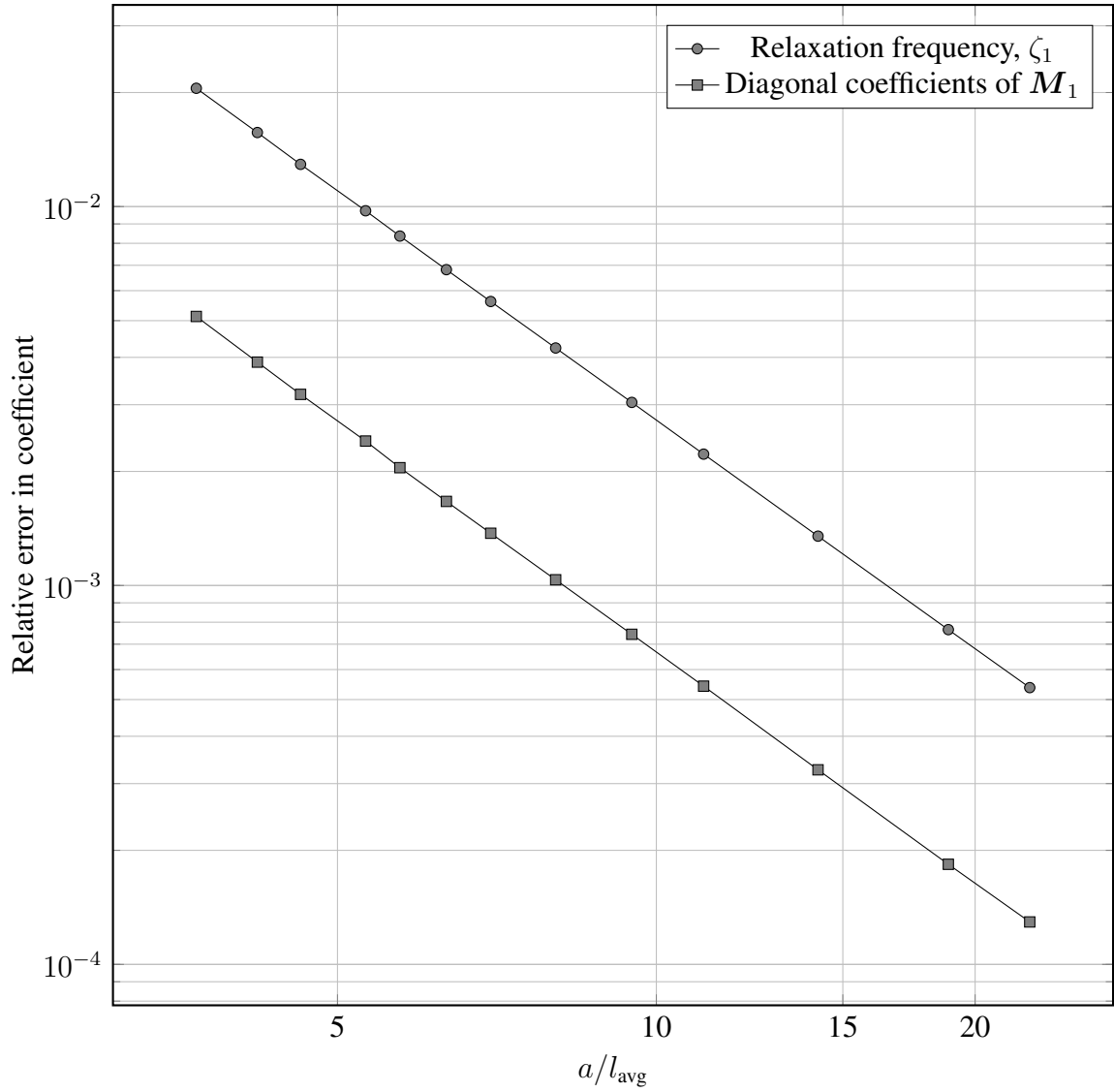


Figure 2.2: Convergence plot for the pole-expansion coefficients of a hollow spherical conductor. The relative error in the coefficients is plotted against the inverse of the average mesh edge dimension. © 2019 IEEE.

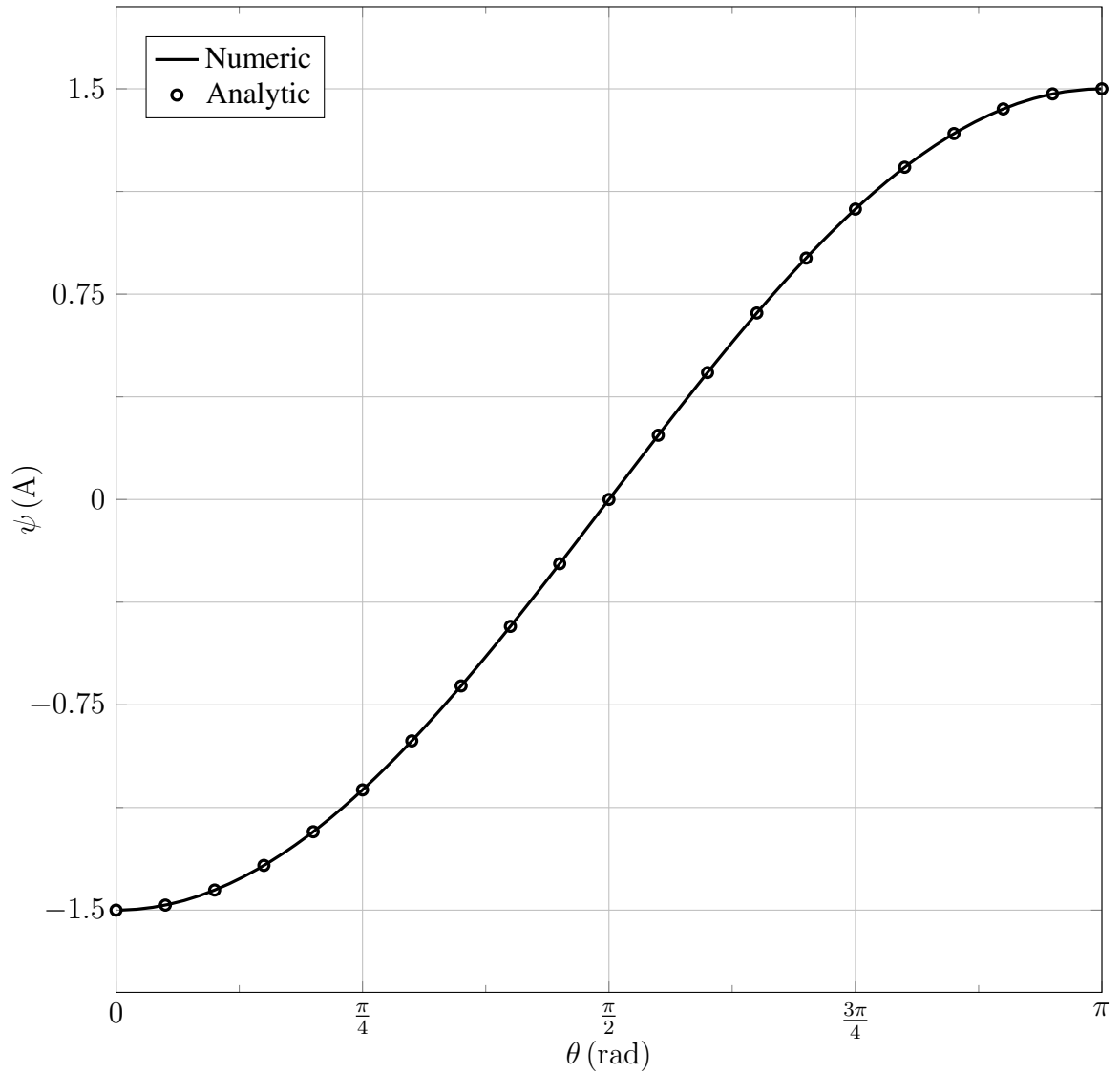
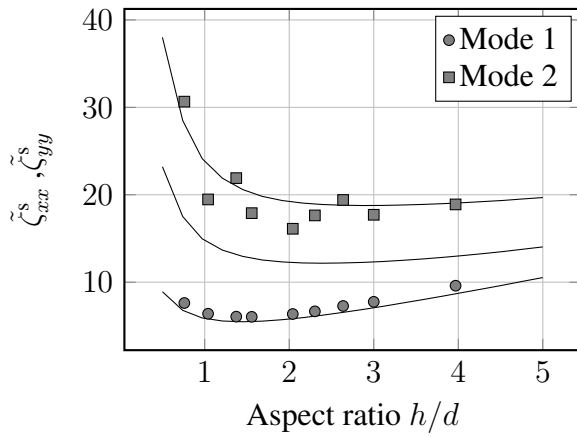
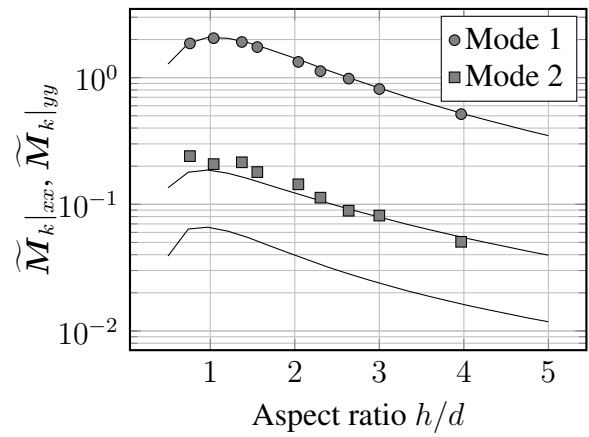


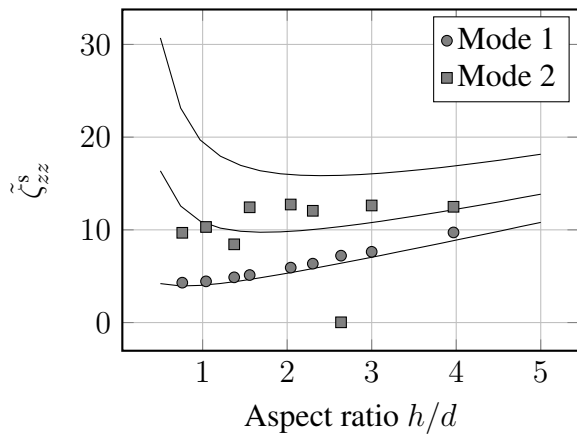
Figure 2.3: Stream function, ψ , for the single z -oriented eddy-current mode of a hollow spherical shell. The analytically-derived and numerically-computed stream functions are plotted against the polar angle, θ , measured from the z -axis. Because of the rotational symmetry, the stream function does not vary in the azimuthal direction, ϕ . Therefore, the eddy current, $\vec{J} = \hat{n} \times \nabla\psi$, must flow exclusively in the azimuthal direction.



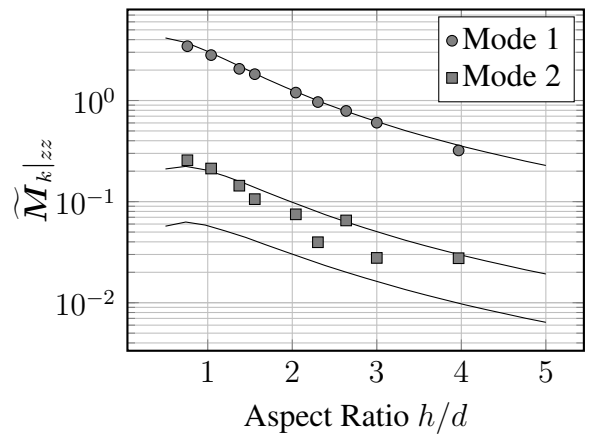
(a) Relaxation frequencies of transverse modes



(b) Polarizability coefficients of transverse modes



(c) Relaxation frequencies of longitudinal modes



(d) Polarizability coefficients of longitudinal modes

Figure 2.4: Longitudinal and transverse pole-expansion coefficients for thin conducting tubes plotted as a function of their aspect ratio, h/d . The coefficients were normalized by scaling the tubing dimensions so that they were inscribed by the unit sphere. © 2019 IEEE.

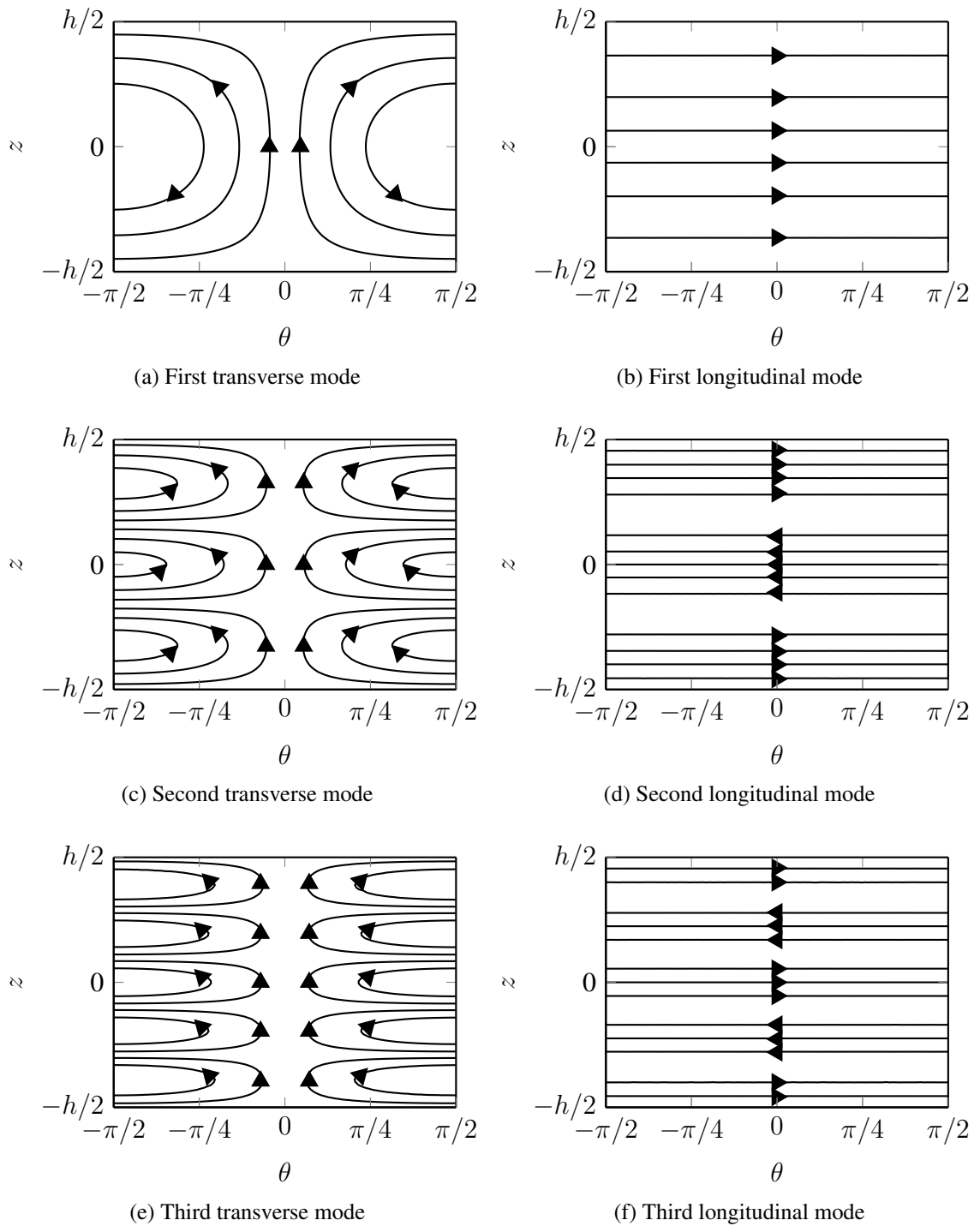


Figure 2.5: Current flow patterns for the first three longitudinal and transverse eddy-current modes of a conducting tube. Only one side of the tube is shown with the currents on the other side of the tube completing the contours. Two orthogonal modes can represent the transverse modes, y-directed modes (shown) and the x-directed modes which are identical after a 90° rotation. © 2019 IEEE.

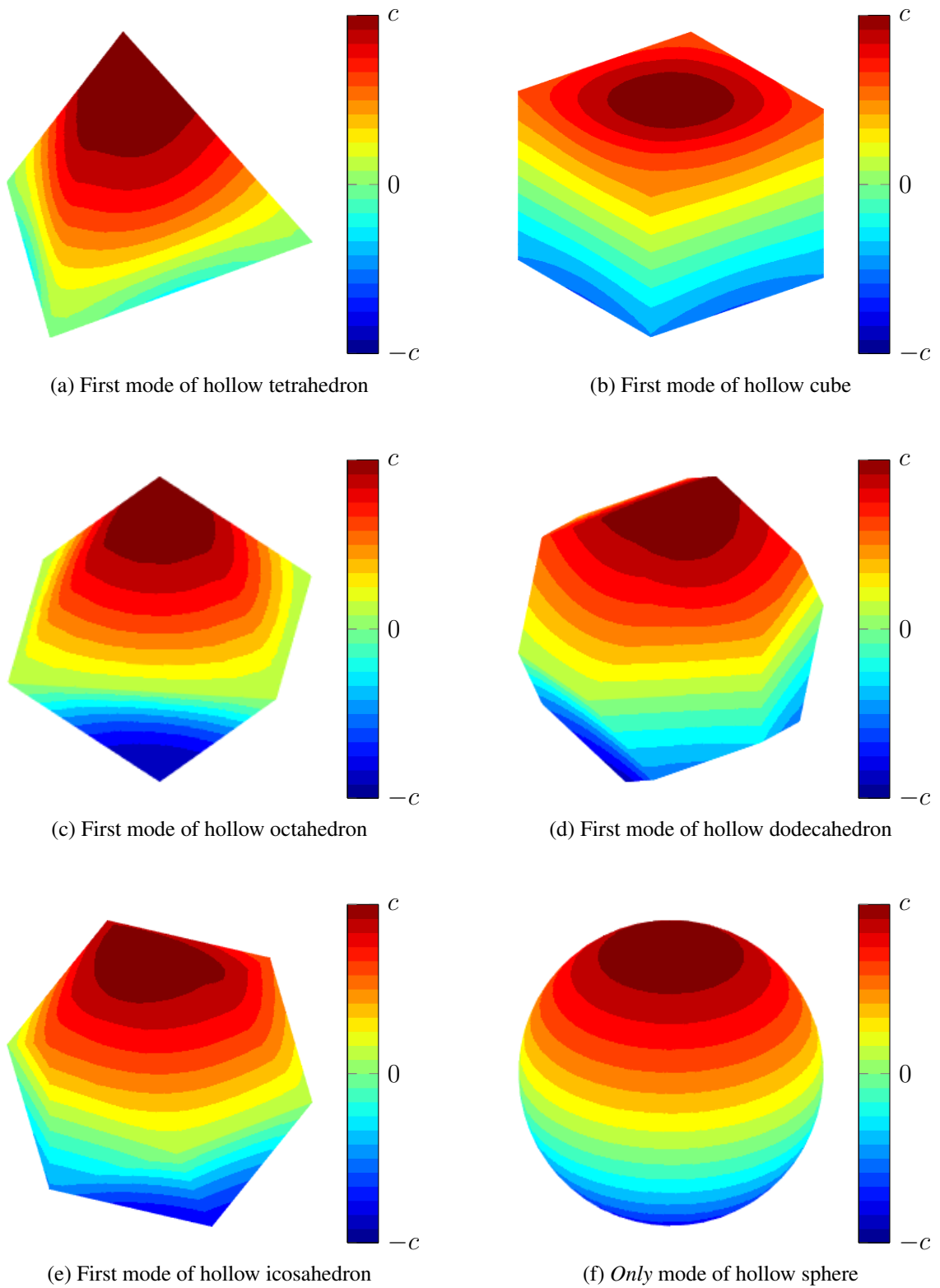


Figure 2.6: Contours of the stream function of the first modes of the hollow platonic solids and the only mode of the hollow sphere (with a non-zero dipole moment). Equal currents flow through each of the contours, and all currents flow in the same direction around the shell.

CHAPTER 3

CONDUCTING SOLIDS

3.1 Introduction

In this chapter, a method will be presented for computing the pole-expansion coefficients of the MPT of three-dimensional targets. To date, pole-expansion coefficients have not been computed for targets with arbitrary geometries, as previous characterizations of the pole-expansion coefficients of three-dimensional targets have been limited to targets with axial symmetry [4, 5]. Closed-form expressions have only been derived for spheres [6], and oblate and prolate spheroids [33]. Modeling general targets is important, because many targets of interest do not have rotational symmetry or are too thick to be accurately modeled by the approach in Chapter 2.

The method outlined in this chapter applies to sufficiently smooth, non-permeable targets without symmetry. It is an extension of the method in Chapter 2, with significant changes because of difficulties that are unique to three-dimensional analysis. A volume integral method is set up to satisfy Maxwell's equations, but a vector potential is used to represent the current density instead of a stream function. A tree-cotree projection is applied to the system matrices to remove their null spaces. The resultant linear system can be decomposed using a standard eigenvalue solver for dense matrices. The pole-expansion coefficients are then derived from the eigenvalues and eigenvectors. The method is verified by comparing the numerically-computed pole-expansion coefficients for a conducting sphere to their analytical values. The expansion coefficients for a sphere, cube and regular tetrahedron are compared to experimental data.

3.2 Electromagnetic Model

The primary aim of deriving a numerical model is to characterize the scattered magnetic field associated with the eddy currents that are induced in the conducting volume, Ω_c , by a time-varying magnetic excitation. Maxwell's equations in their time-harmonic form, under the eddy-current approximation, which allows displacement currents to be neglected, state that

$$\nabla \times \vec{H}(\vec{r}) = \vec{J}(\vec{r}) \quad (3.1a)$$

$$\nabla \times \vec{E}(\vec{r}) = -j\omega\vec{B}(\vec{r}) \quad (3.1b)$$

$$\nabla \cdot \vec{B}(\vec{r}) = 0 \quad (3.1c)$$

$$\nabla \cdot \vec{J}(\vec{r}) = 0. \quad (3.1d)$$

In addition, the constitutional relationships state that

$$\vec{B}(\vec{r}) = \mu\vec{H}(\vec{r}) \quad (3.2a)$$

$$\vec{J}(\vec{r}) = \sigma\vec{E}(\vec{r}), \quad (3.2b)$$

where μ is the permeability, and the electrical conductivity, σ , satisfies

$$\sigma = \begin{cases} \sigma_c & \text{in } \Omega_c \\ 0 & \text{in } \Omega \setminus \Omega_c. \end{cases} \quad (3.3)$$

If a vector potential, $\vec{B}(\vec{r}) = \nabla \times \vec{A}(\vec{r})$, is introduced, then Ampere's law (3.1a), can be satisfied by

$$\nabla^2(\vec{A}(\vec{r}) - \vec{A}^{\text{inc}}(\vec{r})) = -\mu_0\vec{J}(\vec{r}), \quad (3.4)$$

provided that the conducting and background media are assumed to be non-permeable. The incident magnetic vector potential, $\vec{\mathbf{A}}^{\text{inc}}$, represents the magnetic excitation in the absence of the conductor. Implicit in this separation is the assumption that the excitation is not significantly altered by the addition of the conductor.

The well-known fundamental solution to the three-dimensional Laplacian is

$$\nabla^2 \mathbf{G}(\vec{\mathbf{r}}) = -\delta(\vec{\mathbf{r}}), \quad (3.5)$$

where $\mathbf{G}(\vec{\mathbf{r}})$ is the free-space Green's function, $\mathbf{G}(\vec{\mathbf{r}}) = \frac{1}{4\pi r}$. Utilizing the Green's function, the magnetic vector potential due to the eddy currents flowing throughout a volume, V , can be written as

$$\vec{\mathbf{A}}(\vec{\mathbf{r}}) - \vec{\mathbf{A}}^{\text{inc}}(\vec{\mathbf{r}}) = \frac{\mu_0}{4\pi} \int_V \frac{\vec{\mathbf{J}}(\vec{\mathbf{r}}')}{\|\vec{\mathbf{r}} - \vec{\mathbf{r}}'\|} dV'. \quad (3.6)$$

When it is assumed that there is no charge built up in the computational domain, the electric field can be directly related to the magnetic vector potential while satisfying Faraday's law (3.1b), $\vec{\mathbf{E}}(\vec{\mathbf{r}}) = -j\omega\vec{\mathbf{A}}(\vec{\mathbf{r}})$. Substituting for the electric field and then subsequently substituting Ohm's law, $\vec{\mathbf{E}}(\vec{\mathbf{r}}) = \sigma^{-1}\vec{\mathbf{J}}(\vec{\mathbf{r}})$, into Eq. (3.6), we have

$$\sigma^{-1}\vec{\mathbf{J}}(\vec{\mathbf{r}}) + j\omega\frac{\mu_0}{4\pi} \int_V \frac{\vec{\mathbf{J}}(\vec{\mathbf{r}}')}{\|\vec{\mathbf{r}} - \vec{\mathbf{r}}'\|} dV' = -j\omega\vec{\mathbf{A}}^{\text{inc}}(\vec{\mathbf{r}}). \quad (3.7)$$

Eq. (3.7) relates the eddy currents, $\vec{\mathbf{J}}(\vec{\mathbf{r}})$ that flow in the conductor due to the magnetic excitation, $\vec{\mathbf{A}}^{\text{inc}}(\vec{\mathbf{r}})$.

3.3 Numerical Strategy

3.3.1 Discretization and Choice of Basis Functions

Divergence-conforming constant normal/linear tangential (CN/LT) basis functions were chosen to expand the current density,

$$\vec{\mathbf{J}}(\vec{\mathbf{r}}) \approx \sum_{m=1}^{\mathcal{N}(\text{f})} \mathbf{j}_m^{\text{f}} \vec{\mathbf{w}}_m^{\text{f}}(\vec{\mathbf{r}}), \quad (3.8)$$

where \mathbf{j}_m^{f} are the face-associated unknowns, and

$$\vec{\mathbf{w}}^{\text{f}} = 2(\lambda_i \nabla \lambda_j \times \nabla \lambda_k + \lambda_j \nabla \lambda_k \times \nabla \lambda_i + \lambda_k \nabla \lambda_i \times \nabla \lambda_j), \quad (3.9)$$

where $\lambda_{\{i,j,k\}}$ are the barycentric coordinates of the associated faces of the tetrahedron.

Applying Galerkin's method, the discrete version of Eq. (3.7) can be written as

$$\mathbf{R}\mathbf{j} + j\omega\mathbf{L}\mathbf{j} = -j\omega\mathbf{a}^{\text{inc}}, \quad (3.10)$$

where the following matrices must be computed for each basis function pair

$$\mathbf{L}_{ij} = \frac{\mu_0}{4\pi} \iint \frac{\vec{\mathbf{w}}_i(\vec{\mathbf{r}}) \cdot \vec{\mathbf{w}}_j(\vec{\mathbf{r}}')}{\|\vec{\mathbf{r}} - \vec{\mathbf{r}}'\|} dV' dV \quad (3.11)$$

$$\mathbf{R}_{ij} = \int \sigma^{-1} \vec{\mathbf{w}}_i(\vec{\mathbf{r}}) \cdot \vec{\mathbf{w}}_j(\vec{\mathbf{r}}) dV \quad (3.12)$$

$$\mathbf{a}^{\text{f, inc}} = \int \vec{\mathbf{w}}_i(\vec{\mathbf{r}}) \cdot \vec{\mathbf{A}}^{\text{inc}} dV. \quad (3.13)$$

Since divergence-conforming (CN/LT) basis functions were chosen, Eq. (3.7) does not, on its own, constrain the solenoidality of the current density.

Despite the finite divergence of the basis functions over their respective domains, the functions are a natural choice to represent the current density, which is solenoidal, because they force normal continuity across cell boundaries while allowing for simple enforcement

of boundary conditions. By eliminating unknowns associated with the faces on the boundary of the conductor, eddy-current flow is confined to the conducting material. The total divergence inside each tetrahedral cell can be forced to zero by utilizing a sparse topological matrix to constrain the basis-function coefficients.

3.3.2 Discrete Curl Matrix

Enforcing the solenoidality of the current density using a topological matrix is akin to defining a vector potential, $\vec{T}(\vec{r})$, for the current density,

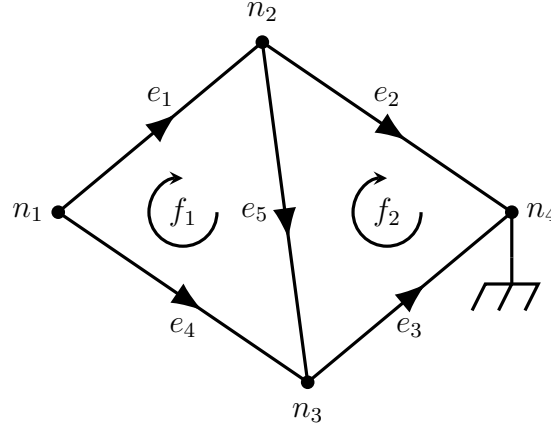
$$\vec{J}(\vec{r}) = \nabla \times \vec{T}(\vec{r}), \quad (3.14)$$

which forces $\vec{J}(\vec{r})$ to be solenoidal, since $\nabla \cdot (\nabla \times \vec{T}(\vec{r})) = 0$. On a discrete mesh, this corresponds to

$$\mathbf{j}^f = \mathbf{C} \mathbf{t}^e, \quad (3.15)$$

where \mathbf{j}^f are the face-associated current density unknowns, \mathbf{C} is the topological edge-face incidence matrix, and the potential unknowns, \mathbf{t}^e , are associated with the mesh edges. For a given mesh, in which each simplex has been assigned an orientation, the sparse edge-face incidence matrix has entries

$$\mathbf{C}_{ij} = \begin{cases} -1, & \text{if the } j\text{th edge is oriented negatively} \\ & \text{with respect to the } i\text{th face} \\ +1, & \text{if the } j\text{th edge is oriented positively} \\ & \text{with respect to the } i\text{th face} \\ 0, & \text{otherwise.} \end{cases} \quad (3.16)$$



$$\mathbf{G} = \begin{bmatrix} -1 & +1 & & & \\ -1 & & +1 & & \\ & -1 & +1 & & \\ & -1 & & & \\ & & & -1 & \end{bmatrix} \quad \mathbf{C} = \begin{bmatrix} +1 & -1 & +1 & & \\ & & -1 & +1 & -1 \end{bmatrix}$$

Figure 3.1: Example graph with $\mathcal{N} = 4$, $\mathcal{E} = 5$, $\mathcal{F} = 2$. All nodes are positively oriented by convention, and the reference node is n_4 . The orientation of each of the edges and faces is denoted by an arrowhead. For this graph, the node-edge incidence matrix, \mathbf{G} , and the edge-face incidence matrix, \mathbf{C} , are given. It can be trivially seen that $\mathbf{C}\mathbf{G} = \mathbf{0}$.

Using Eq. (3.15) to constrain the current density unknowns in Eq. (3.10), and multiplying on the left by \mathbf{C}^T to maintain symmetry, results in the following matrix equation:

$$\mathbf{C}^T \mathbf{R} \mathbf{C} \mathbf{t}^e + j\omega \mathbf{C}^T \mathbf{L} \mathbf{C} \mathbf{t}^e = \mathbf{C}^T \mathbf{a}^{f, \text{inc}}. \quad (3.17)$$

3.3.3 Tree-Cotree Decomposition and Projection

While introducing a potential through a topological matrix helps by constraining the divergence of the current density, it creates two distinct difficulties in the process. First, the boundary conditions for the current density can no longer be enforced by eliminating current density unknowns on the conductor boundary. Although potential unknowns are linearly related to current density unknowns, it is not immediately obvious how to constrain the potential unknowns so that the current density unknowns through the conductor

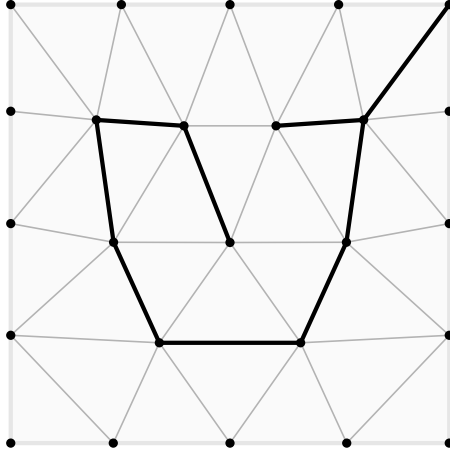


Figure 3.2: One of many tree-cotree decompositions relative to the boundary of a simple graph. The boundary is the set of edges on the exterior. One of the many possible trees is shown in bold, while the cotree edges are grayed out. Note that the tree does not close a cycle with itself or with the boundary.

boundary are zero, so that current does not exit the conducting region. Second, the potential is not unique, since many different fields can have the same curl. In other words, the topological matrix, C , has a large null space, and only a fraction of its unknowns are essential.

The large null space associated with the topological matrix, C , can be understood in the context of another topological matrix, the node-edge incidence matrix, G , with entries

$$G_{ij} = \begin{cases} -1, & \text{if the } i\text{th edge is oriented negatively} \\ & \text{with respect to the } j\text{th node,} \\ +1, & \text{if the } i\text{th edge is oriented positively} \\ & \text{with respect to the } j\text{th node,} \\ 0, & \text{otherwise.} \end{cases} \quad (3.18)$$

An illustration of a graph and the corresponding G and C matrices is given in Fig. 3.1. The two topological matrices satisfy the relation $CG = 0$, which is the discrete analogue of the vector calculus identity $\nabla \times (\nabla\phi) = 0$. Finding the generalized eigenvalues of

$C^T LC$ and $C^T RC$ is non-trivial, because the eigenvalue problem is singular, since every column of G is in the null space of both system matrices. Fortunately, both this difficulty, and the enforcement of boundary conditions can be addressed by eliminating non-essential unknowns from C .

A minimum spanning tree is a subset of edges of a graph that connects all the vertices together, without closing any cycles. The remaining edges are called cotree edges. The choice of tree and cotree edges is not unique; however, the number of edges in each partition is always the same. A minimum spanning tree relative to the boundary (mod Δ) is a subset of edges whose union with the subset of boundary edges does not close a cycle [9]. The tree of a simple graph is shown in Fig. 3.2. Finding the tree-cotree decomposition for complex topologies, such as an toroid, requires extra care as generators must be added to the tree to account for topological currents [34].

Decomposing the potential unknowns, t^e , into tree and cotree unknowns relative to the conductor boundary, ensures that no eddy currents can flow out of the conducting region. Once a spanning tree is chosen, the non-essential degrees of freedom can be eliminated by permuting the columns and rows of G , C and t^e ,

$$G = \begin{bmatrix} G_t \\ G_c \end{bmatrix} \quad C = \begin{bmatrix} C_t & C_c \end{bmatrix} \quad t^e = \begin{bmatrix} t_t^e \\ t_c^e \end{bmatrix}, \quad (3.19)$$

where G_t , C_t , and t_t^e contain only the tree-associated rows and columns of the original matrices, and G_c , C_c , and t_c^e contain only the cotree-associated rows and columns. The tree node-edge incidence matrix, G_t , is square. Choosing $t^e \perp G$ so that the potential is orthogonal to the null space gives

$$G^T t^e = G_t^T t_t^e + G_c^T t_c^e = 0, \quad (3.20)$$

which can be simplified to

$$\mathbf{t}_t^e = -(\mathbf{G}_t^T)^{-1} \mathbf{G}_c \mathbf{t}_c^e, \quad (3.21)$$

because \mathbf{G}_t is invertible. Using this relation, the full potential vector can be written as

$$\mathbf{t}^e = \begin{bmatrix} -(\mathbf{G}_t^T)^{-1} \mathbf{G}_c \\ \mathbf{I}_c \end{bmatrix} \mathbf{t}_c^e = \mathbf{W} \mathbf{t}_c^e, \quad (3.22)$$

where \mathbf{I}_c is the identity matrix, with dimension equal to the number of cotree edges, and \mathbf{W} maps \mathbf{t}_c^e to \mathbf{t}^e such that $\mathbf{t}^e \perp \mathbf{G}$. Substituting Eq. (3.22) into Eq. (3.17) and multiplying on the left by \mathbf{W}^T gives a full rank matrix equation,

$$\underbrace{\mathbf{W}^T \mathbf{C}^T \mathbf{R} \mathbf{C} \mathbf{W}}_{\mathbf{R}_{CW}} \mathbf{t}_c^e + j\omega \underbrace{\mathbf{W}^T \mathbf{C}^T \mathbf{L} \mathbf{C} \mathbf{W}}_{\mathbf{L}_{CW}} \mathbf{t}_c^e = \mathbf{W}^T \mathbf{C}^T \mathbf{a}^{f, inc}, \quad (3.23)$$

which may be written concisely as

$$\mathbf{R}_{CW} \mathbf{t}_c^e + j\omega \mathbf{L}_{CW} \mathbf{t}_c^e = \mathbf{W}^T \mathbf{C}^T \mathbf{a}^{f, inc}. \quad (3.24)$$

In contrast to the generalized eigenvalue problem of $\mathbf{C}^T \mathbf{L} \mathbf{C}$ and $\mathbf{C}^T \mathbf{R} \mathbf{C}$, which is singular, there is an equivalent generalized eigenvalue problem which is non-singular,

$$\mathbf{L}_{CW} \mathbf{v} = \lambda \mathbf{R}_{CW} \mathbf{v}, \quad (3.25)$$

or

$$\mathbf{L}_{CW} \mathbf{V} = \mathbf{R}_{CW} \mathbf{\Lambda} \mathbf{V}, \quad (3.26)$$

where each \mathbf{v} is an eigenvector, λ is the corresponding eigenvalue, $\mathbf{V} = [\mathbf{v}_1, \mathbf{v}_2, \dots, \mathbf{v}_K]$ is the matrix of eigenvectors, and $\mathbf{\Lambda} = \text{diag}[\lambda_1, \lambda_2, \dots, \lambda_K]$ is the diagonal matrix of eigenvalues. The generalized eigenvalues and eigenvectors of this non-singular, dense, symmetric, and positive definite matrix pencil can be found using a standard eigenvalue solver.

3.3.4 Pole Expansion Derivation

The generalized eigenvalues and eigenvectors of Eq. (5.47) can be used to expand Eq. (3.17) into pole-expansion form by first recognizing that

$$\mathbf{R}_{\text{CW}} = \mathbf{R}_{\text{CW}} \mathbf{V} \mathbf{V}^T \mathbf{R}_{\text{CW}} \quad (3.27)$$

$$\mathbf{L}_{\text{CW}} = \mathbf{R}_{\text{CW}} \mathbf{V} \mathbf{\Lambda} \mathbf{V}^T \mathbf{R}_{\text{CW}}, \quad (3.28)$$

which derives from the \mathbf{R}_{CW} -orthogonality of the eigenvectors, $\mathbf{V}^T \mathbf{R}_{\text{CW}} \mathbf{V} = \mathbf{I}$. The pencil can then be written as

$$\mathbf{R}_{\text{CW}} + j\omega \mathbf{L}_{\text{CW}} = \mathbf{R}_{\text{CW}} \mathbf{V} (\mathbf{I} + j\omega \mathbf{\Lambda}) \mathbf{V}^T \mathbf{R}_{\text{CW}}. \quad (3.29)$$

If Eq. (3.29) is multiplied on the left by \mathbf{V}^T and on the right by \mathbf{V} , then

$$\mathbf{V}^T (\mathbf{R}_{\text{CW}} + j\omega \mathbf{L}_{\text{CW}}) \mathbf{V} = (\mathbf{I} + j\omega \mathbf{\Lambda}). \quad (3.30)$$

Taking the inverse of the pencil, provided that ω does not coincide with a pole, results in

$$\begin{aligned} (\mathbf{V}^T (\mathbf{R}_{\text{CW}} + j\omega \mathbf{L}_{\text{CW}}) \mathbf{V})^{-1} &= (\mathbf{I} + j\omega \mathbf{\Lambda})^{-1} \\ \mathbf{V}^{-1} (\mathbf{R}_{\text{CW}} + j\omega \mathbf{L}_{\text{CW}})^{-1} (\mathbf{V}^T)^{-1} &= (\mathbf{I} + j\omega \mathbf{\Lambda})^{-1} \\ (\mathbf{R}_{\text{CW}} + j\omega \mathbf{L}_{\text{CW}})^{-1} &= \mathbf{V} (\mathbf{I} + j\omega \mathbf{\Lambda})^{-1} \mathbf{V}^T, \end{aligned} \quad (3.31)$$

which can be written in summation form as

$$(\mathbf{R}_{\text{CW}} + j\omega \mathbf{L}_{\text{CW}})^{-1} = \sum_{k=1}^K (1 + j\omega \lambda_k)^{-1} \mathbf{v}_k \mathbf{v}_k^T. \quad (3.32)$$

Using Eq. (3.32), it is possible to solve for the cotree-associated vector potential unknowns in Eq. (3.24),

$$\mathbf{t}_c^e = - \sum_{k=1}^K \frac{j\omega\lambda_k}{1 + j\omega\lambda_k} \lambda_k^{-1} \mathbf{v}_k \mathbf{v}_k^T \mathbf{W}^T \mathbf{C}^T \mathbf{a}^{\text{f, inc}}. \quad (3.33)$$

Multiplying Eq. (3.34) on the left by $\mathbf{C}\mathbf{W}$, and noting from Eq. (3.15) and Eq. (3.22) that $\mathbf{j}^{\text{f}} = \mathbf{C}\mathbf{W}\mathbf{t}_c^e$, gives

$$\mathbf{j}^{\text{f}} = - \sum_{k=1}^K \frac{j\omega\lambda_k}{1 + j\omega\lambda_k} \lambda_k^{-1} \mathbf{C}\mathbf{W} \mathbf{v}_k \mathbf{v}_k^T \mathbf{W}^T \mathbf{C}^T \mathbf{a}^{\text{f, inc}}, \quad (3.34)$$

where the eigenvalues can be identified as the reciprocal of the relaxation frequencies associated with the eddy-current modes. The magnetic polarizability of each of the current density modes can be computed from their magnetic dipole moments,

$$\vec{\mathbf{m}} = \frac{1}{2} \int_V \vec{\mathbf{r}} \times \vec{\mathbf{J}}(\vec{\mathbf{r}}) dV, \quad (3.35)$$

which, in turn, can be evaluated using quadrature. The magnetic dipole moments are computed for eddy currents supported by excitations, $\vec{\mathbf{A}}^{\text{inc}}$, that correspond to \hat{x} -, \hat{y} -, and \hat{z} -directed uniform magnetic fields¹. Then, the components of the magnetic polarizabilities are inverted from the magnetic moments using the relation

$$\vec{\mathbf{m}} = \mathbf{M} \cdot \vec{\mathbf{H}}^{\text{inc}}. \quad (3.36)$$

The three magnetic excitations provide a full-rank basis, which is sufficient to invert the tensor components.

¹These $\vec{\mathbf{A}}^{\text{inc}}$ are not unique, and many compatible fields could have been chosen. In this work, for example, $\vec{\mathbf{A}}^{\text{inc}} = -\frac{1}{2}\mu_0(y\hat{x} - x\hat{y})$ was chosen for the \hat{z} -directed excitation.

3.4 Numerical Implementation

The numerical code was implemented in MATLAB on a hex-core, 3.4 GHz Intel i7, with 64 GB of memory. Tetrahedral meshes for a sphere were generated in `DistMesh` [28], using the function `distmeshnd`. `Gmsh` [29] was chosen to mesh the more irregular conductor shapes, that couldn't be meshed straightforwardly by `DistMesh`. The MATLAB function `graphminspantree`, an implementation of Prim's algorithm [35], was used to find the minimum spanning tree of a graph from its adjacency matrix. The 500 smallest eigenvalues and their corresponding eigenvectors were computed using `eigs`, MATLAB's wrapper for `ARPACK` [36]. The weakly-singular integrals in Eq. (3.11) for the overlapping tetrahedral domains were computed using a singularity cancellation strategy outlined in [37]. The outer integral was performed using a Gauss-Legendre rule for tetrahedrons [38], while the inner transformed integral was performed using a one-dimensional Gauss-Legendre rule in each of the three transformed dimensions. Terms where the integration domains did not overlap were computed by applying two successive Gauss-Legendre rules for tetrahedrons.

3.5 Results

3.5.1 Spherical Conductor

The solid spherical conductor is one of the few target geometries for which it is possible to derive the pole-expansion coefficients analytically [6]. The high degrees of target symmetry cause the magnetic polarizability to be isotropic, meaning that one coefficient is sufficient to characterize each of its frequency-dependent MPTs.

In Fig. 3.3, the spherical conductor's pole-expansion coefficients are plotted as a stem plot, with the normalized relaxation frequencies, $\tilde{\zeta}_k$, determining the stem locations, and the zz -component of the normalized diagonal tensor coefficients, $\widetilde{\mathcal{M}}_k|_{zz}$, determining the amplitudes. These coefficients can be scaled according to Eq. (1.4) and Eq. (1.5). Both

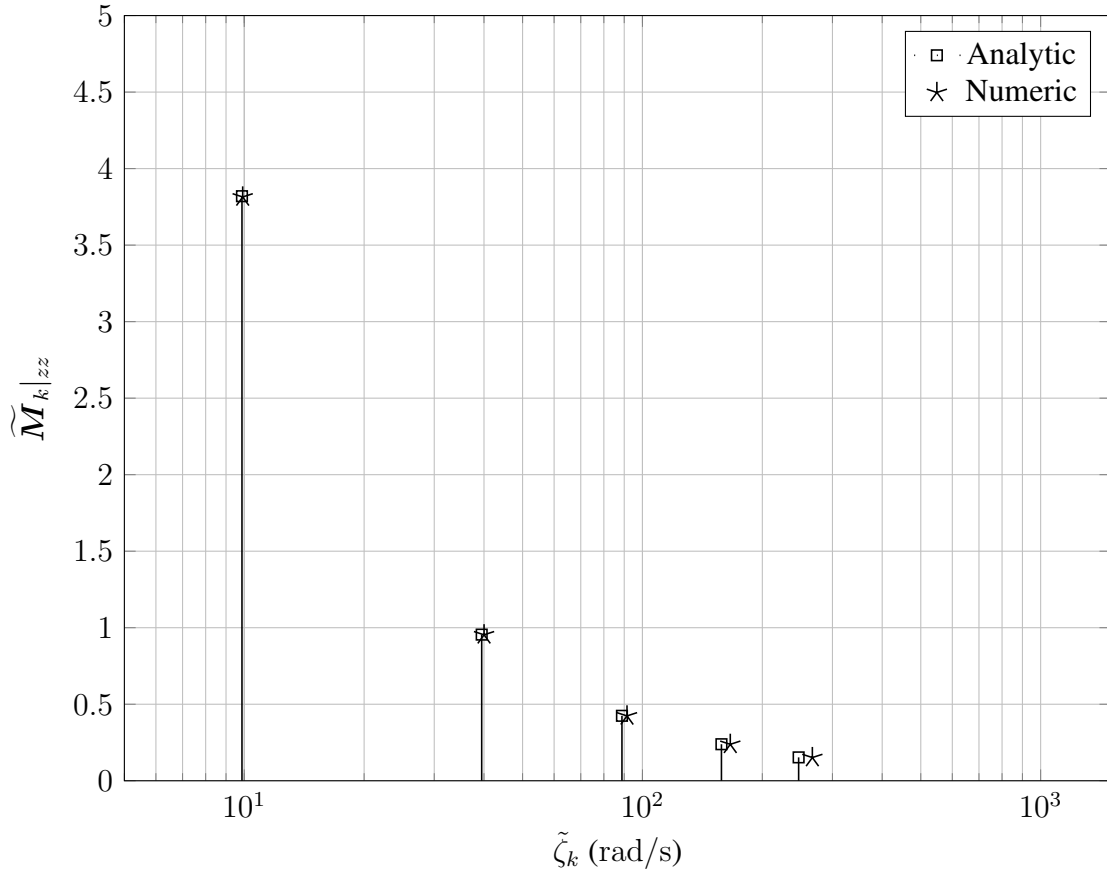


Figure 3.3: Normalized pole-expansion coefficients of a spherical conductor. Since a sphere is an isotropic target, its polarizability tensors are diagonal, with equal entries along the diagonal.

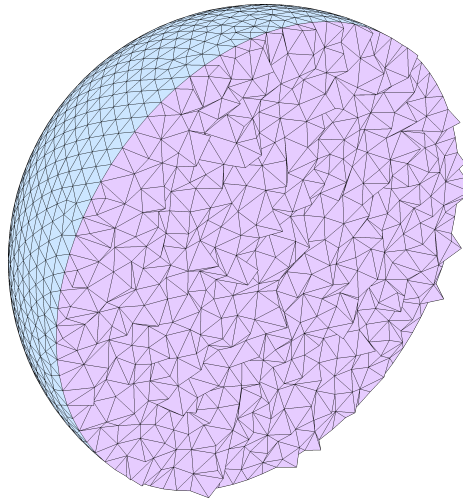


Figure 3.4: Cutout of the mesh of a sphere that was used to derive the pole-expansion coefficients and draw the mode graphs. This mesh has 45,319 tetrahedra, which corresponds to 42,543 cotree unknowns.

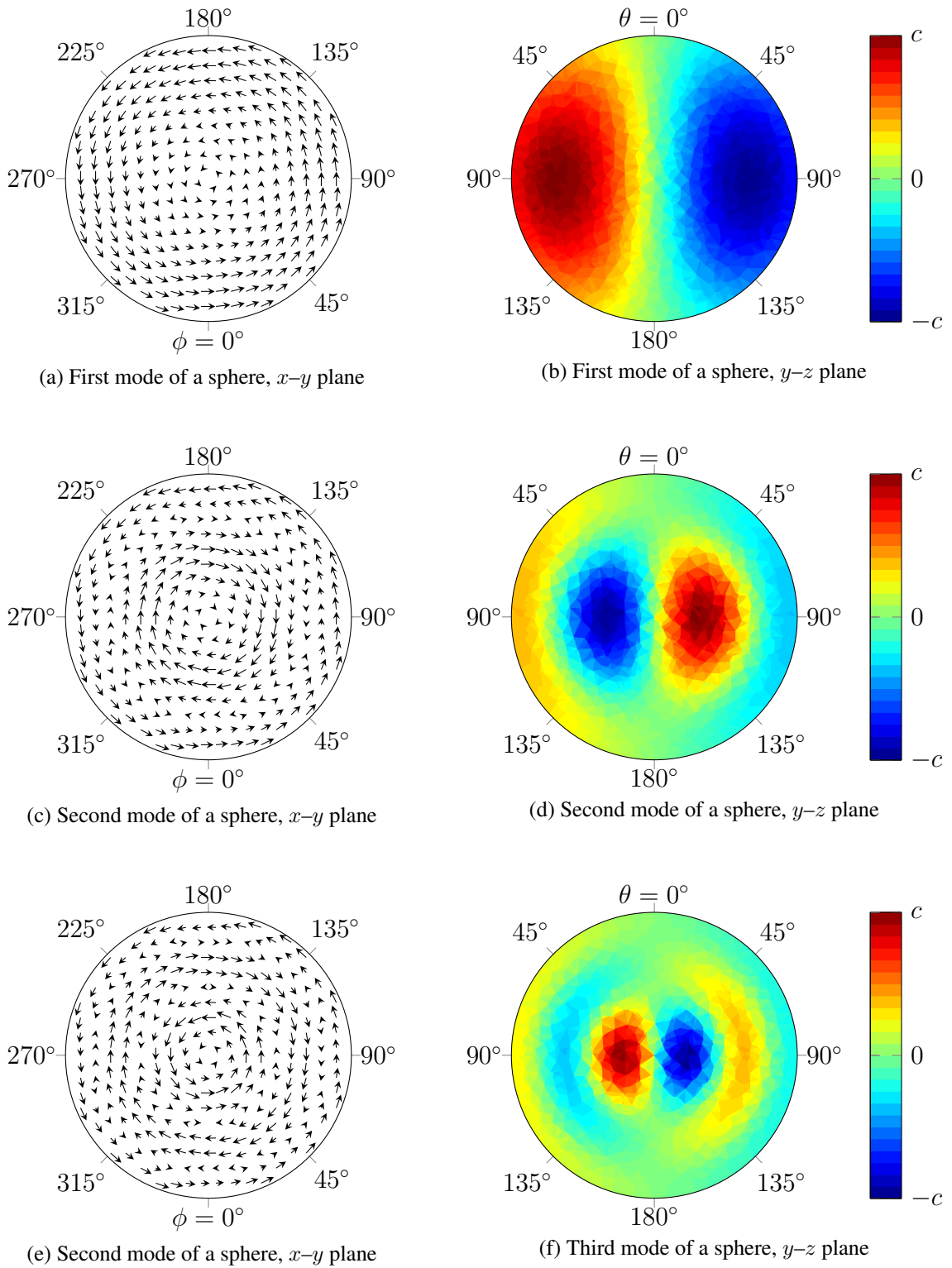


Figure 3.5: Slices of the first three modes of a spherical conductor, computed using a volume integral method. The quiver plots illustrate the direction of current flow in the x - y plane. The color plots graph the amplitude of the current density flowing through the y - z plane.

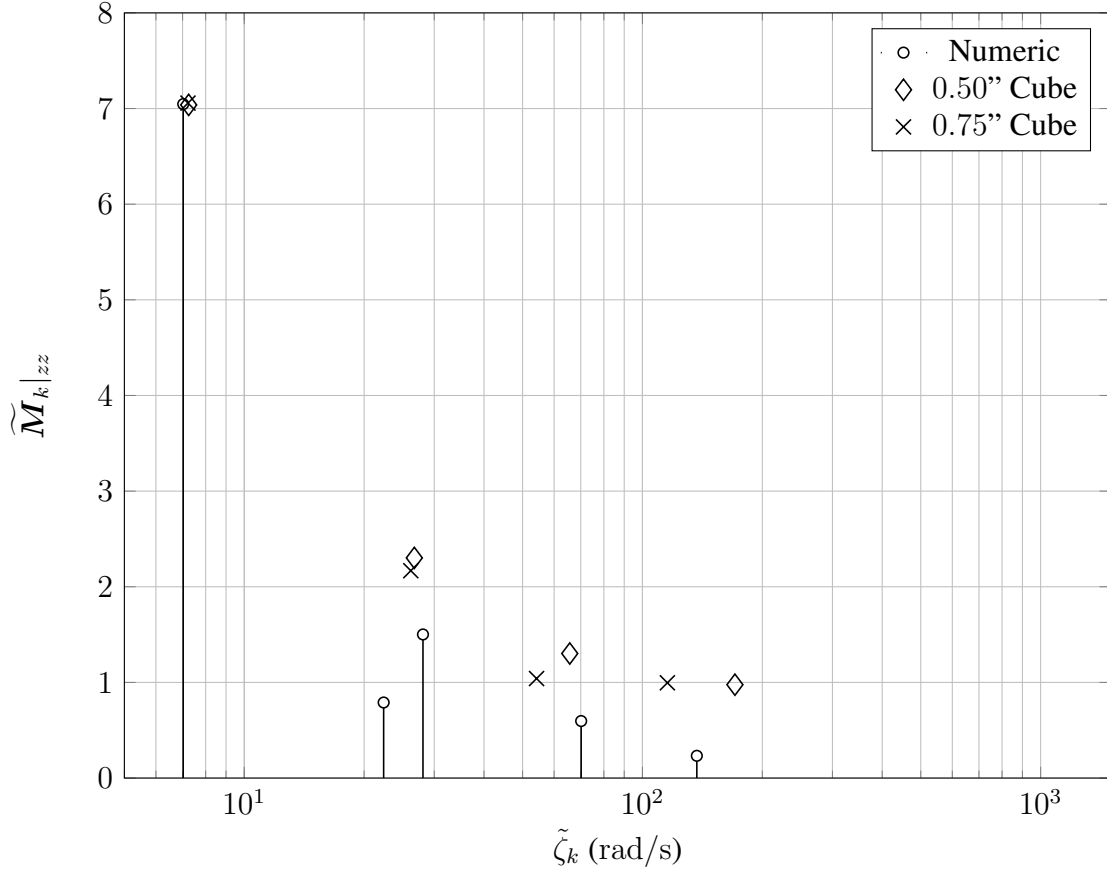


Figure 3.6: Normalized pole-expansion coefficients of a cubical conductor. Since a cube is an isotropic target, its polarizability tensors are diagonal, with all of its non-zero entries being equal.

the numerically-computed coefficients and their analytical values are shown. In Fig. 3.4, a cutout of the mesh used to derive these coefficients is shown. Even for a relatively coarse discretization, with only 45,319 tetrahedra, the numerically-computed coefficients show good agreement with their analytical counterparts. In Fig. 3.5, the first three modes of the sphere are shown (that have a non-zero dipole moment). For each mode, two slices of the current density are shown: the first slice is a quiver plot of the current density in the x - y plane, and the second slice is a color plot depicting the amplitude of the current in the y - z plane.

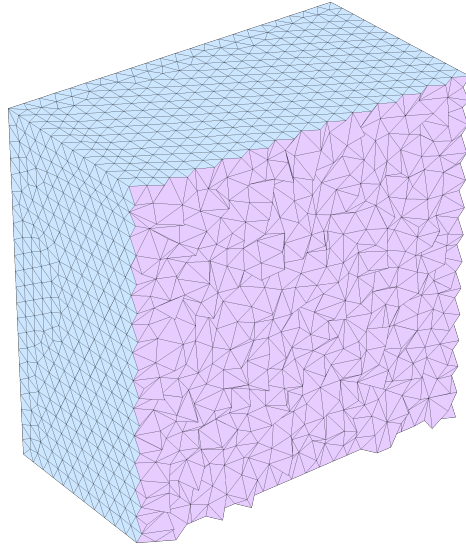
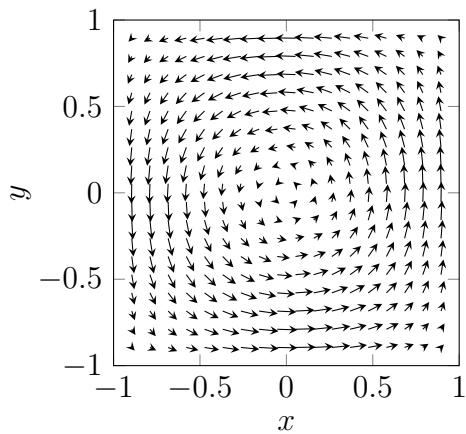


Figure 3.7: Cutout of the cubical mesh used to draw the mode graphs. This mesh has 49,728 tetrahedra, which corresponds to 46,259 cotree unknowns.

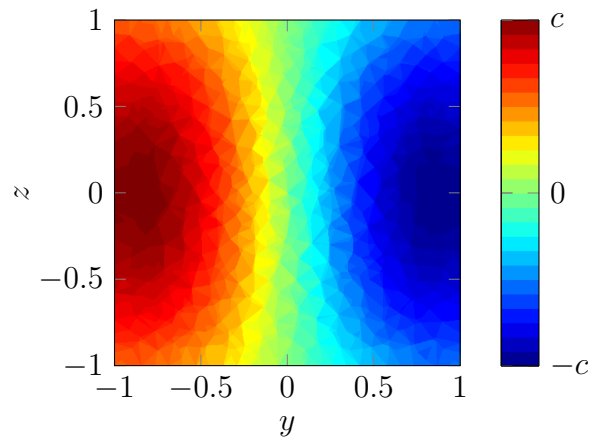
3.5.2 Cubical Conductor

While a cube also has an isotropic response, its pole-expansion coefficients are not known to have a closed-form solution. The pole-expansion coefficients can, however, be inverted from experimental data. For this purpose, two aluminum cubes with edge lengths of 0.5” and 0.75” were measured, normalized, and plotted alongside the coefficients that were computed numerically. The comparison between measured and numerical results is shown in Fig. 3.6. In Fig. 3.7, a cutout of the mesh used to derive the coefficients is shown. In Fig. 3.8, the first three modes of the cube are shown (that have a non-zero dipole moment). For each mode, two slices of the current density are shown: the first slice is a quiver plot of the current density in the x - y plane, and the second slice is a color plot of the amplitude of the current in the y - z plane.

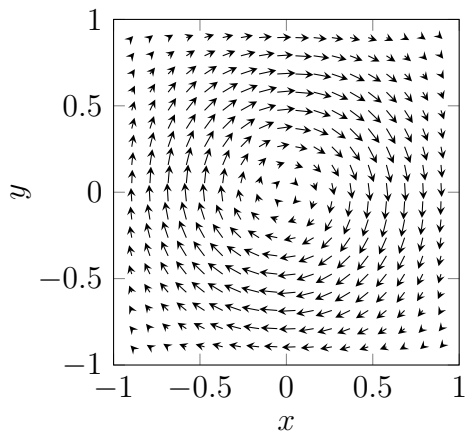
In Fig. 3.6, the first pole of the numerically-derived coefficients and the measurement agree very well, but the other poles are only in rough agreement. Other than the dominant pole, the remaining coefficients that were inverted from the measurement are likely to be inaccurate for this example. Inversions of measured data are prone to inaccuracies when the



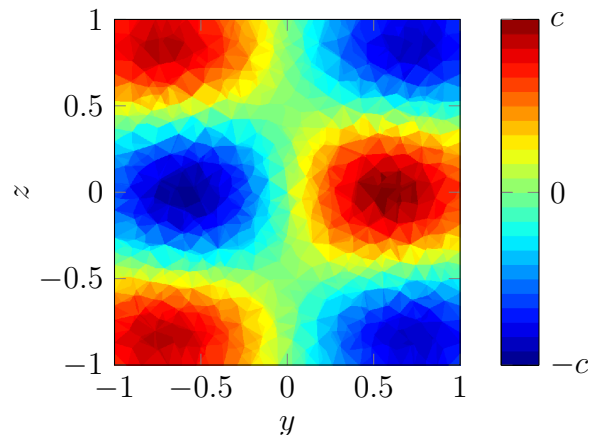
(a) First mode of a cube, x - y plane



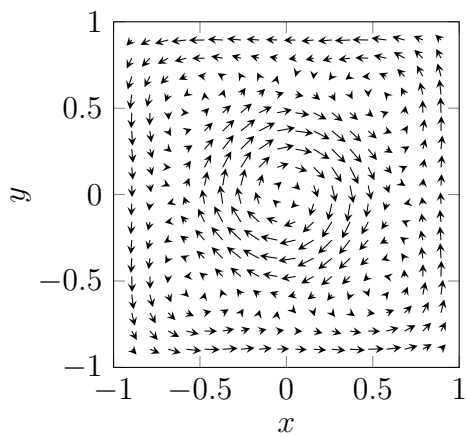
(b) First mode of a cube, y - z plane



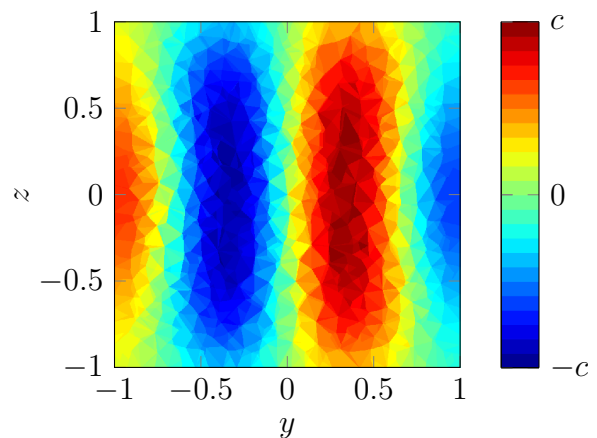
(c) Second mode of a cube, x - y plane



(d) Second mode of a cube, y - z plane



(e) Third mode of a cube, x - y plane



(f) Third mode of a cube, y - z plane

Figure 3.8: Slices of the first three modes of a cubical conductor, computed using a volume integral method. The quiver plots illustrate the direction of current flow in the x - y plane. The color plots graph the amplitude of the current density flowing through the y - z plane.

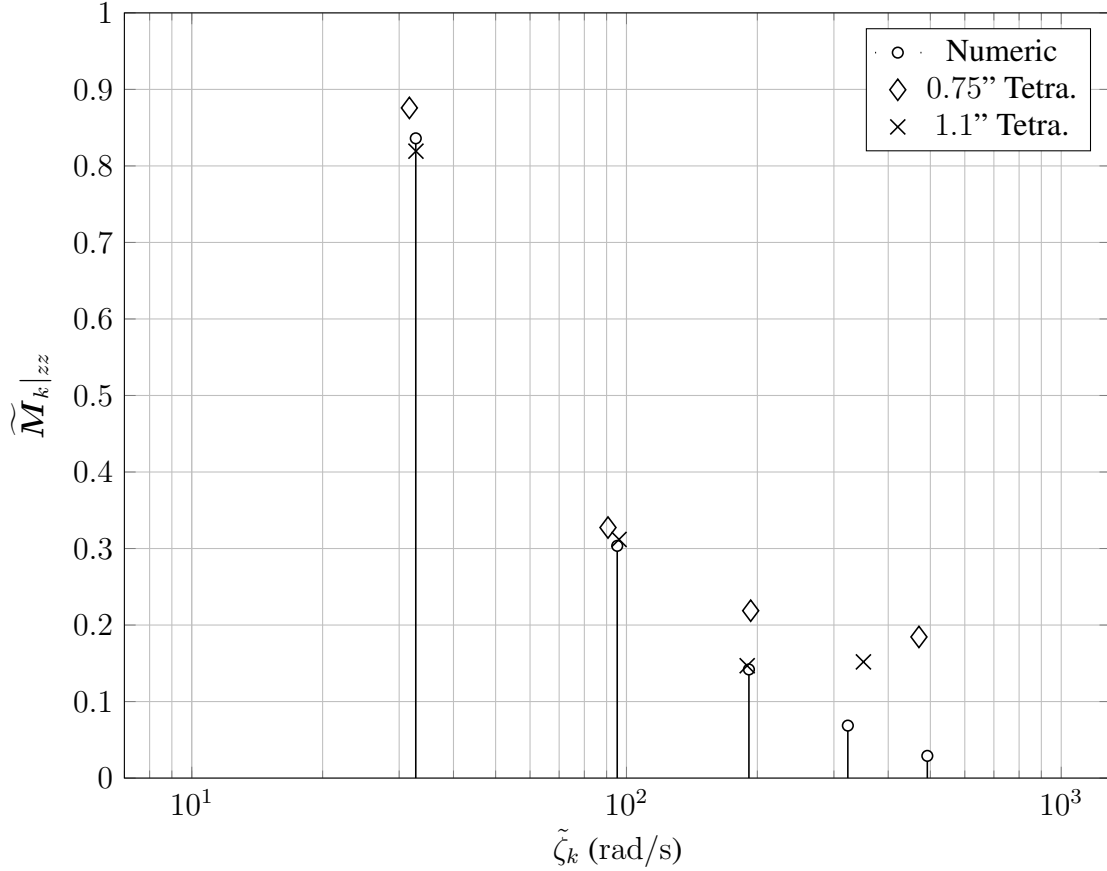


Figure 3.9: Normalized pole-expansion coefficients of a tetrahedral conductor. Since a tetrahedron is an isotropic target, its polarizability tensors are diagonal, with all of its non-zero entries being equal.

two poles are not sufficiently distant. such is the case with the second and third poles of the conducting cube. Because the two poles have similar relaxation frequencies, they are not sufficiently differentiated from one another, and the inversion combines the two relaxations, placing a larger amplitude coefficient between the two relaxation frequencies. Coefficients that are over an order of magnitude smaller than the dominant tensor coefficient also cannot be inverted reliably. This explains the comparatively poor agreement between numerical and experimental results, and also highlights the importance of numerically modeling the coefficients, rather than simply relying on inversions of measured data.

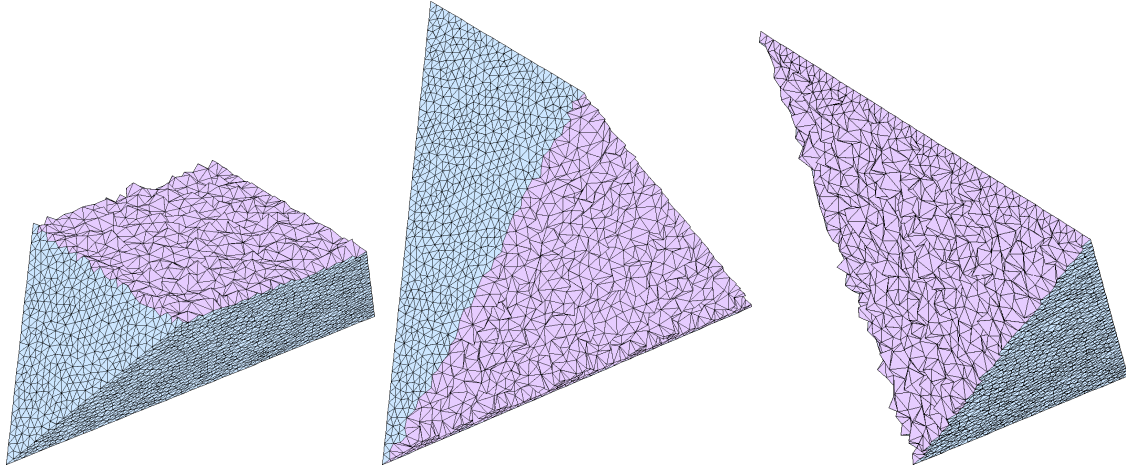


Figure 3.10: Cutouts of the tetrahedral mesh used to draw the mode graphs. This mesh has 47,001 tetrahedra, which corresponds to 29,796 cotree unknowns.

3.5.3 Regular Tetrahedron

Like both spheres and cubes, the regular tetrahedron has an isotropic MPT. Like the cube, the pole-expansion coefficients cannot be derived analytically; therefore, the numerical results could only be compared to inverted measured data. For this purpose, aluminum tetrahedrons with edge lengths of 0.75” and 1.1” were measured, normalized, and plotted alongside the numerically-computed coefficients. Because of practical manufacturing limitations, the dihedral angles between the base of the tetrahedron and each of the remaining faces were 71.00° , rather than 70.53° , which is the dihedral angle between the faces of a regular tetrahedron. The inversion still assumed the target was isotropic.

In Fig. 3.9, the numerically-computed coefficients are compared to measured data. The first two poles of the numerical computation and the measurement agree very well, but the third and fourth poles are only in rough agreement. This improved accuracy over the cube is because the poles of the regular tetrahedron are sufficiently distant so as not to mix. The errors in the measured third and fourth pole-expansion coefficients are expected because of their small relative amplitude. In Fig. 3.10, cutouts of the mesh used to derive the coefficients are shown. In Fig. 3.11, the first three modes of the tetrahedron are shown (that have a non-zero dipole moment). For each mode, three slices of the current density

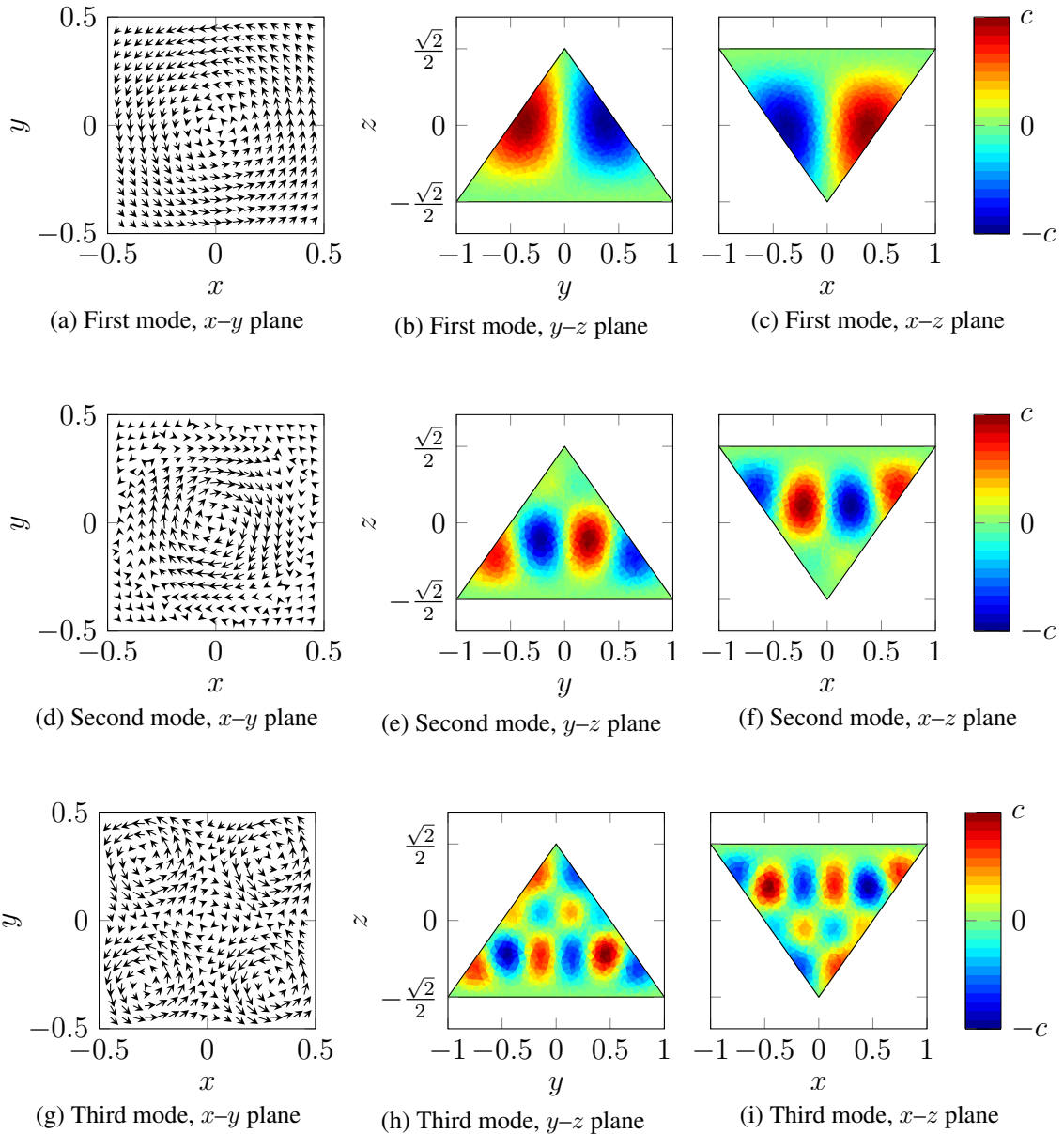


Figure 3.11: Slices of the first three modes of a conducting regular tetrahedron, computed using a volume integral method. The quiver plots illustrate the direction of current flow in the x - y plane. The color plots graph the amplitude of the current density flowing through the x - z and y - z planes.

are shown: the first slice is a quiver plot of the current in the x - y plane, the second is a color plot of the amplitude of the current in the y - z plane, and the third slice is a color plot of the amplitude of the current in the x - z plane.

3.6 Conclusion

In this chapter, a volume integral method was presented for numerically computing the pole-expansion coefficients of arbitrary three-dimensional targets. The method relies on a vector potential to enforce a quasi-magnetostatic assumption on the current density as well as to enforce the appropriate boundary conditions. The coefficients can then be derived using a simple eigendecomposition of system matrices. It was, however, first necessary to project the linear system away from its null space, to avoid setting up an ill-posed generalized eigenvalue problem.

To demonstrate the validity of the method, numerical results were compared to the analytically-derived coefficients for a conducting sphere. Both sets of coefficients showed good agreement. For experimental validation, two sets of shapes were chosen, cubes and regular tetrahedrons. The higher-order coefficients of the cubes showed poor agreement with the numerically-computed coefficients. This is most likely due to the close proximity of the second and third poles of the expansion. Poles that are in close proximity cannot be reliably distinguished by the inversion algorithm. This highlights the importance of the numerical modeling, because inversions of measured coefficients may not always be accurate. Finally, the numerically-derived coefficients for a regular tetrahedron were compared to experimentally-measured coefficients. In this case, the numerically-derived coefficients showed better agreement with the experimental data because the poles were sufficiently distant.

CHAPTER 4

BODIES OF REVOLUTION

4.1 Introduction

In this chapter, a simple method will be described for computing pole-expansion coefficients of conductors with axial symmetry. The technique presented in this chapter is based on a simple circuit model [39]. Baum originally suggested using an eigendecomposition in conjunction with this method for a theoretical argument, but no computational work was done [6]. Only coefficients that correspond to axially-directed currents can be modeled in such a way. Nonetheless, because of symmetry, all of the pole-expansion coefficients of a spherical conductor can be modeled with this method. This method may be also used for targets where only axially-directed eddy currents are of interest. All of the significant pole-expansion coefficients of thick wire loop can be modeled in this way and also some of the pole-expansion coefficients of a cylindrical conductor.

4.2 Numerical Strategy

4.2.1 Circuit Impedance Model

The approach taken in this chapter is to first discretize the cross section of the body of revolution into a network of coupled loops. This is done by first obtaining a triangulation of the conducting region's cross section, where each triangular element is then rotated about the axis of revolution to create a cell. A cutout of a torus that has been discretized in such a manner is shown in Fig. 4.1. Each loop is assumed to support only an axially-directed current. Each current loop is also assumed to see an impedance, which is a function of both the loop resistance, the loop inductance, as well as the frequency. Finally, the flowing current and impedance give rise to a voltage drop over the loop.

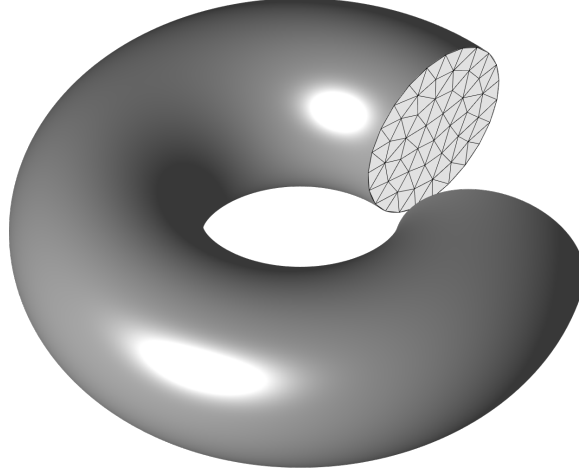


Figure 4.1: Cutout of a torus discretized into rotationally-symmetric elements with triangular cross section.

These assumptions lead to a simple impedance relation between the voltage drops over the loops, V , and the respective currents, I ,

$$V = (\mathbf{R} + j\omega\mathbf{L})I, \quad (4.1)$$

where ω is the angular frequency, \mathbf{R} is a diagonal matrix of loop resistances, and \mathbf{L} is a symmetric matrix of loop inductances. The diagonal entries of the positive-definite inductance matrix, \mathbf{L} , are the self inductances of each of the loops, and the off-diagonal entries contain the mutual inductances to other loops in the network.

Modeling the currents is simply a matter of finding sensible approximations for the voltages, loop resistances, and loop inductances. Simplest are the loop resistances, which are the diagonal entries of \mathbf{R} , and are equal to

$$\mathbf{R}_{jj} = \frac{l_j}{\sigma A_j}, \quad (4.2)$$

where l_j is the length of the loop, and A_j is the area of its triangular cross section. The self inductance of each current loop can be approximated from the formula for the self

inductance of a current loop with circular cross section,

$$\mathbf{L}_{jj} = b_k \mu_0 \left[\left(1 + \frac{1}{8} \left(\frac{a_j}{b_j} \right)^2 \right) \log \left(\frac{b_j}{8a_j} \right) + \frac{1}{24} \left(\frac{a_j}{b_j} \right)^2 + \frac{1}{4} \right], \quad (4.3)$$

where b_k is the radius of the loop, and a_k is the radius of the circular cross-section. This formula can be used to crudely approximate the self inductance of a current loop with triangular cross section by choosing an a_k that parametrizes a circular cross section of equal area to each cell's triangular cross section. The off-diagonal mutual inductance terms in the inductance matrix, \mathbf{L} , can be computed using the formula

$$\mathbf{L}_{ij} = \frac{2\mu_0 \sqrt{b_i b_j}}{k} \left[\left(1 - \frac{k^2}{2} \right) K(k^2) - E(k^2) \right], \quad (4.4)$$

where K and E are complete elliptic integrals of the first and second kind, respectively, and

$$k^2 = \frac{4b_i b_j}{(b_i + b_j)^2 + s^2}, \quad (4.5)$$

where s is the vertical separation between current loops.

4.2.2 Generalized Eigenvalue Problem

Like the strategy in previous chapters, the pole-expansion coefficients can be obtained by solving a generalized eigenvalue problem,

$$\mathbf{L}\mathbf{v} = \lambda \mathbf{R}\mathbf{v}, \quad (4.6)$$

where \mathbf{v} is the eigenvector, and λ is the corresponding eigenvalue. The eigenvalues and eigenvectors can be joined together in matrix form to also satisfy

$$\mathbf{L}\mathbf{V} = \mathbf{R}\mathbf{V}\mathbf{\Lambda}, \quad (4.7)$$

where $\mathbf{V} = [\mathbf{v}_1, \mathbf{v}_2, \dots, \mathbf{v}_K]$ is the matrix of eigenvectors, and $\mathbf{\Lambda} = \text{diag}[\lambda_1, \lambda_2, \dots, \lambda_K]$ is the diagonal matrix of eigenvalues.

4.2.3 Pole Expansion Derivation

The generalized eigenvalues and eigenvectors of Eq. (4.6) can be used to expand Eq. (4.7) into pole-expansion form by first recognizing that

$$\mathbf{R} = \mathbf{R}\mathbf{V}\mathbf{V}^T\mathbf{R} \quad (4.8)$$

$$\mathbf{L} = \mathbf{R}\mathbf{V}\mathbf{\Lambda}\mathbf{V}^T\mathbf{R}, \quad (4.9)$$

which derives from the \mathbf{R} -orthogonality of the eigenvectors, $\mathbf{V}^T\mathbf{R}\mathbf{V} = \mathbf{I}$. The impedance can then be written as

$$\mathbf{R} + j\omega\mathbf{L} = \mathbf{R}\mathbf{V}(\mathbf{I} + j\omega\mathbf{\Lambda})\mathbf{V}^T\mathbf{R}. \quad (4.10)$$

If Eq. (4.10) is multiplied on the left by \mathbf{V}^T and on the right by \mathbf{V} , then

$$\mathbf{V}^T(\mathbf{R} + j\omega\mathbf{L})\mathbf{V} = (\mathbf{I} + j\omega\mathbf{\Lambda}). \quad (4.11)$$

Taking the inverse of the pencil, provided that ω does not coincide with a pole, results in

$$\begin{aligned} (\mathbf{V}^T(\mathbf{R} + j\omega\mathbf{L})\mathbf{V})^{-1} &= (\mathbf{I} + j\omega\mathbf{\Lambda})^{-1} \\ \mathbf{V}^{-1}(\mathbf{R} + j\omega\mathbf{L})^{-1}\mathbf{V}^{-T} &= (\mathbf{I} + j\omega\mathbf{\Lambda})^{-1} \\ (\mathbf{R} + j\omega\mathbf{L})^{-1} &= \mathbf{V}(\mathbf{I} + j\omega\mathbf{\Lambda})^{-1}\mathbf{V}^T, \end{aligned} \quad (4.12)$$

which can be written in summation form as

$$(\mathbf{R} + j\omega\mathbf{L})^{-1} = \sum_{k=1}^K (1 + j\omega\lambda_k)^{-1} \mathbf{v}_k \mathbf{v}_k^T. \quad (4.13)$$

Eq. (4.13) implies the following relation between loop voltages and loop currents:

$$I = \sum_{k=1}^K (1 + j\omega\lambda_k)^{-1} \mathbf{v}_k \mathbf{v}_k^T V. \quad (4.14)$$

If an assumption is made, that the voltage drop across each current loop is entirely due to a uniform time-varying magnetic field with magnitude $\|\mathbf{H}_o\|$, then the voltage excitation is given by

$$V = -j\omega \left\| \vec{\mathbf{H}}_o \right\| A, \quad (4.15)$$

where A is the area of the circle circumscribed by each current loop. Substituting this expression into Eq. (4.13) gives an expression for the z -directed magnetic moment,

$$\mathbf{m}_z = A \cdot I = - \sum_{k=1}^K \frac{j\omega/\zeta_k}{1 + j\omega/\zeta_k} \mu_0 A^T \mathbf{v}_k \mathbf{v}_k^T A \zeta_k \left\| \vec{\mathbf{H}}_o \right\| = - \sum_{k=1}^K \frac{j\omega/\zeta_k}{1 + j\omega/\zeta_k} c_k \left\| \vec{\mathbf{H}}_o \right\|, \quad (4.16)$$

where $\zeta_k = 1/\lambda_k$, and $\mathbf{M}_k|_{zz} = \mu_0 A^T \mathbf{v}_k \mathbf{v}_k^T A / \lambda_k$. Finally, the zz -component of the magnetic polarizability tensor is given by

$$\mathbf{M}(\omega)|_{zz} = - \sum_{k=1}^K \frac{j\omega/\zeta_k}{1 + j\omega/\zeta_k} \mathbf{M}_k|_{zz}, \quad (4.17)$$

because of the relationship between the magnetic moment and the magnetic polarizability,

$$\vec{\mathbf{m}} = \mathbf{M} \cdot \vec{\mathbf{H}}. \quad (4.18)$$

4.3 Results

4.3.1 Spherical Conductor

The pole-expansion coefficients for a spherical conductor have been computed analytically in the past [6]. Numerical results could, therefore, be compared to their known analytic values. The numerical analysis also provides the current modes that give rise to these

coefficients. Plots of the first six current modes that have a non-vanishing dipole moment are shown in Fig. 4.2. The first mode has a current that circulates around the sphere, and higher-order modes show a more complex current distribution. The plots demonstrate the intuition that the number of sign reversals in the current throughout the cross section increases with increasing mode number. The convergence behavior of the method is shown in Fig. 4.3, where the error in each of the expansion coefficients is plotted as a function of the mesh grain.

4.3.2 Thick Wire Loops

This method can also be applied to thick wire loops, where the radius of the wire, a , is significant relative to the radius of the loop, b . The first set of pole-expansion coefficients for a thick wire loop can be predicted by ignoring the thickness of the loop and then following the analysis for filament loops that is given in [6]. As the wire loop increases in thickness, additional poles are needed to characterize the response. A depiction of these modes is shown in Fig. 4.4 for a relatively thick wire loop with $a/b = 0.5$. The relative amplitude of the tensor coefficients is a function of the wire thickness; therefore, the ordering of the modes is different for loops of varying aspect ratios.

The significance of the secondary modes can be understood from Fig 4.5, where the pole-expansion coefficients are graphed as a function of aspect ratio, a/b . The pole-expansion coefficients in this graph are normalized by their analytical values for a filament loop, ζ_S and M_S . Experimental data is also plotted for wire loops with thicknesses ranging from 32 AWG to 10 AWG and circumferences ranging from 50 mm to 200 mm. The analytical formula agrees with both the numerically-computed coefficients and the inversions of measured data. As the thickness of the wire grows, so does the significance of the secondary poles. Because of their small relative amplitude, however, the secondary poles are difficult to invert from measured data. In Fig. 4.6, the same coefficients are graphed, but this time they are normalized so that they can be scaled using Eq. (1.4) and Eq. (1.5).

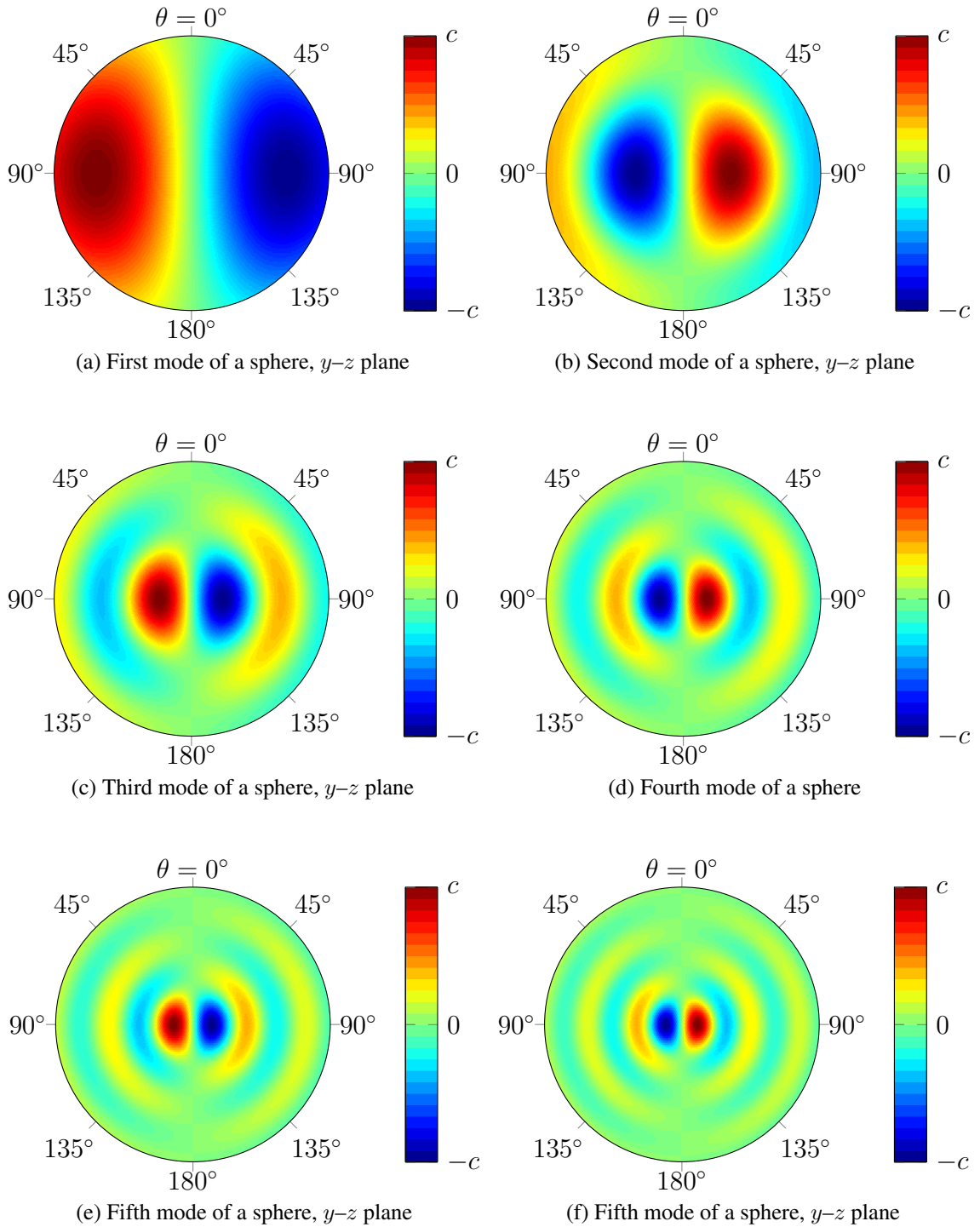
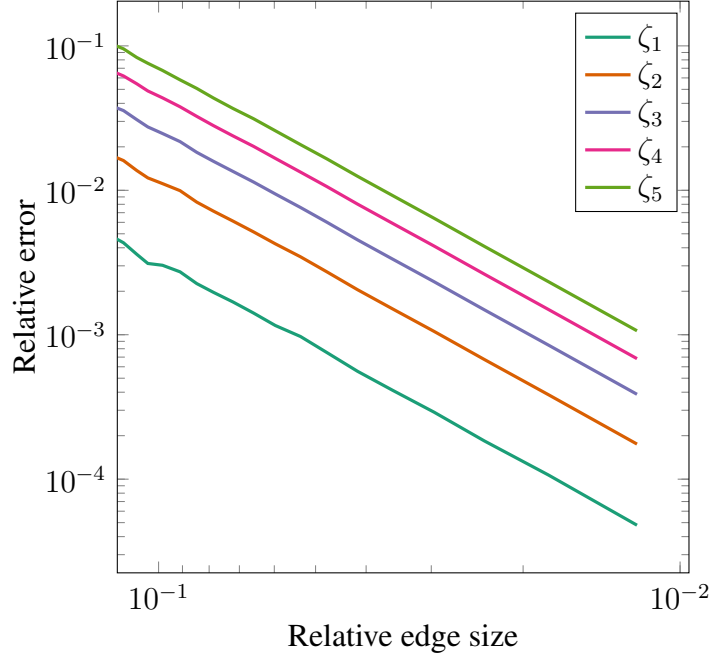
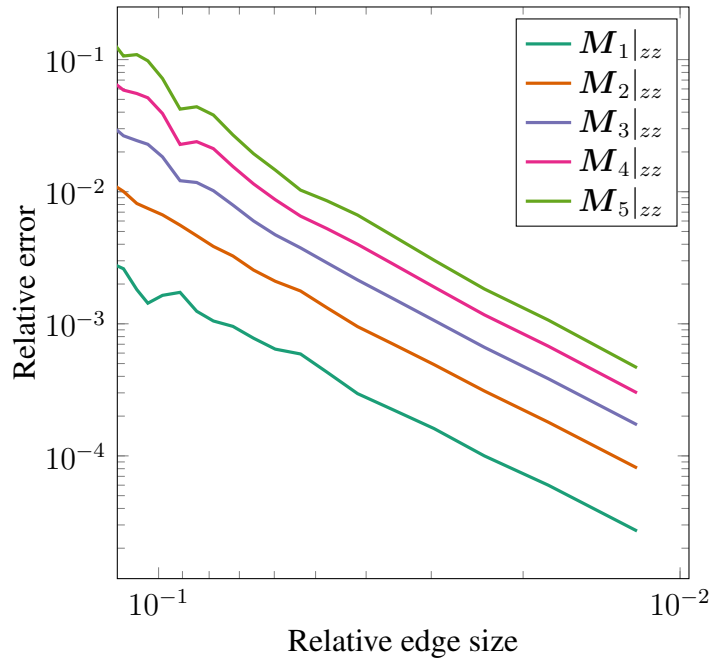


Figure 4.2: Slices of the eddy-current modes in the y - z plane of a non-permeable conducting sphere. The cross section of the current-density flow is plotted, with blue and red marking currents that flow into the page and out of the page respectively.



(a) Convergence plot for relaxation frequencies



(b) Convergence plot for diagonal tensor coefficients

Figure 4.3: Convergence plot for the pole-expansion coefficients of the MPT of a spherical conductor. The relative error in the pole-expansion coefficients is plotted against the mesh's average relative edge length.

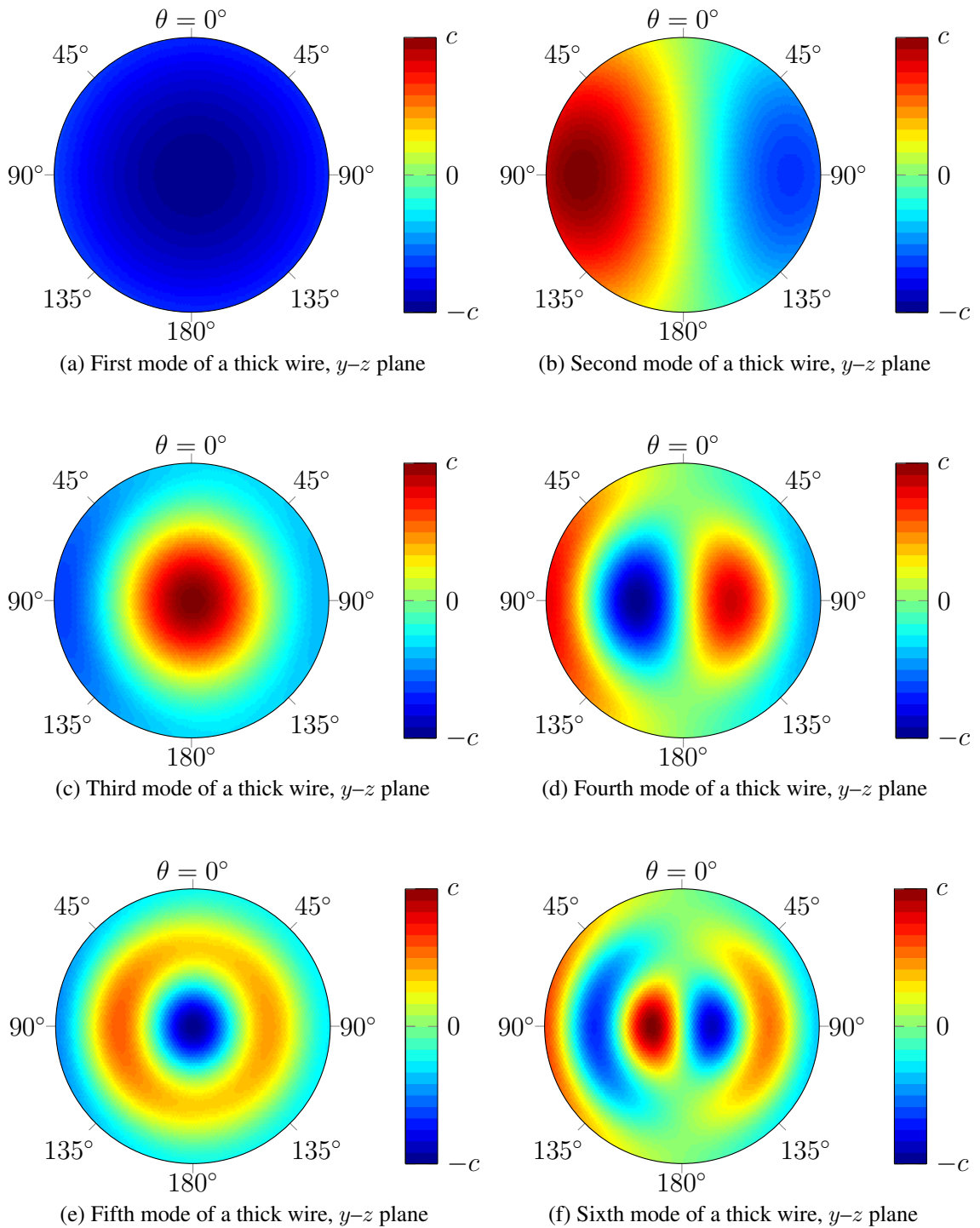
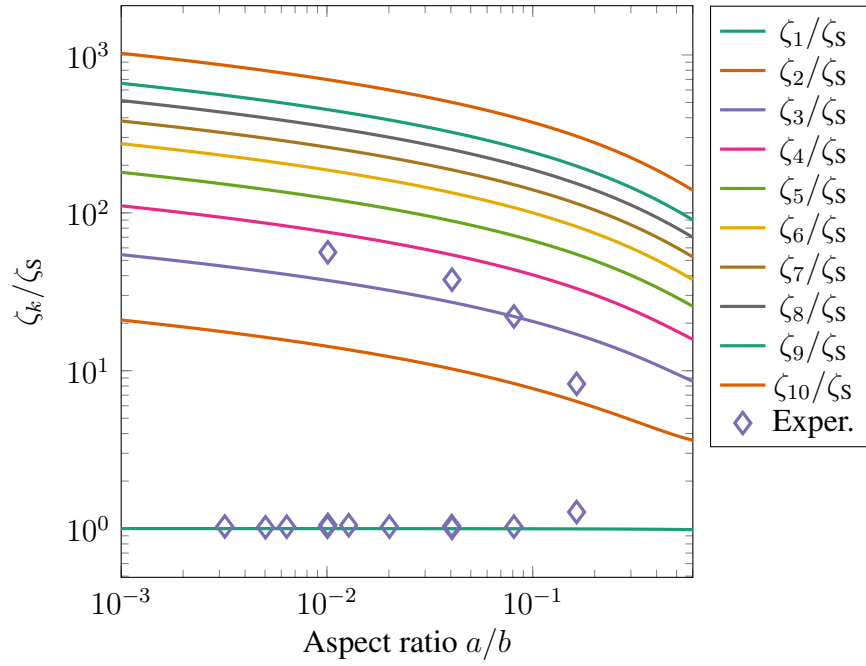
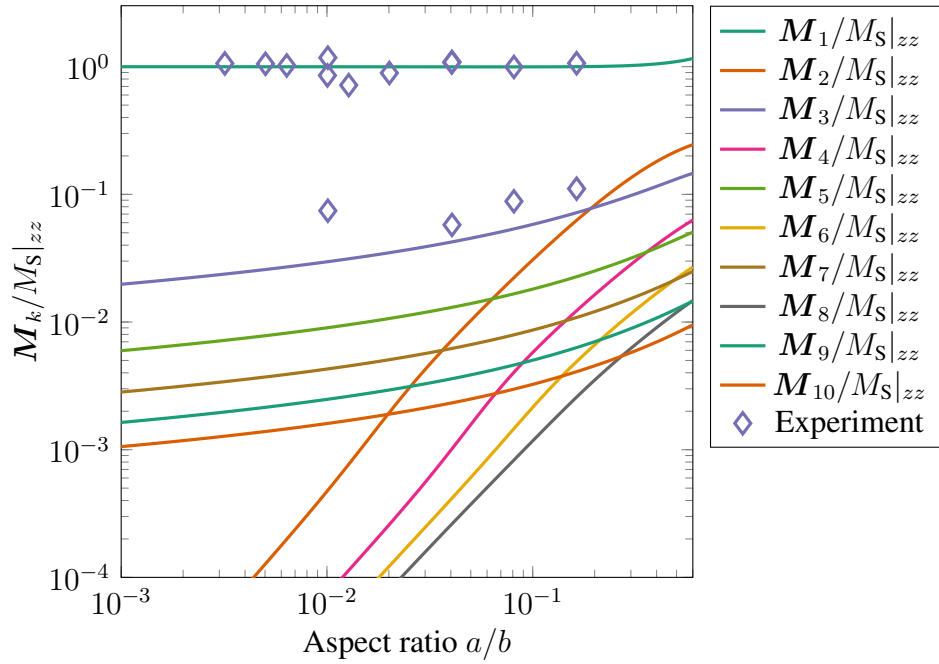


Figure 4.4: Slices of the eddy-current modes of a thick wire loop with $a/b = 0.5$. The cross section of the current-density flow in the y - z plane is plotted, with blue and red marking currents that flow into the page and out of the page respectively.

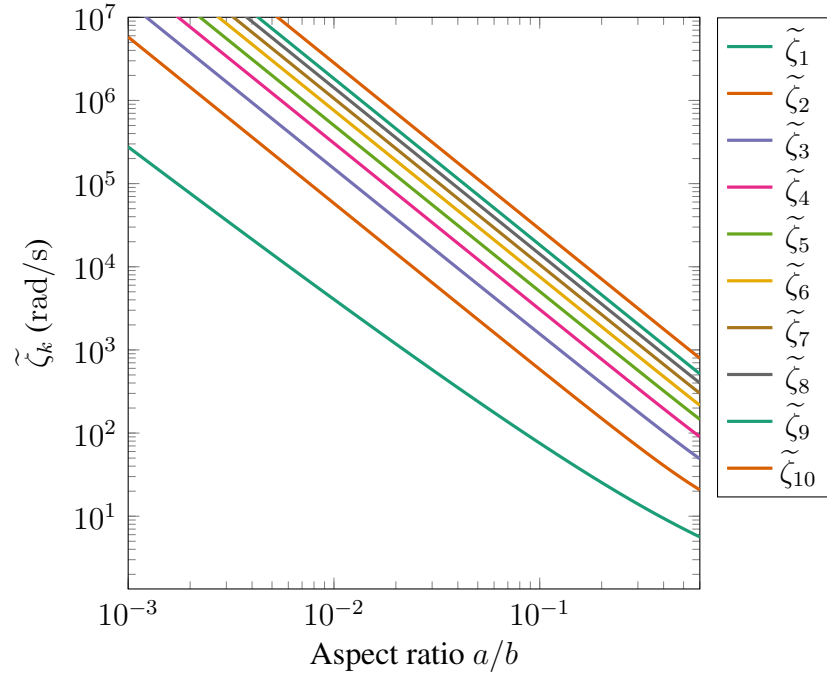


(a) Relaxation frequencies

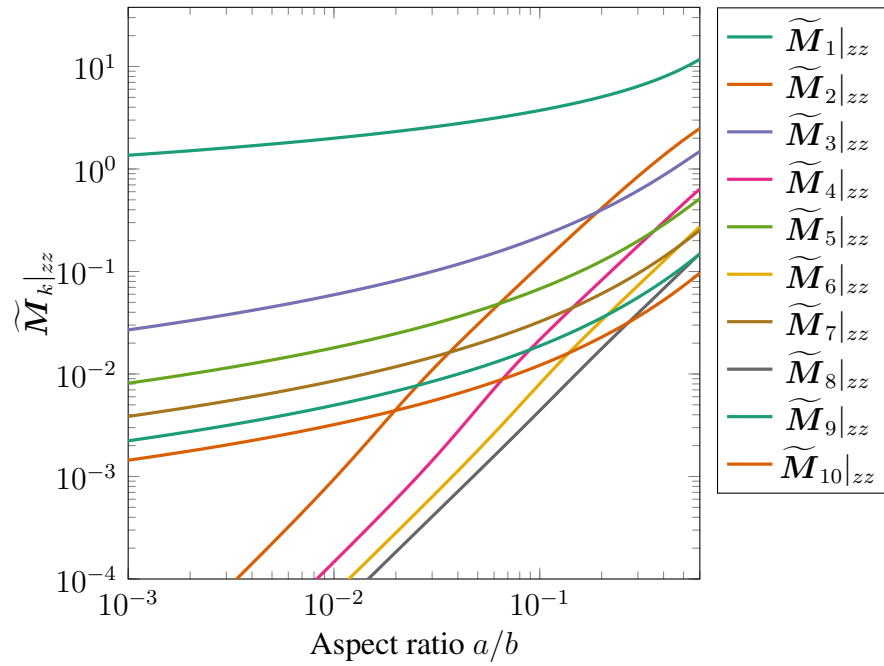


(b) Magnetic polarizability coefficients

Figure 4.5: Pole-expansion coefficients of a thick wire loop that are divided by their analytical values for a thin wire loop, and then graphed against their aspect ratio a/b . Experimental data validates the thin-wire approximation but also demonstrates the significance of higher-order modes.



(a) Relaxation frequencies



(b) Magnetic polarizability coefficients

Figure 4.6: Normalized pole-expansion coefficients of a thick wire loop are graphed against their aspect ratio a/b . The radii of the wire loops have been normalized to 1 so that the coefficients can be easily scaled.

4.4 Conclusion

A simple method was presented for computing a subset of the pole-expansion coefficients of rotationally symmetric targets. The method can only compute coefficients that correspond to axially-directed currents, which makes it less general than the work in [17, 5]. The method is only approximate but still exhibits fast convergence. This was illustrated by comparing numerical results to the analytically-derived coefficients for a sphere. Mode graphs were given for a sphere and a thick wire loop, illustrating the current flow that is associated with each of their respective first six poles. Finally, numerically-computed, analytical, and measured pole-expansion coefficients were compared for loops of varying aspect ratios.

Part II

Differential Methods

CHAPTER 5

CONDUCTING SOLIDS

5.1 Introduction

In this chapter, a number of approaches will be presented for computing the pole-expansion coefficients of the MPT of three-dimensional targets using a differential method. To date, pole-expansion coefficients have not been computed for targets with arbitrary geometries, as previous characterizations of the pole-expansion coefficients of three-dimensional targets has been limited to targets with axial symmetry [4, 5]. Closed-form expressions have only been derived for spheres [6], and oblate and prolate spheroids [33]. Modeling general targets is important, because many targets of interest do not have rotational symmetry or are too thick to be accurately modeled by the approach in Chapter 2.

The methods outlined in this chapter, which are all based on the finite integration technique, apply to targets with arbitrary geometries. The analysis is complicated by the fact that the linear systems computed using differential methods have a large null space, the presence of which makes it difficult to compute the linear system's smallest eigenvalues. In contrast to the integral approach in Chapter 3, removing the null space is not possible, because it destroys the sparsity of the linear system. In this chapter, a number of techniques are explored for computing the eigenvalues of such linear systems. Computational results are given for a sphere, and a cube, and are compared to experimental data.

5.2 The Finite Integration Technique

The finite integration technique (FIT) [40] is a spatial discretization scheme, based on Yee's Grid [41], which utilizes staggered grids, a primary grid and a dual grid, to solve Maxwell's equations. In the notation of the finite integration technique, the time-harmonic form of

Maxwell's equation under a quasi-magnetostatic assumption state that

$$\begin{aligned}
\nabla \times \vec{H}(\vec{r}) &= \vec{J}(\vec{r}) & \tilde{C}\widehat{h} &= \widehat{j} \\
\nabla \times \vec{E}(\vec{r}) &= -j\omega\vec{B}(\vec{r}) & C\widehat{e} &= -j\omega\widehat{b} \\
\nabla \cdot \vec{B}(\vec{r}) &= 0 & \tilde{S}\widehat{b} &= 0 \\
\nabla \cdot \vec{J}(\vec{r}) &= 0 & \tilde{S}\widehat{j} &= 0,
\end{aligned} \tag{5.1}$$

where \widehat{e} is the electric field, \widehat{h} is the magnetic field intensity, \widehat{b} is the magnetic flux density, \widehat{j} is the current density, C is the curl operator on the primary grid, \tilde{C} is the curl operator on the dual grid, S is the divergence operator on the primary grid, and \tilde{S} is the divergence operator on the dual grid. \widehat{e} and \widehat{b} are unknowns on the primary grid, while \widehat{h} and \widehat{j} are unknowns on the dual grid. \widehat{e} is associated with traces on the primary grid, while \widehat{h} is associated with traces on the dual grid. Similarly, \widehat{b} is associated with fluxes through the faces of the primary grid, while \widehat{j} is associated with fluxes through the faces of the dual grid. A depiction of the Yee grid and the unknowns corresponding to each grid are illustrated in Fig. 5.1. The constitutive relations,

$$\begin{aligned}
\vec{H}(\vec{r}) &= \nu\vec{B}(\vec{r}) & \widehat{h} &= M_\nu\widehat{b} \\
\vec{J}(\vec{r}) &= \sigma\vec{E}(\vec{r}), & \widehat{j} &= M_\sigma\widehat{e},
\end{aligned} \tag{5.2}$$

map unknowns between primary and dual grids through the mass matrices for reluctivity, M_ν , and conductivity, M_σ . This association of unknowns with each of the grids can be understood from Alain Bossavit's "Maxwell's House" [9, 42] in Fig. 5.2, which illustrates the relation between Maxwell's equations, the electromagnetic unknowns, and the constitutive relations.

In FIT, the discrete gradient, curl, and divergence matrices, which are G , C , and S respectively, contain topological information on the incidence relations of simplexes on the primary grid. Their analogues, \tilde{G} , \tilde{C} , and \tilde{S} , contain the topological information on the

incidence relations of dual simplexes.

The differential operators on the primary and dual grid have several important properties. First, the curl primary curl matrix, C , is equal to the transpose of the curl on the dual matrix, \tilde{C} , meaning that

$$C = \tilde{C}^T. \quad (5.3)$$

Second, the two vector calculus identities

$$\text{div curl} = 0 \quad (5.4)$$

$$\text{curl grad} = \mathbf{0} \quad (5.5)$$

have discrete analogues

$$\begin{aligned} SC = 0 & \quad \text{and} \quad \tilde{S}\tilde{C} = 0 \\ CG = 0 & \quad \tilde{C}\tilde{G} = 0, \end{aligned} \quad (5.6)$$

where G and \tilde{G} are the discrete gradient on the primary grid and dual grid respectively. Substituting Eq. (5.3) into the Eq. (5.6) implies that

$$G = \tilde{S}^T \quad (5.7)$$

$$S = \tilde{G}^T. \quad (5.8)$$

5.3 A Curl-Curl Equation

The electric field's curl-curl equation is a consolidated form that can be derived from a quasi-magnetostatic approximation of Maxwell's equations. Beginning with Faraday's law, and multiplying on the left by M_ν gives

$$M_\nu C \hat{e} = -j\omega M_\nu \hat{b} = -j\omega \hat{h}, \quad (5.9)$$

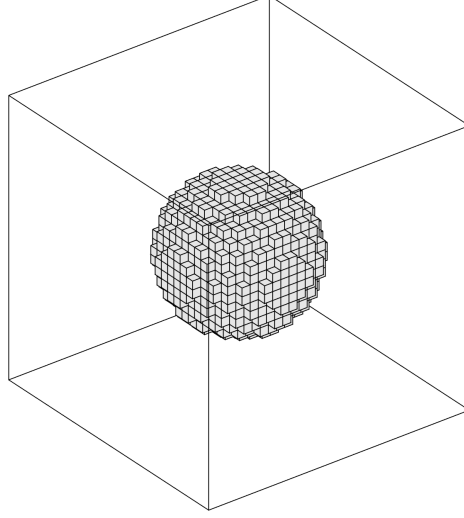


Figure 5.3: Illustration of a discretized highly-conductive sphere embedded in a low conductivity region. Only the primary cells in the conducting region are shown, illustrating FIT's characteristic cubical grid.

which utilized the constitutive relation $\widehat{\mathbf{h}} = \mathbf{M}_\nu \widehat{\mathbf{b}}$. Next, multiplying on the left by $\widetilde{\mathbf{C}}$ gives

$$\widetilde{\mathbf{C}} \mathbf{M}_\nu \mathbf{C} \widehat{\mathbf{e}} = -j\omega \widetilde{\mathbf{C}} \widehat{\mathbf{h}}, \quad (5.10)$$

which by Ampere's law also equals

$$\widetilde{\mathbf{C}} \mathbf{M}_\nu \mathbf{C} \widehat{\mathbf{e}} = -j\omega \widehat{\mathbf{j}}. \quad (5.11)$$

Substituting the final constitutive relation, $\widehat{\mathbf{j}} = \mathbf{M}_\sigma \widehat{\mathbf{e}}$, gives the curl-curl equation in the electric field,

$$\widetilde{\mathbf{C}} \mathbf{M}_\nu \mathbf{C} \widehat{\mathbf{e}} = -j\omega \mathbf{M}_\sigma \widehat{\mathbf{e}}. \quad (5.12)$$

The curl-curl equation can be broken into incident and scattered components,

$$\widetilde{\mathbf{C}} \mathbf{M}_\nu \mathbf{C} \widehat{\mathbf{e}}^{\text{inc}} + \widetilde{\mathbf{C}} \mathbf{M}_\nu \mathbf{C} \widehat{\mathbf{e}}^{\text{sca}} = -j\omega \mathbf{M}_\sigma \widehat{\mathbf{e}}^{\text{inc}} - j\omega \mathbf{M}_\sigma \widehat{\mathbf{e}}^{\text{sca}}, \quad (5.13)$$

which simplifies to

$$\tilde{\mathbf{C}}\mathbf{M}_\nu\mathbf{C}\widehat{\mathbf{e}}^{\text{sca}} + j\omega\mathbf{M}_\sigma\widehat{\mathbf{e}}^{\text{sca}} = -j\omega\mathbf{M}_\sigma\widehat{\mathbf{e}}^{\text{inc}}, \quad (5.14)$$

when it is assumed that the excitation field satisfies $\tilde{\mathbf{C}}\mathbf{M}_\nu\mathbf{C}\widehat{\mathbf{e}}^{\text{inc}} = 0$. This equation can be inverted for $\widehat{\mathbf{e}}^{\text{sca}}$ by solving a symmetric eigenvalue problem,

$$\mathbf{C}^T\mathbf{M}_\nu\mathbf{C}\mathbf{v} = \lambda\mathbf{M}_\sigma\mathbf{v}, \quad (5.15)$$

where $\tilde{\mathbf{C}} = \mathbf{C}^T$ was substituted, \mathbf{v} is an eigenvector, and λ is its corresponding eigenvalue.

This eigenvalue problem has a number of properties of note. Because of the identity $\mathbf{C}\mathbf{G} = \mathbf{0}$, the curl-curl matrix has a large null space, which makes up approximately one-third of its eigenvalue spectrum. The curl-curl matrix is a product of sparse matrices; it is, therefore, also sparse, with approximately 13 nonzero entries per row. The mass matrix \mathbf{M}_σ is diagonal but highly ill-conditioned, since it expresses the conductivity contrast between a highly-conductive target and the soil, which has low conductivity. This type of computational domain is illustrated in Fig. 5.3, where a highly-conducting sphere is embedded in a region with low conductivity. Only the highly-conductive cells are drawn, but a large computational domain outside of the conductor is necessary so that fields are not abruptly truncated. The curl-curl equation is, therefore, a sparse and symmetric matrix equation with a large null space in the matrix $\mathbf{C}^T\mathbf{M}_\nu\mathbf{C}$.

5.4 The Sparse Generalized Eigenvalue Problem

In the following section we will discuss methods for solving generalized eigenvalue problems of the form

$$\mathbf{A}\mathbf{v} = \lambda\mathbf{B}\mathbf{v}, \quad (5.16)$$

where we will adopt the convention of naming $\mathbf{A} = \mathbf{C}^T \mathbf{M}_\nu \mathbf{C}$, the stiffness matrix, and $\mathbf{B} = \mathbf{M}_\sigma$, the mass matrix. The solution to this eigenvalue problem is non-trivial because of the properties of the system matrices and the eigenpairs that are of interest. The large null space of the curl-curl matrix, \mathbf{A} , makes it such that the eigenpairs of interest, which are the smallest non-zero eigenvalues, and are deep in the interior of the eigenvalue spectrum. Moreover, \mathbf{B} is ill-conditioned, and the curl-curl matrix is sparse, meaning that any factorization would require large amounts of storage, since the sparsity would be lost. The interior spectrum is comprised of a small subset of eigenvectors with a non-zero dipole moment, which are of interest, and many more eigenvectors that do not have a dipole moment and are not needed. These undesired modes must be computed anyhow. As a result, it is necessary to compute roughly 500 total eigenpairs in order to find 5 eigenvalues with a non-zero dipole moment. In the following subsections, we will discuss strategies for approaching this eigenvalue problem.

5.4.1 The Lanczos Algorithm

The Implicitly Restarted Lanczos algorithm, which is implemented in ARPACK [36], is a common algorithm choice for solving a sparse, symmetric generalized eigenvalue problem, when only a few of the system's eigenpairs are desired. Through the reverse communication interface, the user is queried by ARPACK for specific vector interactions with the system matrices, avoiding the need to communicate the system matrices themselves to the eigenvalue routine. This allows ARPACK to solve eigenvalue problems where it is impractical to compute the system matrices explicitly.

Shift-and-Invert Strategy

A shift-and-invert strategy is often the preferred approach for computing interior eigenvalues of a symmetric generalized eigenvalue problem. In ARPACK, a shift-and-invert strategy

requires solutions to a linear system of the form $(\mathbf{A} - \sigma\mathbf{B})\mathbf{w} = \mathbf{z}$, where σ is the shift¹, as well as matrix-vector products of the form $\mathbf{z} = \mathbf{B}\mathbf{w}$. The shift, σ , is chosen near the eigenvalues of interest, and ARPACK will find a set number of eigenpairs with eigenvalues that are nearest to the shift. When the matrix \mathbf{B} is highly ill-conditioned, or singular, as is the case in this section, the solver can take steps to *purify* the basis vectors and rid them of contributions from infinite or near-infinite eigenvectors.

Unfortunately, a shift-and-invert strategy is not viable for computing the desired eigenpairs of these matrices because of two main drawbacks. First, the strategy computes eigenvectors that have an eigenvalue that is nearest to σ ; as such, it requires a reasonable initial guess, which is not always available. Choosing a shift that is too low will return many eigenvectors that have an eigenvalue of zero, and choosing a shift that is too high will cause ARPACK to miss some of the eigenpairs of interest. Second, precise solutions to the ill-conditioned linear system are required so that the algorithm remains numerically stable; for that reason, the inverse problem, $(\mathbf{A} - \sigma\mathbf{B})\mathbf{w} = \mathbf{z}$, practically demands a potentially indefinite factorization of $\mathbf{A} - \sigma\mathbf{B}$. Because of the size of the system matrices and the fact that the factorization of these matrices destroys their sparsity, the storage requirements are vastly increased, making large problems unfeasible.

5.4.2 The FEAST Algorithm

The FEAST algorithm is a Rayleigh-Ritz-based algorithm for computing all of the eigenvalues and eigenvectors of Hermitian or non-Hermitian eigenvalue problems within a region of the complex plane [43]. The algorithm utilizes contour integration and a density matrix to accurately solve only for the eigenpairs of interest. Like in ARPACK, FEAST utilizes a reverse communication interface that allows for custom handling of the solutions to linear systems, that are required at each iteration step. While not competitive in performance compared to other eigenvalue solvers, at least for this application, the unique spectral fil-

¹Here σ denotes the shift, not the electrical conductivity.

tering strategy provides a reliable method for finding all the eigenvalues within a region of the complex plane. This is difficult to guarantee using other solvers.

5.4.3 The Jacobi-Davidson Iteration

The Jacobi-Davidson iteration is an attractive alternative to the Lanczos and FEAST algorithm for computing interior eigenvalues when a factorization is not feasible [44, 45]. Where other solvers require precise solutions to a linear inverse problem, the Jacobi-Davidson iteration only requires an approximate solution to its correction equation. Solutions to the correction equation can be computed using a less precise iterative method instead of the direct method, which is practically demanded by ARPACK. In order to understand the Jacobi-Davidson iteration, its best to understand it in the context of the its two spiritual predecessors: the Jacobi Orthogonal components correction (JOCC) and the Davidson iteration. In this section, we will consider only the standard eigenvalue problem of a matrix \mathbf{A} ,

$$\mathbf{A}\mathbf{v} = \lambda\mathbf{v}, \quad (5.17)$$

although the ideas are trivially extendable to the generalized eigenvalue problem.

Jacobi's Orthogonal Component Correction

The Jacobi orthogonal component correction is a method for computing the approximate eigenvalues of symmetric matrices. If \mathbf{A} is a symmetric and diagonally dominant matrix, with α being its diagonal element with the largest magnitude, then the symmetric eigenvalue problem can be written in matrix notation as

$$\mathbf{A} \begin{bmatrix} 1 \\ \mathbf{z} \end{bmatrix} = \begin{bmatrix} \alpha & \mathbf{b}^T \\ \mathbf{b} & \mathbf{F} \end{bmatrix} \begin{bmatrix} 1 \\ \mathbf{z} \end{bmatrix} = \lambda \begin{bmatrix} 1 \\ \mathbf{z} \end{bmatrix}, \quad (5.18)$$

where \mathbf{F} is a square matrix, and \mathbf{b} and \mathbf{z} are vectors. The eigenvalue problem is equivalent, then, to two dependent equations,

$$\lambda = \alpha + \mathbf{b}^T \mathbf{z} \quad (5.19)$$

$$(\mathbf{F} - \lambda \mathbf{I}) \mathbf{z} = -\mathbf{b}. \quad (5.20)$$

Jacobi suggested solving the linear system iteratively,

$$\theta_k = \alpha + \mathbf{b}^T \mathbf{z}_k \quad (5.21)$$

$$(\mathbf{D}_F - \theta_k \mathbf{I}) \mathbf{z}_{k+1} = (\mathbf{D}_F - \mathbf{F}) \mathbf{z}_k - \mathbf{b}, \quad (5.22)$$

where \mathbf{D}_F is the diagonal of the matrix \mathbf{F} , and where the initial guesses are $\theta_1 = \alpha$ and $\mathbf{z}_1 = \mathbf{0}$. Interpreting this iterative strategy, it is apparent that α is the initial approximation of the system's largest eigenvalue and $\mathbf{e}_1 = \begin{bmatrix} 1 & 0 & \dots & 0 \end{bmatrix}^T$ is the corresponding approximate eigenvector. At each iteration step, corrections to the eigenvector are searched for in the space orthogonal to the initial approximate eigenvector, \mathbf{e}_1 . To maintain its simplicity, the algorithm completely ignores the availability of better approximations to the eigenvector, $\mathbf{u}_k = [1 \quad \mathbf{z}^T]^T$. Jacobi understood this limitation and pre-processed \mathbf{A} to make it even more diagonally dominant, making \mathbf{e}_1 an even better approximation for the largest eigenvector. This viewpoint is useful, because it helps to understand the Davidson iteration as an accelerated version of JOCC.

Davidson Iteration

The Davidson iteration is an algorithm that is effective at calculating the eigenpairs of diagonally dominant matrices. The algorithm works by the principle of subspace expansion. If a subspace is given, $\mathbf{V} = \text{span}\{\mathbf{v}_1, \mathbf{v}_2, \dots, \mathbf{v}_k\}$, in which the matrix has a Ritz vector, \mathbf{u}_k , with a corresponding Ritz value, θ_k , then at each iteration step Davidson suggested

expanding the search space using a vector, \mathbf{t}_k , with

$$(\mathbf{D}_A - \theta_k \mathbf{I})\mathbf{t}_k = -\mathbf{r}_k, \quad (5.23)$$

and where $\mathbf{r}_k = \mathbf{A}\mathbf{u}_k - \lambda\mathbf{u}_k$ is the residual. The vector, \mathbf{t}_k , that satisfies the linear system is orthogonalized with respect to the previous search subspace, \mathbf{V} , and then is subsequently added to the search subspace (only the component of \mathbf{t}_k orthogonal to \mathbf{u}_k remains). The iteration is repeated until convergence, as the norm of the residual reaches some tolerance, ϵ . Examining Eq. (5.23), and substituting the expression for the residual, it becomes apparent that for this method not to stagnate, the matrix \mathbf{A} must not be exactly diagonal, because then $\mathbf{z} = \mathbf{u}_k$, and the search space is not expanded.

In order to understand the Davidson iteration's relation to JOCC, it is helpful to give \mathbf{A} the structure in Eq. (5.18) and to scale \mathbf{u}_k such that $\mathbf{u}_k = \begin{bmatrix} 1 & \mathbf{z}^T \end{bmatrix}^T$. Then, the residual vector takes the form

$$\mathbf{r}_k = \mathbf{A}\mathbf{u}_k - \theta_k\mathbf{u}_k = \begin{bmatrix} \alpha + \mathbf{b}^T \mathbf{z}_k - \theta_k \\ (\mathbf{F} - \theta_k \mathbf{I})\mathbf{z}_k + \mathbf{b} \end{bmatrix}. \quad (5.24)$$

If \mathbf{y}_k is chosen to be the component of \mathbf{t}_k orthogonal to \mathbf{e}_1 , then

$$(\mathbf{D}_F - \theta_k \mathbf{I})\mathbf{y}_k = -(\mathbf{F} - \theta_k \mathbf{I})\mathbf{z}_k - \mathbf{b} = (\mathbf{D}_F - \mathbf{F})\mathbf{z}_k - (\mathbf{D}_F - \theta_k \mathbf{I})\mathbf{z}_k - \mathbf{b}, \quad (5.25)$$

and therefore,

$$(\mathbf{D}_F - \theta_k \mathbf{I})(\mathbf{z}_k + \mathbf{y}_k) = (\mathbf{D}_F - \mathbf{F})\mathbf{z}_k - \mathbf{b}. \quad (5.26)$$

From Eq. (5.26), it can be recognized that for a given \mathbf{z}_k and θ_k , Eq. (5.26) is equal to Eq. (5.22) when $\mathbf{z}_{k+1} = \mathbf{z}_k + \mathbf{y}_k$. The methods are different, because JOCC computes its next approximate eigenpair using only the previous approximation and the original approximation, \mathbf{e}_1 , whereas the Davidson iteration computes a new Ritz vector using the

entire expanded search subspace. In that sense, the Davidson iteration can be viewed as an accelerated version of JOCC [44].

From JOCC and Davidson to Jacobi-Davidson

The Jacobi-Davidson iteration borrows ideas both from Jacobi orthogonal component correction and from the Davidson iteration. It borrows from JOCC the idea of searching for corrections in the space orthogonal to the eigenvector approximation. This is different from the Davidson iteration, where the component in the direction of the Ritz vector is removed only during the orthogonalization step. It borrows from the Davidson iteration the idea of exploiting the entire subspace that was constructed up to that point in the search for the next Ritz pair. Both methods, in their own way, attempt to find a correction vector that is orthogonal to the current eigenvector approximation.

The Jacobi-Davidson iteration is inspired by this idea of searching for a correction in the subspace orthogonal to the current Ritz vector. Let $\tilde{\mathbf{A}}$ be the orthogonal projection of the matrix, \mathbf{A} , onto the subspace orthogonal to \mathbf{u}_k ,

$$\tilde{\mathbf{A}} = (\mathbf{I} - \mathbf{u}_k \mathbf{u}_k^T) \mathbf{A} (\mathbf{I} - \mathbf{u}_k \mathbf{u}_k^T), \quad (5.27)$$

where it was assumed that $\|\mathbf{u}_k\|_2 = 1$. Then from Eq. (5.27) it follows that

$$\mathbf{A} = \tilde{\mathbf{A}} + \mathbf{A} \mathbf{u}_k \mathbf{u}_k^T + \mathbf{u}_k \mathbf{u}_k^T \mathbf{A} - \theta_k \mathbf{u}_k \mathbf{u}_k^T, \quad (5.28)$$

where the property $\mathbf{u}_k^T \mathbf{A} \mathbf{u}_k = \theta_k$ was substituted into the expansion's last term.

We would like to find a correction, \mathbf{v} , orthogonal to the current Ritz vector, \mathbf{u}_k , which together satisfy Eq. (5.17),

$$\mathbf{A}(\mathbf{u}_k + \mathbf{v}) = \lambda(\mathbf{u}_k + \mathbf{v}) \quad \mathbf{v} \perp \mathbf{u}_k. \quad (5.29)$$

Substituting Eq. (5.28) into Eq. (5.29) gives

$$\begin{aligned} (\tilde{\mathbf{A}} + \mathbf{A}\mathbf{u}_k\mathbf{u}_k^T + \mathbf{u}_k\mathbf{u}_k^T\mathbf{A} - \theta_k\mathbf{u}_k\mathbf{u}_k^T)(\mathbf{u}_k + \mathbf{v}) &= \lambda(\mathbf{u}_k + \mathbf{v}) \\ \tilde{\mathbf{A}}\mathbf{u}_k + \tilde{\mathbf{A}}\mathbf{v} + \mathbf{A}\mathbf{u}_k + \theta_k\mathbf{u}_k + (\mathbf{u}_k^T\mathbf{A}\mathbf{v})\mathbf{u}_k - \theta_k\mathbf{u}_k &= \lambda(\mathbf{u}_k + \mathbf{v}), \end{aligned}$$

and refactoring gives

$$\begin{aligned} (\tilde{\mathbf{A}} - \lambda\mathbf{I})\mathbf{v} &= -\mathbf{A}\mathbf{u}_k + \theta_k\mathbf{u}_k + \lambda\mathbf{u}_k - \theta_k\mathbf{u}_k - (\mathbf{u}_k^T\mathbf{A}\mathbf{v})\mathbf{u}_k \\ (\tilde{\mathbf{A}} - \lambda\mathbf{I})\mathbf{v} &= -\mathbf{r}_k + (\lambda - \theta_k - \mathbf{u}_k^T\mathbf{A}\mathbf{v})\mathbf{u}_k. \end{aligned} \quad (5.30)$$

The rightmost term of Eq. (5.30) must be zero because the remaining terms in the equation are all orthogonal to \mathbf{u}_k . Therefore,

$$(\tilde{\mathbf{A}} - \lambda\mathbf{I})\mathbf{v} = -\mathbf{r}_k. \quad (5.31)$$

Since the actual eigenvalue is unknown, Jacobi-Davidson uses the current Ritz value instead, giving

$$(\tilde{\mathbf{A}} - \theta_k\mathbf{I})\mathbf{v} = -\mathbf{r}_k. \quad (5.32)$$

Eq. (5.32) leads to the final form of the Jacobi-Davidson correction equation,

$$(\mathbf{I} - \mathbf{u}_k\mathbf{u}_k^T)(\mathbf{A} - \theta_k\mathbf{I})(\mathbf{I} - \mathbf{u}_k\mathbf{u}_k^T)\mathbf{t} = -\mathbf{r}_k \quad \mathbf{t} \perp \mathbf{u}_k, \quad (5.33)$$

which exploits the orthogonality between \mathbf{t} , \mathbf{u}_k , and \mathbf{r}_k . The Jacobi-Davidson iteration for the generalized eigenvalue problem is given in Alg. 1, where the iteration for a standard eigenvalue problem is given by substituting $\mathbf{B} = \mathbf{I}$.

Algorithm 1 The Jacobi-Davidson iteration for the generalized eigenvalue problem.

```

1: function JACOBI-DAVIDSON( $\mathbf{A}$ ,  $\mathbf{B}$ ,  $\epsilon$ ,  $i_{\max}$ )
2:    $\mathbf{E}_0 \leftarrow [ ]$ ,  $\Lambda_0 \leftarrow \emptyset$ 
3:   for  $i \leftarrow 1, 2, \dots, i_{\max}$  do
4:     Initialize  $\mathbf{v}_1 \leftarrow \mathbf{v}_1 / \|\mathbf{v}_1\|$  such that  $\mathbf{v}_1 \perp \mathbf{E}_{i-1}$ 
5:      $\mathbf{V}_1 \leftarrow [\mathbf{E}_{i-1}, \mathbf{v}_1]$ 
6:     Compute  $\mathbf{W}_1 = \mathbf{V}_1^T \mathbf{A} \mathbf{V}_1$ 
7:     for  $k \leftarrow 1, 2, \dots$  do
8:       Compute the eigenpairs  $(\theta, \mathbf{s})$  of  $\mathbf{W}_k$  ( $\mathbf{W}_k \mathbf{s} = \theta \mathbf{I} \mathbf{s}$ )
9:       Select  $(\theta_k, \mathbf{s}_k)$  with  $\theta_k$  nearest to the target ( $\theta_k \notin \Lambda_{i-1}$ ) and with  $\|\mathbf{s}_k\| = 1$ .
10:      Compute  $\mathbf{u}_k = \mathbf{V}_k \mathbf{s}_k$  and  $\mathbf{r}_k = (\mathbf{A} - \theta_k \mathbf{B}) \mathbf{u}_k$ .
11:      if  $\|\mathbf{r}_k\| < \epsilon$  then
12:        Set  $\lambda_i = \theta_k$  and  $\mathbf{e}_i = \mathbf{u}_k$ 
13:        Update  $\mathbf{E}_i = [\mathbf{E}_{i-1}, \mathbf{e}_i]$  and  $\Lambda_i = \Lambda_{i-1} \cup \{\lambda_i\}$ 
14:        exit  $k$ 
15:      else
16:        Solve (approximately)
17:         $(\mathbf{I} - \mathbf{B} \mathbf{u}_k \mathbf{u}_k^T)(\mathbf{A} - \theta_k \mathbf{B})(\mathbf{I} - \mathbf{u}_k \mathbf{u}_k^T \mathbf{B}) \mathbf{t} = -\mathbf{r}_k$     $\mathbf{t} \perp_{\mathbf{B}} \mathbf{u}_k$ 
18:         $\mathbf{B}$ -orthonormalize  $\mathbf{t}$  against  $\mathbf{V}_k$ ,  $\mathbf{v}_{k+1} \leftarrow \frac{\mathbf{t} - \sum_{l=1}^k (\mathbf{v}_l^T \mathbf{B} \mathbf{t}) \mathbf{v}_l}{\|\mathbf{t} - \sum_{l=1}^k (\mathbf{v}_l^T \mathbf{B} \mathbf{t}) \mathbf{v}_l\|_{\mathbf{B}}}$ 
19:        Expand the search space,  $\mathbf{V}_{k+1} = [\mathbf{V}_k, \mathbf{v}_{k+1}]$ 
20:        Let  $\mathbf{W}_{k+1} = \begin{bmatrix} \mathbf{W}_k & \mathbf{V}_k^T \mathbf{A} \mathbf{v}_{k+1} \\ \mathbf{v}_{k+1}^T \mathbf{A} \mathbf{V}_k & \mathbf{v}_{k+1}^T \mathbf{A} \mathbf{v}_{k+1} \end{bmatrix}$ 
21:      end if
22:    end for
23:  end for
24:  Return  $\mathbf{E}_i, \Lambda_i$ 
25: end function

```

5.5 Null Space Avoidance Techniques

As mentioned previously, finding the smallest eigenvalues of the curl-curl equation is difficult because of the large size of its null space. Approximately one-third of the eigenvalues of the linear system are zero eigenvalues. As such, it is not practical to compute and store them, and they must be avoided in some way in order to reach the interior of the eigenvalue spectrum, where the eigenpairs of interest lie. In the following section, a number of strategies will be discussed for null space avoidance. The first two strategies can be implemented generally, in any eigenvalue solver, while the remaining two are specific to the Jacobi-Davidson iteration.

5.5.1 Ritz Value Filtering

Ritz value filtering is the idea of choosing to refine only those Ritz vectors with Ritz values that lie within some region of the complex plane. This simple idea can be implemented in many different ways. ARPACK implements a type of filtering to eliminate infinite or near-infinite eigenvalues [36]. In SLEPC, a general package which implements many interchangeable eigenvalue solvers, including Jacobi-Davidson and Lanczos, it is possible to specify a region in the complex plane, so that the solver only refines Ritz pairs in that region [46]. Geus implemented an aggressive adaptive filter in JDSYM, a Jacobi-Davidson implementation, which cuts off the search region, so that Ritz pairs are refined only if they have a Ritz value greater than a certain threshold, τ , or that have a Ritz value that is greater than the last converged eigenvalue [47].

In the Jacobi-Davidson iteration, Ritz value filtering has mixed performance when used as a means to avoid the curl-curl equation's null space. Its main advantage is the simplicity of its implementation, requiring only a rough guess of the system's first non-zero eigenvalue, so that Ritz pairs below that guess can be safely filtered out. Regardless of the implementation, filtering has a disadvantage that the correction vector used to expand

the search space has no guarantee of being orthogonal to the system's null space. This means that the search space may not be significantly expanded in each iteration, resulting in slow convergence. For the eigenvalue problems in this chapter, we found that the aggressive filtering in `JDSYM` often misses clustered eigenvalues, because eigenpairs are not found necessarily in monotonic order, and the filter's cutoff moves too aggressively. Clustered eigenpairs are not uncommon in electromagnetics problems, and eigenvalues often have multiplicity due to target symmetries. An argument could be made that if the target has symmetry, it should be exploited when formulating the electromagnetic model, which would eliminate these redundant eigenpairs. While this argument has merit, exploiting symmetry does not entirely solve the problem. It is conceivable, however, that a less aggressive filter would be less likely to miss eigenpairs.

5.5.2 Tree-Cotree Filtering

As was mentioned previously, the null space of the curl-curl matrix is a consequence of the presence of inessential degrees of freedom in the curl operator. A straightforward approach for removing this null space is to simply eliminate these redundant degrees of freedom from the equation. This conveniently reduces the number of degrees of freedom in the curl-curl matrix, and hence, the size of the generalized eigenvalue problem.

The curl matrix is a rectangular matrix with a number of columns equal to the number of edges in the grid, $\mathcal{N}(\mathcal{E})$, and a number of rows equal to the number of faces, $\mathcal{N}(\mathcal{F})$. The number of inessential degrees of freedom is equal to the number of nodes in the mesh $\mathcal{N}(\mathcal{N})$, leaving $\mathcal{N}(\mathcal{E}) - \mathcal{N}(\mathcal{N})$ essential degrees of freedom. The inessential degrees of freedom correspond to gradients, which are node-associated, with $\mathcal{N}(\mathcal{N})$ degrees of freedom. Any gradient function is mapped to zero by the curl operator, and therefore has a vanishing norm with respect to the matrix \mathbf{A} . Two-thirds of the eigenvalue spectrum is comprised of the $\mathcal{N}(\mathcal{E}) - \mathcal{N}(\mathcal{N})$ essential degrees of freedom, while the $\mathcal{N}(\mathcal{N})$ remaining are inessential.

These essential and inessential degrees of freedom in the curl matrix are closely related to the tree-cotree decomposition of edges in the grid. A maximally-spanning tree, which is defined as a non-unique subset of edges, that travel through all the nodes in the grid without closing a cycle will always have $\mathcal{N}(\mathcal{N})$ members; a cotree, which is the subset of all remaining graph edges, will always have $\mathcal{N}(\mathcal{E}) - \mathcal{N}(\mathcal{N})$ members. For a regular grid, such as the Yee grid in this section, a tree-cotree decomposition of grid edges can be found trivially.

Given a tree-cotree decomposition, define the following partitions of matrices and unknowns:

$$\mathbf{C}' = \begin{bmatrix} \mathbf{C}_t & \mathbf{C}_c \end{bmatrix} \quad (5.34)$$

$$\mathbf{G}' = \begin{bmatrix} \mathbf{G}_t \\ \mathbf{G}_c \end{bmatrix} \quad (5.35)$$

$$\mathbf{M}'_{\sigma} = \begin{bmatrix} \mathbf{M}_{\sigma t} & \mathbf{0} \\ \mathbf{0} & \mathbf{M}_{\sigma c} \end{bmatrix} \quad (5.36)$$

$$\widehat{\mathbf{e}}' = \begin{bmatrix} \widehat{\mathbf{e}}_t \\ \widehat{\mathbf{e}}_c \end{bmatrix}. \quad (5.37)$$

Utilizing these partitions, and exploiting the assumption that the current density is solenoidal, gives

$$\mathbf{G}'^T \mathbf{M}'_{\sigma} \widehat{\mathbf{e}} = \mathbf{G}_t^T \mathbf{M}_{\sigma t} \widehat{\mathbf{e}}_t + \mathbf{G}_c^T \mathbf{M}_{\sigma c} \widehat{\mathbf{e}}_c = \mathbf{0}, \quad (5.38)$$

and therefore,

$$\widehat{\mathbf{e}}_t = \mathbf{F} \widehat{\mathbf{e}}_c, \quad \text{where } \mathbf{F} = -(\mathbf{G}_t^T \mathbf{M}_{\sigma t})^{-1} \mathbf{G}_c^T \mathbf{M}_{\sigma c}. \quad (5.39)$$

The partitioned electric field trace, $\widehat{\mathbf{e}}'$, can therefore be written as

$$\widehat{\mathbf{e}}' = \begin{bmatrix} \widehat{\mathbf{e}}_t \\ \widehat{\mathbf{e}}_c \end{bmatrix} = \begin{bmatrix} \mathbf{F} \\ \mathbf{I} \end{bmatrix} \widehat{\mathbf{e}}_t = \mathbf{L}_e \widehat{\mathbf{e}}_t. \quad (5.40)$$

Substituting the partitioned matrices and Eq. (5.40) into the curl-curl equation, Eq. (5.14), gives

$$\mathbf{L}_e^T \mathbf{C}'^T \mathbf{M}_\nu \mathbf{C}' \mathbf{L}_e \widehat{\mathbf{e}}_c^{\text{sca}} + j\omega \mathbf{L}_e^T \mathbf{M}'_\sigma \mathbf{L}_e \widehat{\mathbf{e}}_c^{\text{sca}} = -j\omega \mathbf{L}_e^T \mathbf{M}'_\sigma \mathbf{L}_e \widehat{\mathbf{e}}_c^{\text{inc}}, \quad (5.41)$$

which can be inverted by setting up a generalized eigenvalue problem.

The form in Eq. (5.41), however, has several disadvantages. First, the conditioning of this matrix equation is worse than Eq. (5.14) due to the extra multiplications by the ill-conditioned conductivity matrix, \mathbf{M}_σ , and its inverses. Eq. (5.39) uses the solenoidality of the current density to infer the electric field traces along tree edges using the traces along cotree edges. Given the conductivity contrast in \mathbf{M}_σ between the highly conducting target and the low-conductivity background, it is clear why these additional multiplications raise the condition number. Furthermore, different choices of tree and cotree will result in different matrix conditioning. The simplest tree-cotree decomposition to find, built off of the regularity of the grid, might worsen the conditioning of the system to a greater degree than an arbitrary tree-cotree decomposition. Second, the block matrix \mathbf{F} in Eq. (5.40) destroys the sparsity of the equation, greatly increasing the storage requirements and the cost of matrix multiplications. Still, for small problems, where the loss of sparsity is not an issue, this method can eliminate the null space effectively.

5.5.3 Simplified Augmented System

In his thesis [47], Geus also proposed using an augmented system, when solving the correction equation, to avoid the null space. In the notation of this thesis, the simplified aug-

mented linear system (SAUG) can be written as

$$\begin{bmatrix} \mathbf{A} - \sigma \mathbf{B} & \mathbf{M}_\sigma \mathbf{G} \\ \mathbf{G}^T \mathbf{M}_\sigma & \mathbf{0} \end{bmatrix} \begin{bmatrix} \mathbf{w} \\ \mathbf{w}' \end{bmatrix} = \begin{bmatrix} \mathbf{z} \\ \mathbf{0} \end{bmatrix}. \quad (5.42)$$

The augmented system maintains the symmetry of the original matrices while simultaneously constraining the divergence of \mathbf{w} to zero. This also corresponds to constraining the divergence of the current density to zero. In JDSYM, the SAUG method is not applied explicitly, but rather using a preconditioned Krylov method, where the preconditioner accelerates the convergence of the iterative solver while also being responsible for projecting vectors away from the nullspace. This preconditioned approach is also significantly more computationally efficient than augmenting the linear system. Because the linear system is not positive definite, however, stability is not guaranteed. Still, in practice, like Geus had found previously, we found that the method performed extremely well and exhibited fast convergence.

5.5.4 Null-Space-Free Jacobi-Davidson

Another approach to solving this curl-curl eigenvalue problem is through radical modifications to the Jacobi-Davidson iteration itself [48]. The idea is to represent the electric field unknowns in terms of magnetic field unknowns and to apply successive corrections, within the Jacobi-Davidson iteration, to the magnetic field rather than to the electric field. Through this process, the effect of the null space is muted. In the following subsection we will adopt the notation that

$$\hat{\mathbf{A}} = \mathbf{M}_\nu \mathbf{C} \mathbf{M}_\sigma^{-1} \mathbf{C}^T \mathbf{M}_\nu \quad \text{and} \quad \hat{\mathbf{B}} = \mathbf{M}_\nu. \quad (5.43)$$

Null-space-free Jacobi Davidson relies on a few properties of the system matrices. First,

it can be shown that if $\hat{\mathbf{u}}_k$ is a Ritz vector of $(\hat{\mathbf{A}}\hat{\mathbf{B}}^{-1}\hat{\mathbf{A}}, \hat{\mathbf{A}})$, then

$$\mathbf{u}_k = M_\sigma^{-1} \mathbf{C}^T M_\nu \hat{\mathbf{u}}_k \quad (5.44)$$

is a Ritz vector of (\mathbf{A}, \mathbf{B}) , which shares the same Ritz value. Choosing such a \mathbf{u}_k is advantageous, since it has no null space components. They share identical matrix norms, because

$$\begin{aligned} \hat{\mathbf{u}}_k^T \hat{\mathbf{A}} \hat{\mathbf{B}}^{-1} \hat{\mathbf{A}} \hat{\mathbf{u}}_k &= \hat{\mathbf{u}}_k^T M_\nu \mathbf{C} M_\sigma^{-1} \mathbf{C}^T M_\nu \mathbf{C} M_\sigma^{-1} \mathbf{C}^T M_\nu \hat{\mathbf{u}}_k \\ &= (\hat{\mathbf{u}}_k^T M_\nu \mathbf{C} M_\sigma^{-1}) \mathbf{C}^T M_\nu \mathbf{C} (M_\sigma^{-1} \mathbf{C}^T M_\nu \hat{\mathbf{u}}_k) \\ &= \mathbf{u}_k^T \mathbf{C}^T M_\nu \mathbf{C} \mathbf{u}_k \\ &= \mathbf{u}_k^T \mathbf{A} \mathbf{u}_k, \end{aligned}$$

and, similarly, because

$$\begin{aligned} \hat{\mathbf{u}}_k^T \hat{\mathbf{A}} \hat{\mathbf{u}}_k &= \hat{\mathbf{u}}_k^T M_\nu \mathbf{C} M_\sigma^{-1} \mathbf{C}^T M_\nu \hat{\mathbf{u}}_k \\ &= \hat{\mathbf{u}}_k^T M_\nu \mathbf{C} M_\sigma^{-1} M_\sigma M_\sigma^{-1} \mathbf{C}^T M_\nu \hat{\mathbf{u}}_k \\ &= (\hat{\mathbf{u}}_k^T M_\nu \mathbf{C} M_\sigma^{-1}) M_\sigma (M_\sigma^{-1} \mathbf{C}^T M_\nu \hat{\mathbf{u}}_k) \\ &= \mathbf{u}_k^T M_\sigma \mathbf{u}_k \\ &= \mathbf{u}_k^T \mathbf{B} \mathbf{u}_k. \end{aligned}$$

Now, consider the residual of a \mathbf{u}_k , which also satisfies Eq. (5.44),

$$\begin{aligned}
\mathbf{r}_k &= (\mathbf{A} - \theta_k \mathbf{B}) \mathbf{u}_k \\
&= (\mathbf{C}^T \mathbf{M}_\nu \mathbf{C} - \theta_k \mathbf{M}_\sigma) \mathbf{M}_\sigma^{-1} \mathbf{C}^T \mathbf{M}_\nu \hat{\mathbf{u}}_k \\
&= \mathbf{C}^T (\mathbf{M}_\nu \mathbf{C} \mathbf{M}_\sigma^{-1} \mathbf{C}^T \mathbf{M}_\nu - \theta_k \mathbf{M}_\nu) \hat{\mathbf{u}}_k \\
&= \mathbf{C}^T (\hat{\mathbf{A}} - \theta_k \hat{\mathbf{B}}) \hat{\mathbf{u}}_k \\
&= \mathbf{C}^T \hat{\mathbf{r}}_k.
\end{aligned}$$

Here $\hat{\mathbf{r}}_k$ is the residual for the pencil $(\hat{\mathbf{A}}, \hat{\mathbf{B}})$, which is isospectral to the pencil $(\hat{\mathbf{A}} \hat{\mathbf{B}}^{-1} \hat{\mathbf{A}}, \hat{\mathbf{A}})$.

Next, consider what happens when we evaluate the Jacobi-Davidson correction equation,

$$(\mathbf{I} - \mathbf{B} \mathbf{u}_k \mathbf{u}_k^T) (\mathbf{A} - \theta_k \mathbf{B}) (\mathbf{I} - \mathbf{u}_k \mathbf{u}_k^T \mathbf{B}) \mathbf{t} = -\mathbf{r}_k \quad \mathbf{t} \perp_{\mathbf{B}} \mathbf{u}_k, \quad (5.45)$$

for a correction vector, $\mathbf{t} = \mathbf{M}_\sigma^{-1} \mathbf{C}^T \mathbf{M}_\nu \hat{\mathbf{t}}$, and a Ritz vector that similarly satisfies Eq. (5.44).

The left-hand side of the correction equation simplifies to

$$\begin{aligned}
&(\mathbf{I} - \mathbf{B} \mathbf{u}_k \mathbf{u}_k^T) (\mathbf{A} - \theta_k \mathbf{B}) (\mathbf{I} - \mathbf{u}_k \mathbf{u}_k^T \mathbf{B}) \mathbf{t} \\
&= (\mathbf{I} - \mathbf{B} \mathbf{u}_k \mathbf{u}_k^T) (\mathbf{A} - \theta_k \mathbf{B}) (\mathbf{I} - \mathbf{M}_\sigma^{-1} \mathbf{C}^T \mathbf{M}_\nu \hat{\mathbf{u}}_k \hat{\mathbf{u}}_k^T \mathbf{M}_\nu \mathbf{C} \mathbf{M}_\sigma^{-1} \mathbf{M}_\sigma) \mathbf{M}_\sigma^{-1} \mathbf{C}^T \mathbf{M}_\nu \hat{\mathbf{t}} \\
&= (\mathbf{I} - \mathbf{B} \mathbf{u}_k \mathbf{u}_k^T) (\mathbf{A} - \theta_k \mathbf{B}) (\mathbf{M}_\sigma^{-1} \mathbf{C}^T \mathbf{M}_\nu - \mathbf{M}_\sigma^{-1} \mathbf{C}^T \mathbf{M}_\nu \hat{\mathbf{u}}_k \hat{\mathbf{u}}_k^T \mathbf{M}_\nu \mathbf{C} \mathbf{M}_\sigma^{-1} \mathbf{C}^T \mathbf{M}_\nu) \hat{\mathbf{t}} \\
&= (\mathbf{I} - \mathbf{B} \mathbf{u}_k \mathbf{u}_k^T) (\mathbf{A} - \theta_k \mathbf{B}) (\mathbf{M}_\sigma^{-1} \mathbf{C}^T \mathbf{M}_\nu - \mathbf{M}_\sigma^{-1} \mathbf{C}^T \mathbf{M}_\nu \hat{\mathbf{u}}_k \hat{\mathbf{u}}_k^T \hat{\mathbf{A}}) \hat{\mathbf{t}} \\
&= (\mathbf{I} - \mathbf{B} \mathbf{u}_k \mathbf{u}_k^T) (\mathbf{A} - \theta_k \mathbf{B}) \mathbf{M}_\sigma^{-1} \mathbf{C}^T \mathbf{M}_\nu (\mathbf{I} - \hat{\mathbf{u}}_k \hat{\mathbf{u}}_k^T \hat{\mathbf{A}}) \hat{\mathbf{t}} \\
&= (\mathbf{I} - \mathbf{B} \mathbf{u}_k \mathbf{u}_k^T) (\mathbf{C}^T \mathbf{M}_\nu \mathbf{C} - \theta_k \mathbf{M}_\sigma) \mathbf{M}_\sigma^{-1} \mathbf{C}^T \mathbf{M}_\nu (\mathbf{I} - \hat{\mathbf{u}}_k \hat{\mathbf{u}}_k^T \hat{\mathbf{A}}) \hat{\mathbf{t}} \\
&= (\mathbf{I} - \mathbf{B} \mathbf{u}_k \mathbf{u}_k^T) (\mathbf{C}^T \mathbf{M}_\nu \mathbf{C} \mathbf{M}_\sigma^{-1} \mathbf{C}^T \mathbf{M}_\nu - \theta_k \mathbf{C}^T \mathbf{M}_\nu) (\mathbf{I} - \hat{\mathbf{u}}_k \hat{\mathbf{u}}_k^T \hat{\mathbf{A}}) \hat{\mathbf{t}} \\
&= (\mathbf{I} - \mathbf{B} \mathbf{u}_k \mathbf{u}_k^T) (\mathbf{C}^T \hat{\mathbf{A}} - \theta_k \mathbf{C}^T \hat{\mathbf{B}}) (\mathbf{I} - \hat{\mathbf{u}}_k \hat{\mathbf{u}}_k^T \hat{\mathbf{A}}) \hat{\mathbf{t}} \\
&= (\mathbf{I} - \mathbf{B} \mathbf{u}_k \mathbf{u}_k^T) \mathbf{C}^T (\hat{\mathbf{A}} - \theta_k \hat{\mathbf{B}}) (\mathbf{I} - \hat{\mathbf{u}}_k \hat{\mathbf{u}}_k^T \hat{\mathbf{A}}) \hat{\mathbf{t}} \\
&= (\mathbf{I} - \mathbf{M}_\sigma \mathbf{M}_\sigma^{-1} \mathbf{C}^T \mathbf{M}_\nu \hat{\mathbf{u}}_k \hat{\mathbf{u}}_k^T \mathbf{M}_\nu \mathbf{C} \mathbf{M}_\sigma^{-1}) \mathbf{C}^T (\hat{\mathbf{A}} - \theta_k \hat{\mathbf{B}}) (\mathbf{I} - \hat{\mathbf{u}}_k \hat{\mathbf{u}}_k^T \hat{\mathbf{A}}) \hat{\mathbf{t}}
\end{aligned}$$

$$\begin{aligned}
&= (\mathbf{C}^T - \mathbf{C}^T \mathbf{M}_\nu \widehat{\mathbf{u}}_k \widehat{\mathbf{u}}_k^T \mathbf{M}_\nu \mathbf{C} \mathbf{M}_\sigma^{-1} \mathbf{C}^T) (\widehat{\mathbf{A}} - \theta_k \widehat{\mathbf{B}}) (\mathbf{I} - \widehat{\mathbf{u}}_k \widehat{\mathbf{u}}_k^T \widehat{\mathbf{A}}) \widehat{\mathbf{t}} \\
&= \mathbf{C}^T (\mathbf{I} - \widehat{\mathbf{B}} \widehat{\mathbf{u}}_k \widehat{\mathbf{u}}_k^T \widehat{\mathbf{A}} \widehat{\mathbf{B}}^{-1}) (\widehat{\mathbf{A}} - \theta_k \widehat{\mathbf{B}}) (\mathbf{I} - \widehat{\mathbf{u}}_k \widehat{\mathbf{u}}_k^T \widehat{\mathbf{A}}) \widehat{\mathbf{t}},
\end{aligned}$$

where both sides of the correction equation are multiplied by \mathbf{C}^T , since $-\mathbf{r}_k = \mathbf{C}^T \widehat{\mathbf{r}}_k$.

Next, the orthogonality constraint in the correction equation simplifies to

$$\begin{aligned}
\mathbf{u}_k \perp_{\mathbf{B}} \mathbf{t} &\implies \mathbf{u}_k^T \mathbf{B} \mathbf{t} = 0 \\
&\widehat{\mathbf{u}}_k^T \mathbf{M}_\nu \mathbf{C} \mathbf{M}_\sigma^{-1} \mathbf{M}_\sigma \mathbf{M}_\sigma^{-1} \mathbf{C}^T \mathbf{M}_\nu \widehat{\mathbf{t}} = 0 \\
&\widehat{\mathbf{u}}_k^T \mathbf{M}_\nu \mathbf{C} \mathbf{M}_\sigma^{-1} \mathbf{C}^T \mathbf{M}_\nu \widehat{\mathbf{t}} = 0 \\
\widehat{\mathbf{u}}_k \perp_{\widehat{\mathbf{A}}} \widehat{\mathbf{t}} &\iff \widehat{\mathbf{u}}_k^T \widehat{\mathbf{A}} \widehat{\mathbf{t}} = 0.
\end{aligned}$$

Since both sides of the correction are multiplied on the left by \mathbf{C}^T , the correction equation can be reduced to

$$(\mathbf{I} - \widehat{\mathbf{B}} \widehat{\mathbf{u}}_k \widehat{\mathbf{u}}_k^T \widehat{\mathbf{A}} \widehat{\mathbf{B}}^{-1}) (\widehat{\mathbf{A}} - \theta_k \widehat{\mathbf{B}}) (\mathbf{I} - \widehat{\mathbf{u}}_k \widehat{\mathbf{u}}_k^T \widehat{\mathbf{A}}) \widehat{\mathbf{t}} = -\widehat{\mathbf{r}}_k \quad \widehat{\mathbf{u}}_k \perp_{\widehat{\mathbf{A}}} \widehat{\mathbf{t}}. \quad (5.46)$$

Using all of these derivations it is possible to construct the null-space-free Jacobi-Davidson iteration (NFJD), which is given in Alg. 2. In NFJD, the subspace approximations are computed using the pencil $(\widehat{\mathbf{A}}, \widehat{\mathbf{B}})$ instead of (\mathbf{A}, \mathbf{B}) , and the search space is spanned by what are, in this case, magnetic field vectors, which are converted to electric field vectors by multiplying on the left by $\mathbf{M}_\sigma^{-1} \mathbf{C}^T \mathbf{M}_\nu$. Through this multiplication, the Ritz vectors are constrained to be orthogonal to the curl-curl matrix's null space. Since corrections are applied to the magnetic field, instead of the electric field, the search space expansion at each iteration step is also orthogonal to the null space of the curl-curl matrix. Additionally, because of the duality in Maxwell's equations, NFJD has a dual version, that utilizes electric-field unknowns instead of magnetic-field unknowns [48]. The Dual version of the algorithm is given in Alg. 3.

Even though the pencils (\mathbf{A}, \mathbf{B}) and $(\widehat{\mathbf{A}}, \widehat{\mathbf{B}})$ are isospectral, their subspace approximations are generally different, corresponding to the matrix pencils $(\widehat{\mathbf{V}}^T \widehat{\mathbf{A}} \widehat{\mathbf{B}}^{-1} \widehat{\mathbf{A}} \widehat{\mathbf{V}}, \widehat{\mathbf{V}}^T \widehat{\mathbf{A}} \widehat{\mathbf{V}})$ and $(\widehat{\mathbf{V}}^T \widehat{\mathbf{A}} \widehat{\mathbf{V}}, \widehat{\mathbf{V}}^T \widehat{\mathbf{B}} \widehat{\mathbf{V}})$ respectively. Similar to the matrix \mathbf{A} , the matrix $\widehat{\mathbf{A}}$ also has a large null space. Therefore, when a Ritz pair of the subspace approximation of $(\widehat{\mathbf{A}}, \widehat{\mathbf{B}})$ approaches the null space of $\widehat{\mathbf{A}}$, it can no longer be used to provide an approximate eigenpair for (\mathbf{A}, \mathbf{B}) . For this reason, like in the case when conventional Jacobi-Davidson is applied to eddy-current problems, the Ritz pairs must be filtered, so that Ritz pairs that are near the null space are not refined.

While this idea appears to theoretically solve the null-space problem, In practice, it performed poorly when applied to the FIT model in this chapter. Both primal and dual version of NFJD were implemented and applied to the eddy-current problem. Unfortunately, neither implementation converged quickly to the eigenpairs of interest. The cause of this slow convergence appeared to be the high conductivity contrast in \mathbf{M}_σ , since eigenvalue problems with smaller conductivity contrast ($\kappa(\mathbf{M}_\sigma) \approx 10^3$) converged quickly. It is not known whether the slow convergence was caused by an issue in our specific implementation of the algorithm, or by the sensitivity of NFJD to ill-conditioning in the system matrices.

5.6 Pole Expansion Derivation

Once the relevant eigenvalues and eigenvectors have been found, it is straightforward to derive the pole-expansion form. Let $\mathbf{A} = \mathbf{C}^T \mathbf{M}_\nu \mathbf{C}$ and $\mathbf{B} = \mathbf{M}_\sigma$, and consider the generalized eigenvalue problem of \mathbf{A} and \mathbf{B} ,

$$\mathbf{A}\mathbf{v} = \lambda\mathbf{B}\mathbf{v}, \quad (5.47)$$

or

$$\mathbf{A}\mathbf{V} = \mathbf{B}\mathbf{\Lambda}\mathbf{V}, \quad (5.48)$$

Algorithm 2 Null-space-free Jacobi-Davidson.

```

1: function NULL-SPACE-FREE JACOBI-DAVIDSON( $\widehat{\mathbf{A}}, \widehat{\mathbf{B}}, \mathbf{B}^{-1}\mathbf{C}^T\widehat{\mathbf{B}}, \epsilon, i_{\max}$ )
2:    $\widehat{\mathbf{E}}_0 \leftarrow [ ]$ ,  $\Lambda_0 \leftarrow \emptyset$ 
3:   for  $i \leftarrow 1, 2, \dots, i_{\max}$  do
4:     Initialize  $\widehat{\mathbf{v}}_1 \leftarrow \widehat{\mathbf{v}}_1 / \|\widehat{\mathbf{v}}_1\|_{\widehat{\mathbf{A}}}$  such that  $\widehat{\mathbf{v}}_1 \perp_{\widehat{\mathbf{A}}} \widehat{\mathbf{E}}_{i-1}$ 
5:      $\widehat{\mathbf{V}}_1 \leftarrow [\widehat{\mathbf{E}}_{i-1}, \widehat{\mathbf{v}}_1]$ 
6:     Compute  $\widehat{\mathbf{Z}}_1 = \widehat{\mathbf{V}}_1^T \widehat{\mathbf{B}} \widehat{\mathbf{V}}_1$ 
7:     for  $k \leftarrow 1, 2, \dots$  do
8:       Compute the eigenpairs  $(\theta, \mathbf{s})$  of  $(\mathbf{I} - \theta \widehat{\mathbf{Z}}_k) \mathbf{s} = \mathbf{0}$ 
9:       Select  $(\theta_k, \mathbf{s}_k)$  with  $\theta_k$  nearest to the target ( $\theta_k \notin \Lambda_{i-1}$ ) and with  $\|\mathbf{s}_k\| = 1$ .
10:      Compute  $\widehat{\mathbf{u}}_k = \widehat{\mathbf{V}}_k \mathbf{s}_k$  and  $\widehat{\mathbf{r}}_k = (\widehat{\mathbf{A}} - \theta_k \widehat{\mathbf{B}}) \widehat{\mathbf{u}}_k$ .
11:      if  $\|\widehat{\mathbf{r}}_k\| < \epsilon$  then
12:        Set  $\lambda_i = \theta_k$  and  $\mathbf{e}_i = \mathbf{B}^{-1} \mathbf{C}^T \widehat{\mathbf{B}} \widehat{\mathbf{u}}_k$ 
13:        Update  $\widehat{\mathbf{E}}_i = [\widehat{\mathbf{E}}_{i-1}, \widehat{\mathbf{u}}_k]$  and  $\Lambda_i = \Lambda_{i-1} \cup \{\lambda_i\}$ 
14:        exit  $k$ 
15:      else
16:        Solve (approximately)
17:           $(\mathbf{I} - \widehat{\mathbf{B}} \mathbf{u}_k \mathbf{u}_k^T \widehat{\mathbf{A}} \widehat{\mathbf{B}}^{-1})(\widehat{\mathbf{A}} - \theta_k \widehat{\mathbf{B}})(\mathbf{I} - \mathbf{u}_k \mathbf{u}_k^T \widehat{\mathbf{A}}) \widehat{\mathbf{t}} = -\widehat{\mathbf{r}}_k \quad \widehat{\mathbf{t}} \perp_{\widehat{\mathbf{A}}} \widehat{\mathbf{u}}_k$ 
18:           $\widehat{\mathbf{A}}$ -orthonomalize  $\widehat{\mathbf{t}}$  against  $\widehat{\mathbf{V}}_k$ ,  $\widehat{\mathbf{v}}_{k+1} \leftarrow \frac{\widehat{\mathbf{t}} - \sum_{l=1}^k (\widehat{\mathbf{v}}_l^T \widehat{\mathbf{A}} \widehat{\mathbf{t}}) \widehat{\mathbf{v}}_l}{\|\widehat{\mathbf{t}} - \sum_{l=1}^k (\widehat{\mathbf{v}}_l^T \widehat{\mathbf{A}} \widehat{\mathbf{t}}) \widehat{\mathbf{v}}_l\|_{\widehat{\mathbf{A}}}}$ 
19:          Expand the search space,  $\widehat{\mathbf{V}}_{k+1} = [\widehat{\mathbf{V}}_k, \widehat{\mathbf{v}}_{k+1}]$ 
20:          Let  $\widehat{\mathbf{Z}}_{k+1} = \begin{bmatrix} \widehat{\mathbf{Z}}_k & \widehat{\mathbf{V}}_k^T \widehat{\mathbf{B}} \widehat{\mathbf{v}}_{k+1} \\ \widehat{\mathbf{v}}_{k+1}^T \widehat{\mathbf{B}} \widehat{\mathbf{V}}_k & \widehat{\mathbf{v}}_{k+1}^T \widehat{\mathbf{B}} \widehat{\mathbf{v}}_{k+1} \end{bmatrix}$ 
21:        end if
22:      end for
23:    end for
24:    Return  $\mathbf{E}_i = \mathbf{B}^{-1} \mathbf{C}^T \widehat{\mathbf{B}} \widehat{\mathbf{E}}_i$ ,  $\Lambda_i$ 
25: end function

```

where each \mathbf{v} is an eigenvector, λ is the corresponding eigenvalue, $\mathbf{V} = [\mathbf{v}_1, \mathbf{v}_2, \dots, \mathbf{v}_K]$ is the matrix of eigenvectors, and $\Lambda = \text{diag}[\lambda_1, \lambda_2, \dots, \lambda_K]$ is the diagonal matrix of eigenvalues. The generalized eigenvalues and eigenvectors of Eq. (5.15) can be used to expand Eq. (5.14) into pole-expansion form by first recognizing that

$$\mathbf{B} = \mathbf{B} \mathbf{V} \mathbf{V}^T \mathbf{B} \quad (5.49)$$

$$\mathbf{A} = \mathbf{B} \mathbf{V} \Lambda \mathbf{V}^T \mathbf{B}, \quad (5.50)$$

Algorithm 3 Null-space-free Jacobi-Davidson - Dual Version.

```

1: function NULL-SPACE-FREE JACOBI-DAVIDSON - DUAL VERSION( $\mathbf{A}$ ,  $\mathbf{B}$ ,  $\epsilon$ ,  $i_{\max}$ )
2:    $\mathbf{E}_0 \leftarrow [ ]$ ,  $\Lambda_0 \leftarrow \emptyset$ 
3:   for  $i \leftarrow 1, 2, \dots, i_{\max}$  do
4:     Initialize  $\mathbf{v}_1 \leftarrow \mathbf{v}_1 / \|\mathbf{v}_1\|_{\mathbf{A}}$  such that  $\mathbf{v}_1 \perp_{\mathbf{A}} \mathbf{E}_{i-1}$ 
5:      $\mathbf{V}_1 \leftarrow [\mathbf{E}_{i-1}, \mathbf{v}_1]$ 
6:     Compute  $\mathbf{Z}_1 = \mathbf{V}_1^T \mathbf{B} \mathbf{V}_1$ 
7:     for  $k \leftarrow 1, 2, \dots$  do
8:       Compute the eigenpairs  $(\theta, \mathbf{s})$  of  $(\mathbf{I} - \theta \mathbf{Z}_k) \mathbf{s} = \mathbf{0}$ 
9:       Select  $(\theta_k, \mathbf{s}_k)$  with  $\theta_k$  nearest to the target ( $\theta_k \notin \Lambda_{i-1}$ ) and with  $\|\mathbf{s}_k\| = 1$ .
10:      Compute  $\mathbf{u}_k = \mathbf{V}_k \mathbf{s}_k / \|\mathbf{V}_k \mathbf{s}_k\|_{\mathbf{B}}$  and  $\mathbf{r}_k = (\mathbf{A} - \theta_k \mathbf{B}) \mathbf{u}_k$ .
11:      if  $\|\mathbf{r}_k\| < \epsilon$  then
12:        Set  $\lambda_i = \theta_k$  and  $\mathbf{e}_i = \mathbf{u}_k$ 
13:        Update  $\mathbf{E}_i = [\mathbf{E}_{i-1}, \mathbf{e}_i]$  and  $\Lambda_i = \Lambda_{i-1} \cup \{\lambda_i\}$ 
14:        exit  $k$ 
15:      else
16:        Solve (approximately)
17:           $(\mathbf{I} - \mathbf{B} \mathbf{u}_k \mathbf{u}_k^T \mathbf{A} \mathbf{B}^{-1})(\mathbf{A} - \theta_k \mathbf{B})(\mathbf{I} - \mathbf{u}_k \mathbf{u}_k^T \mathbf{A}) \mathbf{t} = -\mathbf{r}_k$     $\mathbf{t} \perp_{\mathbf{A}} \mathbf{u}_k$ 
18:         $\mathbf{A}$ -orthonormalize  $\mathbf{t}$  against  $\mathbf{V}_k$ ,  $\mathbf{v}_{k+1} \leftarrow \frac{\mathbf{t} - \sum_{l=1}^k (\mathbf{v}_l^T \mathbf{A} \mathbf{t}) \mathbf{v}_l}{\|\mathbf{t} - \sum_{l=1}^k (\mathbf{v}_l^T \mathbf{A} \mathbf{t}) \mathbf{v}_l\|_{\mathbf{A}}}$ 
19:        Expand the search space,  $\mathbf{V}_{k+1} = [\mathbf{V}_k, \mathbf{v}_{k+1}]$ 
20:        Let  $\mathbf{Z}_{k+1} = \begin{bmatrix} \mathbf{Z}_k & \mathbf{V}_k^T \mathbf{B} \mathbf{v}_{k+1} \\ \mathbf{v}_{k+1}^T \mathbf{B} \mathbf{V}_k & \mathbf{v}_{k+1}^T \mathbf{B} \mathbf{v}_{k+1} \end{bmatrix}$ 
21:      end if
22:    end for
23:  end for
24:  Return  $\mathbf{E}_i, \Lambda_i$ 
25: end function

```

which derives from the \mathbf{B} -orthogonality of the eigenvectors, $\mathbf{V}^T \mathbf{B} \mathbf{V} = \mathbf{I}$. The pencil can then be written as

$$\mathbf{A} + j\omega \mathbf{B} = \mathbf{B} \mathbf{V} (\mathbf{I} + j\omega \Lambda) \mathbf{V}^T \mathbf{B}. \quad (5.51)$$

If Eq. (5.51) is multiplied on the left by \mathbf{V}^T and on the right by \mathbf{V} , then

$$\mathbf{V}^T (\mathbf{A} + j\omega \mathbf{B}) \mathbf{V} = (\Lambda + j\omega \mathbf{I}). \quad (5.52)$$

Taking the inverse of the pencil, provided that ω does not coincide with a pole, results in

$$\begin{aligned} (\mathbf{V}^T(\mathbf{A} + j\omega\mathbf{B})\mathbf{V})^{-1} &= (\mathbf{\Lambda} + j\omega\mathbf{I})^{-1} \\ \mathbf{V}^{-1}(\mathbf{A} + j\omega\mathbf{B})^{-1}(\mathbf{V}^T)^{-1} &= (\mathbf{\Lambda} + j\omega\mathbf{I})^{-1} \\ (\mathbf{A} + j\omega\mathbf{B})^{-1} &= \mathbf{V}(\mathbf{\Lambda} + j\omega\mathbf{I})^{-1}\mathbf{V}^T, \end{aligned} \quad (5.53)$$

which can be written in summation form as

$$(\mathbf{A} + j\omega\mathbf{B})^{-1} = \sum_{k=1}^K (\lambda_k + j\omega)^{-1} \mathbf{v}_k \mathbf{v}_k^T. \quad (5.54)$$

Using Eq. (5.54), it is possible to solve for the scattered electric field traces in Eq. (5.14),

$$\widehat{\mathbf{e}}^{\text{sca}} = - \sum_{k=1}^K \frac{j\omega}{\lambda_k + j\omega} \mathbf{v}_k \mathbf{v}_k^T \mathbf{M}_\sigma \widehat{\mathbf{e}}^{\text{inc}}. \quad (5.55)$$

Multiplying Eq. (5.55) on the left by \mathbf{M}_σ and substituting $\widehat{\mathbf{j}}^{\text{sca}} = \mathbf{M}_\sigma \widehat{\mathbf{e}}^{\text{sca}}$, gives

$$\widehat{\mathbf{j}}^{\text{sca}} = - \sum_{k=1}^K \frac{j\omega/\lambda_k}{1 + j\omega/\lambda_k} \mathbf{M}_\sigma \mathbf{v}_k \mathbf{v}_k^T \mathbf{M}_\sigma \widehat{\mathbf{e}}^{\text{inc}}, \quad (5.56)$$

where the eigenvalues can be identified as the relaxation frequencies associated with the eddy-current modes. The magnetic polarizability of each of the current density modes can be computed from their magnetic dipole moments,

$$\vec{\mathbf{m}} = \frac{1}{2} \int_V \vec{\mathbf{r}} \times \vec{\mathbf{J}}(\vec{\mathbf{r}}) dV, \quad (5.57)$$

which, in turn, can be evaluated using quadrature. The magnetic dipole moments are computed for eddy currents supported by excitations, $\vec{\mathbf{E}}^{\text{inc}}$, that correspond to $\hat{\mathbf{x}}$ -, $\hat{\mathbf{y}}$ -, and $\hat{\mathbf{z}}$ -

directed uniform magnetic fields². Then, the components of the magnetic polarizabilities are inverted from the magnetic moments using the relation

$$\vec{m} = \mathbf{M} \cdot \vec{\mathbf{H}}^{\text{inc}}. \quad (5.58)$$

The three magnetic excitations provide a full-rank basis, which is sufficient to invert the tensor components.

5.7 Numerical Implementation

The results presented in this chapter are exclusively for a FIT-based electromagnetic model that was decomposed using a Jacobi-Davidson eigenvalue solver that utilizes the SAUG method to avoid the null space [47]. Of all of the methods that were described in this chapter, this was found to be the most reliable method for computing the eigenvalues of the eddy-current problem. Further details on the analysis using standard Jacobi-Davidson with Ritz-value filtering can be found in [49], and analysis using null-space-free Jacobi Davidson can be found in [50].

The numerical code was implemented in Python on a hex-core, 3.40 GHz Intel i7 with 64 GB of memory. It utilized the `PySparse` library in Python for its implementation of the Jacobi-Davidson eigenvalue solver, which supports the SAUG method. Following [47], a projected preconditioner was implemented that required a factorization of the matrix $\mathbf{G}^T \mathbf{M}_\sigma \mathbf{G}$, which was computed using `SUPERLU` [51]. This factorization requires dramatically less storage than a factorization of the curl-curl matrix. Still, the method was memory bound by the size of this factorization. Because of this, the maximum problem size that could be modeled was a cubical grid with 90 cells along each dimension, corresponding to a total of 729,000 cells. A system of this size has 2,235,870 unknowns, and computing 500 of the system's eigenvalues takes approximately 72 h.

²These $\vec{\mathbf{E}}^{\text{inc}}$ are not unique, and many compatible fields could have been chosen. Following McFadden [17], $\vec{\mathbf{E}}^{\text{inc}} = \frac{1}{2}(y\hat{x} - x\hat{y})$ was chosen for the \hat{z} -directed excitation.

The vast majority of the total cells were used to discretize the non-conducting region surrounding the conductor. Although the eddy-currents flow only in the conducting region, the accuracy of the computed current modes and the pole-expansion coefficients is highly dependent on the fidelity of the electric and magnetic fields in the non-conducting region. Truncating these fields too close to the conductor leads to substantial errors. Fewer cells can be used to discretize the non-conducting region if the cells are made to gradually increase in dimension as they become more distant from the conductor. This relative grid coarseness does not significantly impact the accuracy of the coefficients, because in those regions the fields vary more slowly as a function of position.

5.8 Results

5.8.1 Spherical Conductor

The pole-expansion coefficients for a spherical conductor have been computed analytically in the past [6]. Numerical results can, therefore, be compared to their known analytical values. A sphere was placed in the center of a cubical grid with 90 cubical cells in each direction. The sphere had 50 cells across its radius, and the remaining cells were used to model the surrounding air region. The air cells were stretched to be larger as they became more distant from the sphere. This allowed a larger air region to be included, taking advantage of the fact that fields far away from the conductor were found to be less important to the derived coefficients. The normalized numerically-derived coefficients are compared to their analytical values in Fig. 5.4. The two sets of coefficients agree, despite the relative coarseness of the grid. The numerical analysis also provides the current modes that give rise to these coefficients. In Fig. 5.5, plots of the first five current modes that have a non-vanishing dipole moment are shown. These mode graphs are lower resolution than the plots in Fig. 4.2, which is inevitable because the results in this section do not exploit symmetry. The accuracy of the pole-expansion coefficients in Fig. 5.4 is higher than the results in Fig. 3.3, even though the cubical grid does not conform to the shape of the sphere.

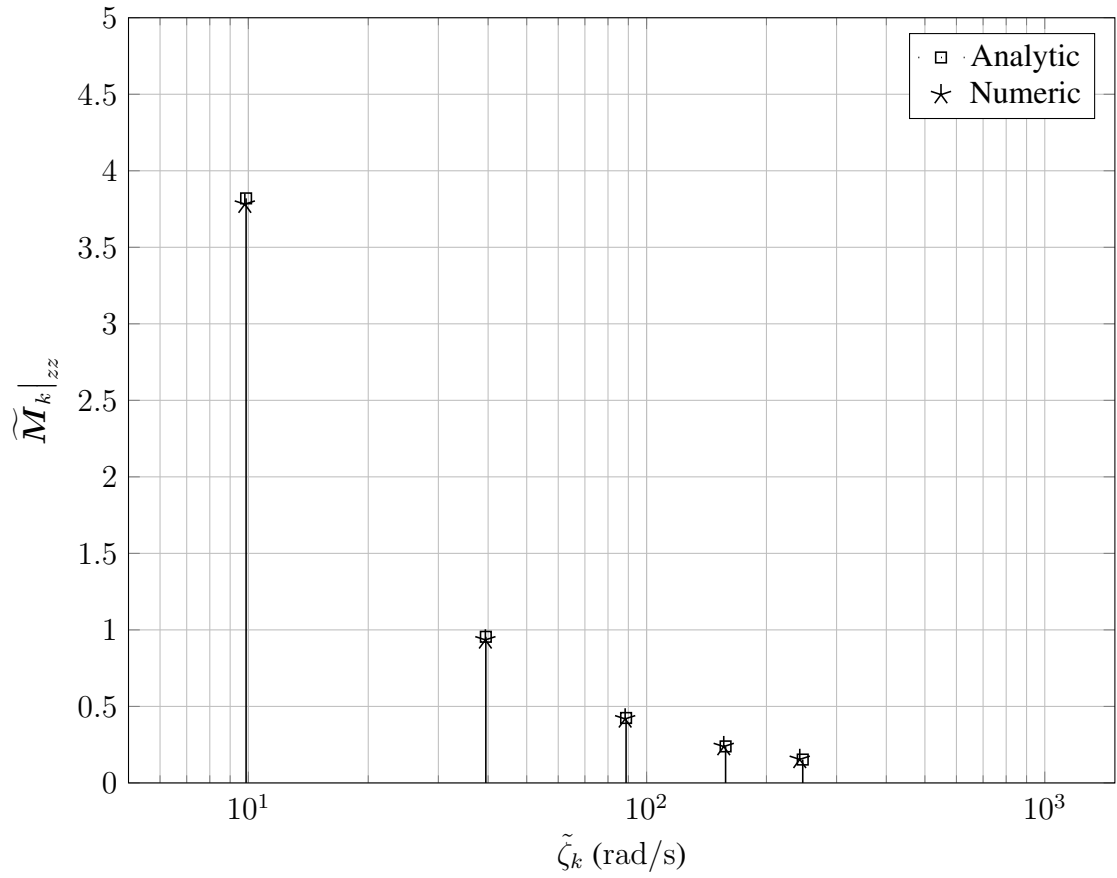


Figure 5.4: Normalized pole-expansion coefficients of a spherical conductor. Since a sphere is an isotropic target, its polarizability tensors are diagonal, with equal entries along the diagonal.

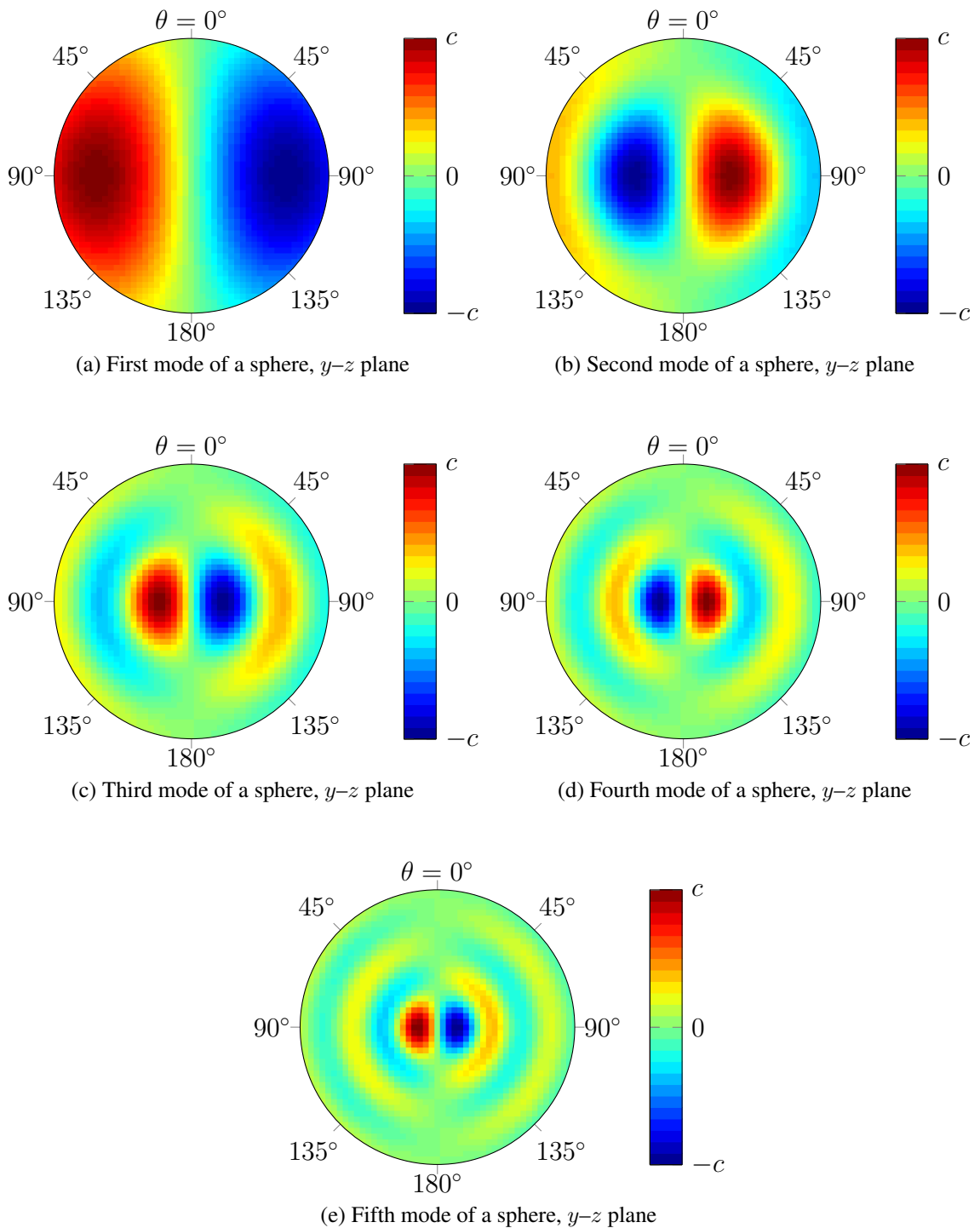


Figure 5.5: Slices of the first five modes of a spherical conductor in the y - z plane, with a dipole moment pointing in the \hat{z} -direction. A color plot of the amplitude of the current density is graphed with blue and red currents flowing in and out of the page respectively.

This is because 3 times as many cells are used to discretize the conducting region. The increased resolution (compared to Chapter 3) greatly improves the accuracy of higher-order coefficients.

5.8.2 Cubical Conductor

The pole-expansion coefficients for a cubical conductor do not have a known analytical expression. Numerical results, therefore, can only be compared to inversions of experimental data. A conducting cube was placed in the center of a grid with 90 cells in each direction. The conducting cube had 50 cells across each of its edges, and the remaining cells were used to model the surrounding air region. Like the grid for the sphere, the air cells were stretched in dimension as they became more distant from the cube. This allowed a larger air region to be included, taking advantage of the fact that fields far away from the conductor were found to be less important to the derived coefficients. A comparison of the normalized numerically-derived and the experimentally-measured coefficients is shown in Fig. 5.6. The two numerical methods agree, with the FIT model most likely achieving better accuracy because of the number of cells as well as the fact that the structured grid matches the shape of the conductor. The numerical analysis also provides the current modes that give rise to these coefficients. In Fig. 5.7, plots of the first five current modes that have a non-vanishing dipole moment are shown. The modes are plotted in the same order that they appear in Fig. 5.6, from left to right. It is important to note, that unlike the sphere, the cross section of the mode does not completely characterize the eddy currents, because the cube is not rotationally symmetric. The increased resolution (compared to Chapter 3) greatly improves the accuracy of the higher-order coefficients as well as the quality of the mode graphs.

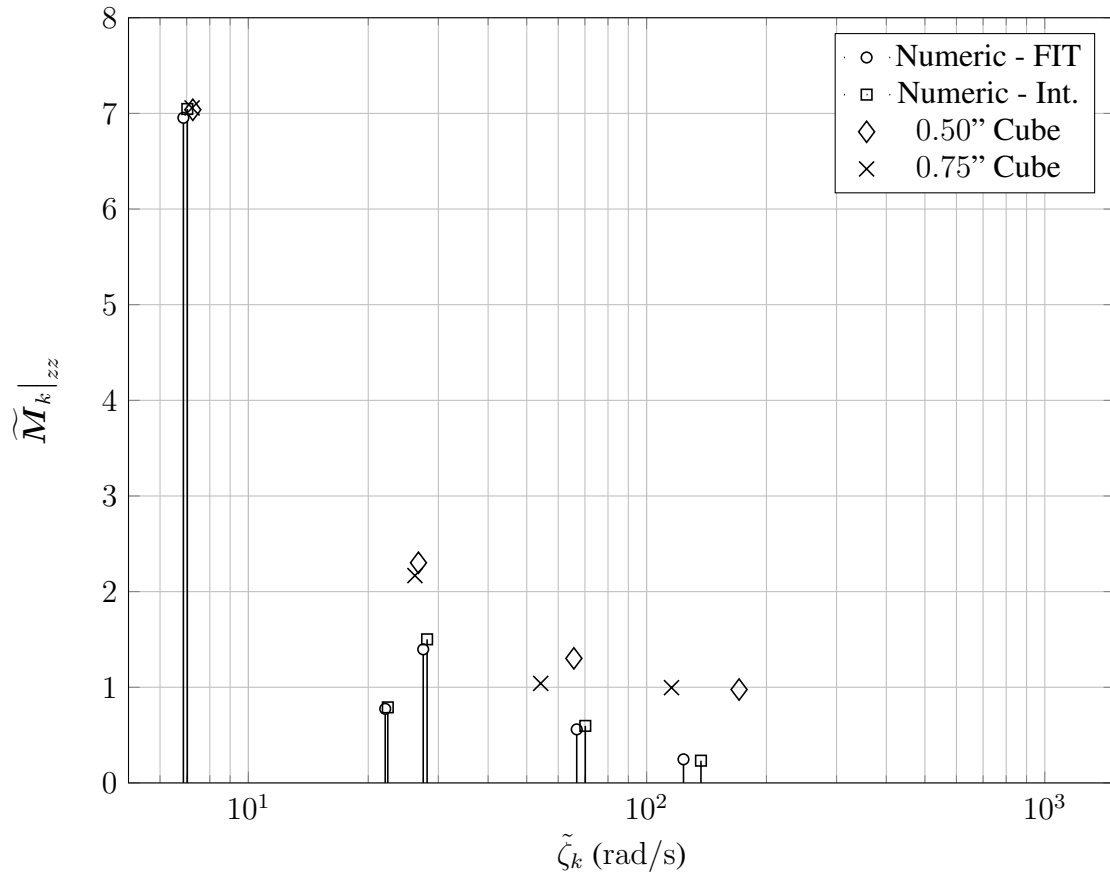


Figure 5.6: Normalized pole-expansion coefficients of a cubical conductor. Since a cube is an isotropic target, its polarizability tensors are diagonal, with equal entries along the diagonal.

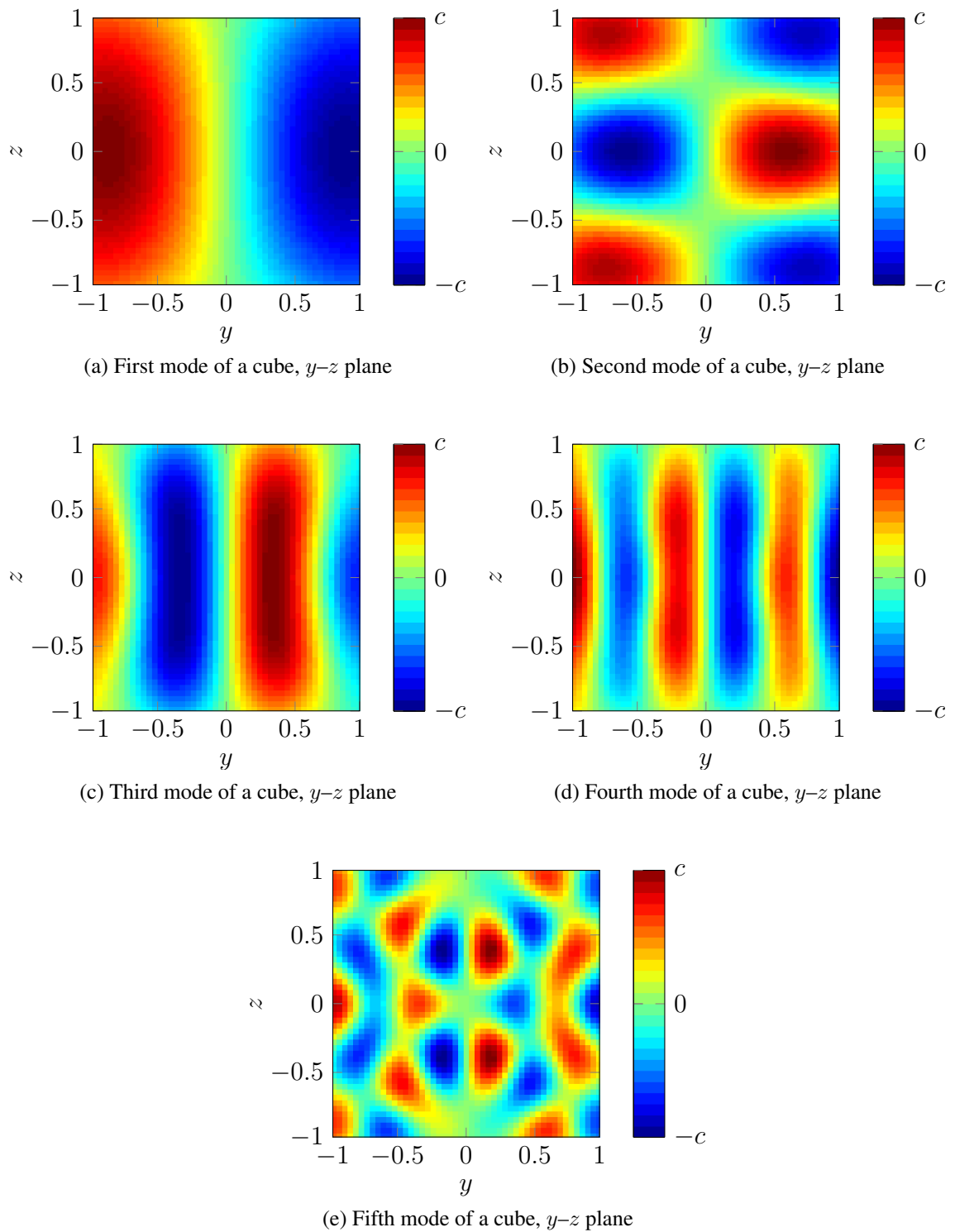


Figure 5.7: Slices of the first five modes of a cubical conductor in the y - z plane, with a dipole moment pointing in the \hat{z} -direction. A color plot of the amplitude of the current density is graphed with blue and red currents flowing in and out of the page respectively.

5.9 Conclusion

A number of approaches were presented for computing the pole-expansion coefficients of the magnetic polarizability of conducting solids. The methods all utilize the finite integration technique, because the regularity of its grids allows for simpler implementation. These methods can be straightforwardly extended for use with the finite element method instead. Numerical results are given for the best-performing of these approaches, which utilizes a Jacobi-Davidson eigenvalue solver that avoids the linear system's null space using a simplified augmented system. To validate the method, the numerically-computed coefficients for a conducting sphere were compared to their analytical values. The numerically-computed coefficients for a conducting cube were compared to inversions of experimental data and to numerically-computed coefficients from the volume integral method. Mode graphs were given for both the sphere and the cube.

CHAPTER 6

CONCLUSIONS AND DISCUSSION

The methods described in this thesis can be used to derive the pole-expansion coefficients of the magnetic polarizability of families of targets, with dedicated methods for targets that are rotationally symmetric or targets that are thin in one dimension. In each of the methods, Maxwell's equations are first represented using a numerical method, either integral or differential, which is then set up as a generalized eigenvalue problem. The eigenvalues of the system correspond to the pole locations of the pole expansion. Because the eigenvectors of the system are the simply the associated mode patterns, deriving the remaining coefficients in the pole expansion involves very straightforward post-processing.

Depending on the method, the task of finding the smallest eigenvalues of the linear systems ranges from being trivial to extremely difficult. In the case of two of the integral methods, for rotationally symmetric targets and for thin targets, it is sufficient to apply a standard eigenvalue solver for dense symmetric matrices. In the case of the volume integral method, both system matrices must be projected away from their null space before applying a standard eigenvalue solver. For differential methods, the matrices are large, sparse, and have a large null space, which cannot be removed without destroying the sparsity. For these methods, two alternative approaches were explored for finding the eigenvalues, both utilizing the Jacobi-Davidson iteration.

Of the integral and differential methods that were presented for deriving the pole-expansion coefficients of arbitrary volumes, each has advantages and disadvantages. The volume integral method scales poorly, because the volume of the conductor is discretized and the system matrices are dense. Utilizing a standard eigenvalue solver guarantees stability. Differential methods scale much better since the system matrices are sparse. Unfortunately, a large volume around the conductor must also be discretized. Additionally,

neither versions of the Jacobi-Davidson iteration have guaranteed stability. In either case, any method for volumes that does not exploit symmetry requires large amounts of storage and computation time.

Permeable materials, which appear quite frequently in targets of interest, were not considered in this thesis. It is not apparent that any of the integral methods that were presented could be extended to model permeable targets. The differential methods should correctly predict the relaxation frequencies associated with permeable targets without requiring any changes, provided that the correct cell permeabilities are assigned. We hypothesize that it would be possible to derive the tensor coefficients as well, if the correct magnetic excitation was applied, however, this was not explored due to time constraints.

All the methods exhibited high accuracy when comparing the numerically-derived coefficients to their analytical values. When results were compared to inversions of experimental data, the two sets of coefficients were often in good agreement, except for situations where the inversions are known to be inaccurate. This includes situations where poles in the expansion are not sufficiently separated in frequency and situations where the tensor coefficients are very weak relative to the primary tensor amplitude. These situations, however, are known to be problematic, and highlight the importance of numerical modeling, which does not suffer from the same limitations.

There are several areas that could be productive areas for future research. Locally optimal block preconditioned conjugate gradients (LOBPCG) has recently been proposed as an alternative to Jacobi-Davidson, for computing the eigenvalues of linear systems associated with differential formulations of Maxwell's equations [52]. It would be interesting to see if an improved implementation of NFJD and LOBPCG could be competitive at finding the smallest eigenvalues of the eddy-current problem. It would also be straightforward to try to extend the work in Chapter 5 to model permeable targets. Finally, the differential formulation can be implemented using the finite element method instead of FIT. A tetrahedral mesh would conform better to most targets, and would allow for smoother cell scaling in the non-

conducting region. Another interesting approach would be to combine a boundary element method for the non-conducting region with a differential method for the conducting region.

Appendices

APPENDIX A
DERIVATION OF THE RECIPROCITY RELATION

The reciprocity relation for EMI sensors states that the electromotive force induced on a receive coil is approximately proportional to a tensor product of the magnetic polarizability tensor, the magnetic excitation due to the transmit coil, and the magnetic excitation due to the receive coil had it been driven by a unit-magnitude steady current. The magnetic excitations are the only terms in the relation that depend on position. Different justifications can give rise to this reciprocity relation, giving different views on its error bounds and physical meaning [13]. In the following derivation, the common engineering viewpoint will be adopted.

Under magnetostatic assumptions, the magnetic field, $\vec{B}(\vec{r})$, due to a steady current, I , flowing in a coil can be expressed using the Biot-Savart law,

$$\vec{B}(\vec{r}) = \frac{\mu_0}{4\pi} \oint_C \frac{I d\vec{\ell} \times \vec{r}'}{\|\vec{r}'\|^3}, \quad (\text{A.1})$$

where \vec{r} is the position in space, C is the closed current path of the coil, comprised of infinitesimal wire segments, $d\vec{\ell}$, that point in the local direction of current flow, and $\vec{r}' = \vec{r} - \vec{\ell}$, which represents the full displacement vector to the wire segments, $d\vec{\ell}$.

Now, assume that the scattering from a buried target can be accurately approximated using a magnetic dipole moment, \vec{m} . The vector potential due to a magnetic dipole moment is then approximately

$$\vec{A}(\vec{r}) \approx \frac{\mu_0}{4\pi} \frac{\vec{m} \times \vec{r}}{\|\vec{r}\|^3}, \quad (\text{A.2})$$

which corresponds to the first non-zero term in the multipole expansion. This assumption becomes more valid as the distance away from the dipole increases. The electromotive

force induced on the circuit, V_{ind} , by Faraday's law, can be written as

$$V_{\text{ind}} = \oint_C \vec{E}(\vec{r}) \cdot d\vec{\ell} = -j\omega \oint_C \vec{A}(\vec{r}) \cdot d\vec{\ell}. \quad (\text{A.3})$$

Substituting Eq. (A.2) into Eq. (A.3), the EMF induced in the receive coil due to a magnetic dipole, can be expressed as

$$V_{\text{ind}} \approx -j\omega \oint_C \frac{\mu_0}{4\pi} \frac{\vec{m} \times \vec{r} \cdot d\vec{\ell}}{\|\vec{r}\|^3}. \quad (\text{A.4})$$

Rearranging the triple product, $\vec{m} \times \vec{r} \cdot d\vec{\ell} = -\vec{m} \cdot d\vec{\ell} \times \vec{r}$, Eq. (A.4) may be written as

$$V_{\text{ind}} \approx j\omega \vec{m} \cdot \left(\frac{\mu_0}{4\pi} \oint_C \frac{d\vec{\ell} \times \vec{r}}{\|\vec{r}\|^3} \right), \quad (\text{A.5})$$

where we recognize that the right term in the dot product is, by the Biot-Savart law, simply the magnetic field due to the receive coil, had it been driven by a unit-magnitude steady current. This means that Eq. (A.5) may also be written as

$$V_{\text{ind}} \approx j\omega \mu_0 \vec{m} \cdot \vec{H}_{\text{RX}}(\vec{r}). \quad (\text{A.6})$$

Next, we introduce the magnetic polarizability tensor, \mathbf{M} , which relates the magnetic dipole moment to the magnetic excitation from the transmitter, $\vec{H}_{\text{TX}}(\vec{r})$, by the relation

$$\vec{m} = \mathbf{M} \cdot \vec{H}_{\text{TX}}(\vec{r}). \quad (\text{A.7})$$

Substituting Eq. (A.7) into Eq. (A.6) we arrive at the final form of the reciprocity relation,

$$V_{\text{ind}} \approx j\omega \mu_0 \vec{H}_{\text{RX}}(\vec{r}) \cdot \left(\mathbf{M} \cdot \vec{H}_{\text{TX}}(\vec{r}) \right). \quad (\text{A.8})$$

APPENDIX B

POLE EXPANSION OF A SPHERICAL SHELL

Let Ω_c be a thin conducting spherical shell centered about the origin. Assume that the spherical shell has a radius of a , and a surface conductivity σ_s . Because of the axial symmetry, the eddy currents must flow entirely in the azimuthal direction. Following the procedure in §7.12 [53], the stream function of the current density can be written as

$$\psi = \sum_{n=1}^{\infty} C_n P_n(\cos \theta), \quad (\text{B.1})$$

where the C_n are scalar functions that are frequency dependent, P_n are Legendre polynomials, and θ is the polar angle. Given that the gradient operator in spherical coordinates is

$$\nabla f = \frac{\partial f}{\partial r} \hat{\mathbf{r}} + \frac{1}{r} \frac{\partial f}{\partial \theta} \hat{\boldsymbol{\theta}} + \frac{1}{r \sin \theta} \frac{\partial f}{\partial \phi} \hat{\boldsymbol{\phi}}, \quad (\text{B.2})$$

the current density associated with this stream function is

$$\mathbf{J}_\phi = \frac{1}{a} \frac{\partial \psi}{\partial \theta} = \sum_{n=1}^{\infty} \frac{C_n}{a} \frac{\partial}{\partial \theta} (P_n(\cos \theta)) = - \sum_{n=1}^{\infty} \frac{C_n \sin \theta}{a} \frac{\partial}{\partial u} (P_n(u)) = - \sum_{n=1}^{\infty} \frac{C_n}{a} P_n^1(\cos \theta), \quad (\text{B.3})$$

where the substitution $u = \cos \theta$ was made, and P_n are the associated Legendre polynomials of the first order. The magnetic vector potential associated with this current, which, in this case, is the field scattered by the spherical shell, is

$$\vec{\mathbf{A}}^{\text{sca}} = \begin{cases} \mu_0 \hat{\boldsymbol{\phi}} \sum_{n=1}^{\infty} \frac{-C_n}{2n+1} \left(\frac{r}{a}\right)^n P_n^1(\cos \theta), & \text{when } r \leq a, \\ \mu_0 \hat{\boldsymbol{\phi}} \sum_{n=1}^{\infty} \frac{-C_n}{2n+1} \left(\frac{a}{r}\right)^{n+1} P_n^1(\cos \theta), & \text{when } r > a. \end{cases} \quad (\text{B.4})$$

For this potential, the radial component of the magnetic field is

$$\mathbf{B}_r^{\text{sca}} = \begin{cases} -\frac{\mu}{a} \sum_{n=1}^{\infty} \frac{n(n+1)C_n}{2n+1} \left(\frac{r}{a}\right)^{n-1} P_n(\cos \theta), & \text{when } r \leq a, \\ -\frac{\mu}{a} \sum_{n=1}^{\infty} \frac{n(n+1)C_n}{2n+1} \left(\frac{a}{r}\right)^{n+2} P_n(\cos \theta), & \text{when } r > a, \end{cases} \quad (\text{B.5})$$

and the polar component of the scattered magnetic field is

$$\mathbf{B}_\theta^{\text{sca}} = \begin{cases} +\frac{\mu}{a} \sum_{n=1}^{\infty} \frac{(n+1)C_n}{2n+1} \left(\frac{r}{a}\right)^{n-1} P_n^1(\cos \theta), & \text{when } r \leq a, \\ +\frac{\mu}{a} \sum_{n=1}^{\infty} \frac{(n+1)C_n}{2n+1} \left(\frac{a}{r}\right)^{n+2} P_n^1(\cos \theta), & \text{when } r > a. \end{cases} \quad (\text{B.6})$$

The incident excitation corresponding to a \hat{z} -directed uniform time-varying magnetic field with magnitude $\|\mathbf{H}_0\|$ is

$$\vec{\mathbf{A}}^{\text{inc}} = \frac{1}{2}\mu_0 \|\vec{\mathbf{H}}_0\| r P_n^1(\cos \theta). \quad (\text{B.7})$$

Eddy currents are excited by the total magnetic vector potential, which can be decomposed into scattered and incident components,

$$-\frac{1}{\sigma} \vec{\mathbf{J}} = j\omega \vec{\mathbf{A}}^{\text{sca}} + j\omega \vec{\mathbf{A}}^{\text{inc}}. \quad (\text{B.8})$$

Evaluating Eq. (B.8) using the expansions in Eq. (B.3, B.4, B.7), with $r = a$, gives

$$\sigma_s^{-1} \sum_{n=1}^{\infty} \frac{C_n}{a} P_n^1(\cos \theta) + j\omega\mu_0 \sum_{n=1}^{\infty} \frac{C_n}{2n+1} P_n^1(\cos \theta) = \frac{1}{2}j\omega\mu_0 \|\vec{\mathbf{H}}_0\| r P_n^1(\cos \theta). \quad (\text{B.9})$$

Because of the orthogonality of the associated Legendre polynomials, only the $n = 1$ terms of the summations can have non-zero coefficients. It is sufficient to solve for C_1 ,

$$\begin{aligned}
\frac{1}{\sigma_s} \frac{C_1}{a} P_1^1(\cos \theta) &= -j\omega\mu_0 \frac{C_1}{3} P_1^1(\cos \theta) + \frac{1}{2} j\omega\mu_0 \left\| \vec{\mathbf{H}}_0 \right\| a P_1^1(\cos \theta) \\
\frac{1}{\sigma_s} \frac{C_1}{a} &= -j\omega\mu_0 \frac{C_1}{3} + \frac{1}{2} j\omega\mu_0 \left\| \vec{\mathbf{H}}_0 \right\| a \\
\frac{1}{\sigma_s} \frac{C_1}{a} + j\omega\mu_0 \frac{C_1}{3} &= \frac{1}{2} j\omega\mu_0 \left\| \vec{\mathbf{H}}_0 \right\| a \\
C_1 + j\omega \frac{\mu_0 \sigma_s a}{3} C_1 &= \frac{1}{2} j\omega\mu_0 \sigma_s \left\| \vec{\mathbf{H}}_0 \right\| a^2 \\
C_1 \left(1 + j\omega \frac{\mu_0 \sigma_s a}{3} \right) &= \frac{1}{2} j\omega\mu_0 \sigma_s \left\| \vec{\mathbf{H}}_0 \right\| a^2 \\
C_1 &= \frac{j\omega / \left(\frac{3}{\mu_0 \sigma_s a} \right)}{1 + j\omega / \left(\frac{3}{\mu_0 \sigma_s a} \right)} \frac{3}{2} a \left\| \vec{\mathbf{H}}_0 \right\|.
\end{aligned}$$

Substituting C_1 into Eq. (B.3) gives an expression for the current density,

$$\mathbf{J}_\phi = - \frac{3 \left\| \vec{\mathbf{H}}_0 \right\| P_n^1(\cos \theta)}{2} \left(\frac{j\omega / \left(\frac{3}{\mu_0 \sigma_s a} \right)}{1 + j\omega / \left(\frac{3}{\mu_0 \sigma_s a} \right)} \right), \quad (\text{B.10})$$

where by examination it is apparent that $\zeta_1 = \frac{3}{\mu_0\sigma_s a}$. In order to compute M_1 it is first necessary to find the dipole moment of the current density

$$\begin{aligned}
\vec{m} &= \frac{1}{2} \int_S a \hat{r} \times \mathbf{J}_\phi dS = -\frac{3}{4} \int_S a \|\vec{H}_0\| P_1^1(\cos\theta) \hat{\theta} dS \\
&= -\frac{3}{4} a \|\vec{H}_0\| \int_S \hat{\theta} \sin\theta dS \\
&= -\frac{3}{4} a \|\vec{H}_0\| \int_0^{2\pi} \int_0^\pi \hat{\theta} a^2 \sin^2(\theta) d\theta d\phi \\
&= -\frac{3}{4} a^3 \|\vec{H}_0\| \int_0^{2\pi} \int_0^\pi \hat{\theta} \sin^2(\theta) d\theta d\phi \\
&= -\frac{3}{4} a^3 \|\vec{H}_0\| \int_0^{2\pi} \int_0^\pi [\cos\theta \cos\phi \hat{x} + \cos\theta \sin\phi \hat{y} - \sin\theta \hat{z}] \sin^2(\theta) d\theta d\phi \\
&= -\frac{3}{4} a^3 \|\vec{H}_0\| \left[0\hat{x} + 0\hat{y} - \frac{4}{3} 2\pi \hat{z} \right] = 2\pi a^3 \|\vec{H}_0\| \hat{z}.
\end{aligned}$$

Since the incident magnetic field, in this derivation, is defined as $\vec{H}^{\text{inc}} = -\|\vec{H}_0\| \hat{z}$, the zz -component of the magnetic polarizability is

$$\mathbf{M}_{zz} = -\left(\frac{j\omega / (\frac{3}{\mu_0\sigma_s a})}{1 + j\omega / (\frac{3}{\mu_0\sigma_s a})} \right) 2\pi a^3, \quad (\text{B.11})$$

with $M_{zx} = M_{zy} = 0$. By symmetry, this can be repeated with \hat{x} - and \hat{y} -directed excitations, resulting in

$$\mathbf{M}(\omega) = -\left(\frac{j\omega / (\frac{3}{\mu_0\sigma_s a})}{1 + j\omega / (\frac{3}{\mu_0\sigma_s a})} \right) 2\pi a^3 \mathbf{I}_3, \quad (\text{B.12})$$

where we can identify that $M_1 = 2\pi a^3 \mathbf{I}_3$.

REFERENCES

- [1] *Why landmines are still a problem*, <http://http://www.icbl.org/en-gb/problem/why-landmines-are-still-a-problem.aspx>, Accessed: 2018-12-17.
- [2] E. Lenz, “Ueber die bestimmung der richtung der durch elektrodynamische vertheilung erregten galvanischen ströme,” *Annalen der Physik*, vol. 107, no. 31, pp. 483–494, 1834.
- [3] W. R. Scott, “Broadband array of electromagnetic induction sensors for detecting buried landmines,” in *IGARSS 2008-2008 IEEE International Geoscience and Remote Sensing Symposium*, IEEE, vol. 2, 2008, pp. II–375.
- [4] L. Carin, H. Yu, Y. Dalichaouch, A. R. Perry, P. V. Czipott, and C. E. Baum, “On the wideband emi response of a rotationally symmetric permeable and conducting target,” *IEEE Trans. Geosci. Remote Sens.*, vol. 39, no. 6, pp. 1206–1213, 2001.
- [5] W. R. Scott and M. McFadden, “Simple wideband models for disks and wires in the eddy current approximation,” *Journal of Applied Geophysics*, vol. 92, pp. 137–143, 2013.
- [6] C. E. Baum, *Detection and identification of visually obscured targets*. CRC Press, 1998.
- [7] B. E. Barrowes, K. O’Neill, T. M. Grzegorzczuk, X. Chen, and J. A. Kong, “Broadband analytical magnetoquasistatic electromagnetic induction solution for a conducting and permeable spheroid,” *IEEE Trans. Geosci. Remote Sens.*, vol. 42, no. 11, pp. 2479–2489, 2004.
- [8] J. E. Gabbay and W. R. Scott, “The eigendecomposition of the eddy current problem in thin conducting shells,” in *Geoscience and Remote Sensing Symposium (IGARSS), 2017 IEEE International*, IEEE, 2017, pp. 4829–4832.
- [9] A. Bossavit, *Computational electromagnetism: variational formulations, complementarity, edge elements*. Academic Press, 1998.
- [10] O. Bíró, “Edge element formulations of eddy current problems,” *Computer Methods in Applied Mechanics and Engineering*, vol. 169, no. 3-4, pp. 391–405, 1999.
- [11] S. Engleder, “Boundary element methods for eddy current transmission problems,” PhD thesis, Graz University of Technology, 2011.

- [12] R. Hiptmair, “Symmetric coupling for eddy current problems,” *SIAM Journal on Numerical Analysis*, vol. 40, no. 1, pp. 41–65, 2002.
- [13] P. D. Ledger and W. B. Lionheart, “Understanding the magnetic polarizability tensor,” *IEEE Trans. Magn.*, vol. 52, no. 5, pp. 1–16, 2016.
- [14] F. Shubitidze, K. O’Neill, S. A. Haider, K. Sun, and K. D. Paulsen, “Application of the method of auxiliary sources to the wide-band electromagnetic induction problem,” *IEEE Trans. Geosci. Remote Sens.*, vol. 40, no. 4, pp. 928–942, 2002.
- [15] P. D. Ledger and W. R. Lionheart, “An explicit formula for the magnetic polarizability tensor for object characterization,” *IEEE Trans. Geosci. Remote Sens.*, vol. 56, no. 6, pp. 3520–3533, 2018.
- [16] C. E. Baum, E. J. Rothwell, K. M. Chen, and D. P. Nyquist, “The singularity expansion method and its application to target identification,” *Proc. IEEE*, vol. 79, no. 10, pp. 1481–1492, 1991.
- [17] M. McFadden and W. R. Scott, “Computing simple models for scatterers in eddy current problems using a modal decomposition,” *Journal of Applied Geophysics*, vol. 95, pp. 104–114, 2013.
- [18] M.-H. Wei, “Electromagnetic induction spectroscopy for the detection of subsurface targets,” PhD thesis, Georgia Institute of Technology, 2012.
- [19] K. R. Krueger, “Model design for algorithmic efficiency in electromagnetic sensing,” PhD thesis, Georgia Institute of Technology, 2013.
- [20] C. E. Hayes, J. H. McClellan, and W. R. Scott, “Low-rank physical model recovery from low-rank signal approximation,” in *2017 IEEE International Conference on Acoustics, Speech and Signal Processing (ICASSP)*, IEEE, 2017, pp. 3131–3135.
- [21] K. Sun, K. O’Neill, F. Shubitidze, I. Shamatava, and K. D. Paulsen, “Fast data-derived fundamental spheroidal excitation models with application to UXO discrimination,” *IEEE Trans. Geosci. Remote Sens.*, vol. 43, no. 11, pp. 2573–2583, 2005.
- [22] M.-H. Wei, W. R. Scott, and J. H. McClellan, “Robust estimation of the discrete spectrum of relaxations for electromagnetic induction responses,” *IEEE Trans. Geosci. Remote Sens.*, vol. 48, no. 3, pp. 1169–1179, 2010.
- [23] J. E. Gabbay and W. R. Scott, “Wideband models for the electromagnetic induction signatures of thin conducting shells,” *IEEE Trans. Geosci. Remote Sens.*, pp. 1–9, 2019.

- [24] J. E. Gabbay and W. R. Scott, “Improved surface method for computing eddy-current modes,” in *Proc. SPIE 10182, Detection and Sensing of Mines, Explosive Objects, and Obscured Targets XXII*, vol. 10182, 2017.
- [25] J.-C. Nédélec, “Mixed finite elements in R^3 ,” *Numerische Mathematik*, vol. 35, no. 3, pp. 315–341, 1980.
- [26] J.-C. Nédélec, “A new family of mixed finite elements in R^3 ,” *Numerische Mathematik*, vol. 50, no. 1, pp. 57–81, 1986.
- [27] G. Xiao, “Applying loop-flower basis functions to analyze electromagnetic scattering problems of PEC scatterers,” *IEEE Trans. Antennas Propag.*, vol. 2014, 2014.
- [28] P.-O. Persson and G. Strang, “A simple mesh generator in MATLAB,” *SIAM review*, vol. 46, no. 2, pp. 329–345, 2004.
- [29] C. Geuzaine and J.-F. Remacle, “Gmsh: A 3-D finite element mesh generator with built-in pre- and post-processing facilities,” *International Journal for Numerical Methods in Engineering*, vol. 79, no. 11, pp. 1309–1331, 2009.
- [30] A. F. Peterson, S. L. Ray, and R. Mittra, *Computational methods for electromagnetics*. IEEE press New York, 1998, vol. 2.
- [31] F. Moro, P. Alotto, A. Stella, and M. Guarnieri, “Solving 3-d eddy currents in thin shells of any shape and topology,” *IEEE Trans. Magn.*, vol. 51, no. 3, pp. 1–4, 2015.
- [32] R. D. Graglia, “On the numerical integration of the linear shape functions times the 3-D green’s function or its gradient on a plane triangle,” *IEEE Trans. Antennas Propag.*, vol. 41, no. 10, pp. 1448–1455, 1993.
- [33] H. Braunsch, C. O. Ao, K. O’Neill, and J. A. Kong, “Magnetoquasistatic response of conducting and permeable prolate spheroid under axial excitation,” *IEEE Trans. Geosci. Remote Sens.*, vol. 39, no. 12, pp. 2689–2701, 2001.
- [34] P. W. Gross, P. W. Gross, P. R. Kotiuga, and R. P. Kotiuga, *Electromagnetic theory and computation: a topological approach*. Cambridge University Press, 2004, vol. 48.
- [35] R. C. Prim, “Shortest connection networks and some generalizations,” *Bell System Technical Journal*, vol. 36, no. 6, pp. 1389–1401, 1957.
- [36] R. B. Lehoucq, D. C. Sorensen, and C. Yang, *ARPACK users’ guide: solution of large-scale eigenvalue problems with implicitly restarted Arnoldi methods*. Siam, 1998, vol. 6.

- [37] R. D. Graglia and G. Lombardi, "Machine precision evaluation of singular and nearly singular potential integrals by use of Gauss quadrature formulas for rational functions," *IEEE Trans. Antennas Propag.*, vol. 56, no. 4, pp. 981–998, 2008.
- [38] R. Cools, "An encyclopaedia of cubature formulas," *Journal of complexity*, vol. 19, no. 3, pp. 445–453, 2003.
- [39] A. Kaufman, "Frequency and transient responses of electromagnetic fields created by currents in confined conductors," *Geophysics*, vol. 43, no. 5, pp. 1002–1010, 1978.
- [40] M. C. T. Weiland, "Discrete electromagnetism with the finite integration technique," *Progress In Electromagnetics Research*, vol. 32, pp. 65–87, 2001.
- [41] K. Yee, "Numerical solution of initial boundary value problems involving maxwell's equations in isotropic media," *IEEE Trans. Antennas Propag.*, vol. 14, no. 3, pp. 302–307, 1966.
- [42] R. Russenschuck, "Electromagnetic design of accelerator magnets," Cern, Tech. Rep., 2006.
- [43] J. Kestyn, E. Polizzi, and P. T. Peter Tang, "FEAST eigensolver for non-hermitian problems," *SIAM Journal on Scientific Computing*, vol. 38, no. 5, S772–S799, 2016.
- [44] G. L. Sleijpen and H. A. Van der Vorst, "A Jacobi–Davidson iteration method for linear eigenvalue problems," *SIAM review*, vol. 42, no. 2, pp. 267–293, 2000.
- [45] W. Rodrigues, A. Pecchia, M. A. der Maur, and A. Di Carlo, "A comprehensive study of popular eigenvalue methods employed for quantum calculation of energy eigenstates in nanostructures using gpus," *Journal of Computational Electronics*, vol. 14, no. 2, pp. 593–603, 2015.
- [46] V. Hernandez, J. E. Roman, and V. Vidal, "SLEPc: A scalable and flexible toolkit for the solution of eigenvalue problems," *ACM Trans. Mathematical Software (TOMS)*, vol. 31, no. 3, pp. 351–362, 2005.
- [47] R. Geus, "The Jacobi-Davidson algorithm for solving large sparse symmetric eigenvalue problems with application to the design of accelerator cavities," PhD thesis, ETH Zurich, 2002.
- [48] Y.-L. Huang, T.-M. Huang, W.-W. Lin, and W.-C. Wang, "A null space free jacobi–davidson iteration for maxwell's operator," *SIAM Journal on Scientific Computing*, vol. 37, no. 1, A1–A29, 2015.

- [49] J. E. Gabbay and W. R. Scott, “Analysis of the natural modes of the 3-d eddy current problem based on the finite integration technique,” in *2015 IEEE International Geoscience and Remote Sensing Symposium (IGARSS)*, IEEE, 2015, pp. 1646–1649.
- [50] J. E. Gabbay and W. R. Scott, “Modal analysis of the eddy current problem using null-space-free jacobi-davidson,” in *2016 IEEE International Geoscience and Remote Sensing Symposium (IGARSS)*, IEEE, 2016, pp. 7493–7496.
- [51] X. S. Li, “An overview of superlu: Algorithms, implementation, and user interface,” *ACM Transactions on Mathematical Software (TOMS)*, vol. 31, no. 3, pp. 302–325, 2005.
- [52] T.-M. Huang, W.-Q. Huang, and W.-W. Lin, “A robust numerical algorithm for computing maxwell’s transmission eigenvalue problems,” *SIAM Journal on Scientific Computing*, vol. 37, no. 5, A2403–A2423, 2015.
- [53] W. R. Smythe, “Static and dynamic electricity,” in, 2nd ed. McGraw-Hill Book Company Inc., 1950, ch. 7.12, pp. 273–274.

VITA



Jonathan Eliezer Gabbay was born in Westwood, New Jersey in 1987. He received his BS from Rutgers University in New Brunswick, NJ, in 2009, and he received his MS from the Georgia Institute of Technology in Atlanta, GA, in 2012. He received his PhD degree in Electrical and Computer Engineering at the Georgia Institute of Technology in 2019. His research interests include computational electromagnetics, iterative methods, as well as subsurface detection and imaging. He was the recipient of the President's fellowship at the Georgia Institute of Technology.